



**INSTITUTO DE PESQUISAS ENERGÉTICAS E NUCLEARES**  
**Autarquia Associada à Universidade de São Paulo**

**The effect of hot-stamping process on the local electrochemical behaviour  
of the 22MnB5 steel coated with hot-dip aluminium-silicon**

**CAMILA PUCCI COUTO**

**Tese apresentada como parte dos  
requisitos para obtenção do Grau de  
Doutor em Ciências na Área  
de Tecnologia Nuclear - Materiais**

**Orientadores:**

**Prof. Dr. Jesualdo Luiz Rossi**

**Prof. Dr. Ir. Herman Terry**

**São Paulo**

**2021**

**INSTITUTO DE PESQUISAS ENERGÉTICAS E NUCLEARES**  
**Autarquia Associada à Universidade de São Paulo**

**The effect of hot-stamping process on the local electrochemical behaviour  
of the 22MnB5 steel coated with hot-dip aluminium-silicon**

**Versão Corrigida**

**Versão Original disponível no IPEN**

**CAMILA PUCCI COUTO**

**Tese apresentada como parte dos  
requisitos para obtenção do Grau de  
Doutor em Ciências na Área  
de Tecnologia Nuclear - Materiais**

**Orientadores:**

**Prof. Dr. Jesualdo Luiz Rossi**

**Prof. Dr. Ir. Herman Terryn**

**São Paulo**

**2021**

**The effect of hot-stamping process on the local  
electrochemical behaviour of the 22MnB5 steel  
coated with hot-dip aluminium-silicon**



**Camila Pucci Couto**

**Promotors: Prof. Dr. Jesualdo Luiz Rossi**

**Prof. Dr. Ir. Herman Terry**

**Dr. Reynier Inocente Revilla Castillo**

Faculty of Engineering  
Vrije Universiteit Brussel

Thesis in a Joint PhD submitted in fulfilment of the requirements for the award of the  
degree of Doctor of Engineering Sciences

July 2021

Fonte de Financiamento: CAPES-PROEX; CAPES-PDSE (88881.189691/2018-01); CNPq-SWE (205368/2018-2)

Autorizo a reprodução e divulgação total ou parcial deste trabalho,  
para fins de estudo e pesquisa, desde que citada a fonte

Como citar:

COUTO, C. P. *The effect of hot-stamping process on the local electrochemical behaviour of the 22MnB5 steel coated with hot-dip aluminium-silicon*. 2021. 170 p. Tese (Doutorado em Tecnologia Nuclear), Instituto de Pesquisas Energéticas e Nucleares, IPEN-CNEN/SP, São Paulo. Disponível em: (data de consulta no formato: dd/mm/aaaa)

Ficha catalográfica elaborada pelo Sistema de geração automática da Biblioteca IPEN/USP, com os dados fornecidos pelo(a) autor(a)

Couto, Camila Pucci The effect of hot-stamping process on the local electrochemical behaviour of the 22MnB5 steel coated with hot-dip aluminium-silicon / Camila Pucci Couto; orientador Jesualdo Luiz Rossi. -- São Paulo, 2021. 170 p.

Tese (Doutorado) - Programa de Pós-Graduação em Tecnologia Nuclear (Materiais) -- Instituto de Pesquisas Energéticas e Nucleares, São Paulo, 2021.

1. Press-hardened steel. 2. Hot stamping. 3. Hot-dip aluminium-silicon. 4. Electrochemical behaviour. 5. Corrosion. I. Rossi, Jesualdo Luiz, orient. II. Título.



Faculty of Engineering - Department of Materials and Chemistry,  
Research Group Electrochemical and Surface Engineering

---

**The effect of hot-stamping process on the local electrochemical behaviour of the  
22MnB5 steel coated with hot-dip aluminium-silicon**

Camila Pucci Couto

**Members of the jury**

Prof. Dr. Ir. Lincy Pyl	<i>President of the jury</i> Vrije Universiteit Brussel Department Mechanics of Materials and Constructions
Prof. Dr. Ir. Rik Pintelon	<i>Vice-president of the jury</i> Vrije Universiteit Brussel Department of Electricity
Prof. Dr. Ir. Iris De Graeve	<i>Secretary of the jury</i> Vrije Universiteit Brussel Department of Materials and Chemistry
Dr. Krista Van den Bergh	<i>External member of the jury</i> OCAS n.v. - Arcelor Mittal
Prof. Dr. Oscar Rosa Mattos	<i>External member of the jury</i> Universidade Federal do Rio de Janeiro (UFRJ - Brazil) Department of Metallurgical and Materials Engineering
Prof. Dr. Hercílio Gomes de Melo	<i>External member of the jury</i> Universidade de São Paulo (USP - Brazil) Department of Metallurgical and Materials Engineering
Prof. Dr. Jesualdo Luiz Rossi	<i>Supervisor</i> Instituto de Pesquisas Energéticas e Nucleares (IPEN - Brazil) Materials Science and Technology Centre
Prof. Dr. Ir. Herman Terryn	<i>Supervisor</i> Vrije Universiteit Brussel Department of Materials and Chemistry
Dr. Reynier Inocente Revilla Castillo	<i>Supervisor</i> Vrije Universiteit Brussel Department of Materials and Chemistry

## **Board of examiners**

### **Instituto de Pesquisas Energéticas e Nucleares - Universidade de São Paulo**

Author: Camila Pucci Couto

Title: The effect of hot-stamping process on the local electrochemical behaviour of the 22MnB5 steel coated with hot-dip aluminium-silicon

This thesis is a Joint PhD presented to the Post-Graduate Programme in Nuclear Technology at University of São Paulo for the award of the degree of Doctor in Science.

5 July 2021

## **Board of examiners**

### **Full members**

Prof. Dr. Jesualdo Luiz Rossi	Instituto de Pesquisas Energéticas e Nucleares (IPEN - Brazil)
Prof. Dr. Ir. Herman Terryn	Vrije Universiteit Brussel (VUB - Belgium)
Prof. Dr. Ir. Iris De Graeve	Vrije Universiteit Brussel (VUB - Belgium)
Prof. Dr. Oscar Rosa Mattos	Universidade Federal do Rio de Janeiro (UFRJ - Brazil)
Prof. Dr. Hercílio Gomes de Melo	Universidade de São Paulo (USP - Brazil)
Dr. Krista Van den Bergh	OCAS n.v. - Arcelor Mittal (Belgium)
Dr. Reynier Inocente Revilla Castillo	Vrije Universiteit Brussel (VUB - Belgium)

### **Substitutes**

Prof. Dr. Rodolfo Politano	Instituto de Pesquisas Energéticas e Nucleares (IPEN - Brazil)
Prof. Dr. Zehbour Panossian	Instituto de Pesquisas Tecnológicas do Estado de São Paulo (IPT - Brazil)
Prof. Dr. Vanessa de Freitas Cunha Lins	Universidade Federal de Minas Gerais (UFMG - Brazil)

## ACKNOWLEDGMENTS

I faced the PhD as a long journey in which I have met so many people who helped me somehow to “arrive in the final destination”, the end of the PhD. I will try to express, in words, my huge gratitude to the people who contributed for this PhD either directly or indirectly.

I think it is fair starting with my sincerely thanks to the people who pushed me through my own limits, who had the patience to guide me throughout this PhD, my supervisors: Prof. Jesualdo Rossi, Prof. Herman Terryn and Dr. Reynier Revilla. I am very grateful for all the opportunities Prof. Jesualdo gave to me; perhaps, the most important one was allowing me to do part of the PhD abroad. Prof. Herman Terryn, thank you so much for having accepted me to be part of SURF group, for making this joint PhD possible and for guiding me through the complex corrosion world. I was also very lucky to have the help of Dr. Reynier Revilla from the very beginning of my staying at SURF. I felt so happy when I heard you would officially become my supervisor. Thank you for your huge patience of teaching and correcting all my first drafts (a trick task).

My sincerely thanks also go to Prof. Iris De Graeve, Prof. Isolda Costa and Prof. Zehbour Panossian. Thanks for sharing so much about your knowledge, experiences and tips through our many discussions. For me, you also represent the strength of women in science!

There was a person responsible for the beginning of this PhD: Prof. Marco Colosio, my bachelor’s supervisor. He was the first one who encouraged me to start this PhD and he continued following my progress up. Colosio, I am indebted to you for your support.

I would like to thank Prof. Rodolfo Politano who was willing to help me at any moment. Besides all the discussions filled up by a lot of philosophy, I am also grateful for your friendship.

Bart, Kitty, Marc, Marnix, Oscar and Priya, thank you so much for helping with the samples’ preparation, fixing the IT problems, or helping with the measurements.

Carine, Annette and Katrien “*I need help... can you help me*” ...probably, you heard it from me many times. Even though, you were always so kind and willing to help me and sorting out all the bureaucratic issues.

I have met so many people at IPEN through these 5 years, and some of them were always standing there, it did not matter why. Thanks Barbara, Larissa Berbel and Maicon for our amazing friendship.

At SURF, I was super welcomed, and I am very grateful for all the people that I have met. They made my days in Brussels easier and happier. Thank you for sharing with me your cultures, your experiences and also for all the coffees, sweets, lunches and drinks together. Of course, I cannot close this paragraph before expressing my deeply gratitude to Katrien and Monika. I could not have had best officemates. Thank you so much for the friendship that we have built. It was a pleasure to share the daily life moments with you.

Life was way easier in Brussels from the moment that I met my “Big Brazilian Community”: Caio and Marina. We were in the same situation: abroad to do a PhD. We faced everything together, from rough time to unforgettable funny situations. We have become family, and family is always there!

Even far from my homeland, I felt like home every day in Brussels thanks to my lovely flatmates: Charlie, Melinda and Momo. Girls, what a strong bond we have built...such a beautiful friendship that I will carry forever with me. I will never forget how much you supported me during this PhD, encouraging me and celebrating the achievements together.

I cannot forget to mention my friends who also supported me from the day 1 of this PhD, and also helped me to “escape” of the PhD reality when it was necessary. Diogo, Gabrielle, Kleber, Lucas, Talita and Victor. Thanks for always being around!

To all my relatives: grandparents, aunties, uncles and cousins. Thank you for caring so much about me and always giving me all the love.

To my cousin, Guilherme, who I consider as the oldest brother. Gui, thanks for, literally, being next to me all these years. When I was feeling exhausted, you pushed and encouraged me to keep going with focus and determination.

To my brother, Gabriel, the best “gift” my parents gave me; the one who really knows how to make me laugh. Behind that stubborn guy, I always find happiness and love.

Finally, I ask the permission of the reader to switch to Portuguese this last paragraph. I dedicate it to my parents, Marisa and Amaury who have supported all my decisions. *Mãe e Pai, eu queria que as poucas palavras aqui escritas conseguissem refletir*

*toda a gratidão que eu sinto por ter vocês ao meu lado durante todas as caminhadas da vida. Obrigada por acreditarem em mim e por apoiarem as minhas decisões. Obrigada por terem me ensinado os principais valores da vida. Eu amo muito vocês!*

*Obrigada a todos que acreditaram em mim!*

Thanks to all the ones who believed in me!

Camila Pucci Couto

COUTO, Camila P. **The effect of hot-stamping process on the local electrochemical behaviour of the 22MnB5 steel coated with hot-dip aluminium-silicon.** 2021. 170 p. Tese (Doutorado em Tecnologia Nuclear), Instituto de Pesquisas Energéticas e Nucleares, IPEN-CNEN/SP, São Paulo.

### ABSTRACT

Press-hardened steel (PHS) is a strategic steel for the automotive industry. The application of this type of steel in the vehicle structure allows safety improvement, mass reduction and less fuel consumption. Due to its ultra-high-tensile strength, the PHS components are produced by means of hot-stamping process. Hot stamping is a thermo-mechanical process in which a steel blank is heated at austenitisation temperatures and then is transferred to a press tool, where the material is formed and quenched simultaneously. The steel substrate is often protected with metallic coatings prior to hot stamping to avoid its oxidation and decarburisation. Zinc and aluminium based systems are often used as coatings for automotive applications. However, for hot stamping, the hot-dip aluminium-silicon (Al-Si) system is the most widespread and used. This coating presents good corrosion and oxidation resistance at high temperatures. However, during hot stamping, the initial microstructure and chemical composition of the metallic coating changes completely due to diffusion. These microstructural and compositional changes take place in the austenitisation step. Hence, after hot stamping the whole coating layer becomes a complex multi-layered system in which the sublayers are enriched in either aluminium or iron/silicon. Consequently, the coating properties, including the corrosion properties, also change after hot stamping. However, little is known about the effect of the morphological and compositional changes of the Al-Si coating due to the thermo-mechanical process on its corrosion behaviour and performance. The different sublayers in the coating form different micro-galvanic-couplings, which can affect the global electrochemical behaviour of the system. Therefore, a detailed approach based on local electrochemical techniques was suggested to evaluate the role that each sublayer plays on the electrochemical behaviour. This work aimed at evaluating the effect of the hot-stamping process on the electrochemical behaviour of 22MnB5 coated with hot-dip Al-Si (10 % Si in mass fraction). The morphology-composition of the layered structure was obtained using field emission scanning electron microscopy (FE-SEM) combined with energy dispersive X-ray spectroscopy (EDS). Global corrosion properties were evaluated by

open circuit potential (OCP), linear sweep voltammetry (LSV) and accelerated corrosion test. Nonetheless, the effect of each sublayer of the coating-steel system, on the electrochemical behaviour was investigated on a local scale by two complementary techniques: scanning Kelvin probe force microscopy (SKPFM) and electrochemical micro cell. The former was carried out in the samples' cross-section and it shows high lateral resolution, while the latter was done from the top surface in a depth profile approach. Thus, it enabled the local potentiodynamic polarisation in an isolated sublayer. The results obtained during the implementation of this work highlight the high complexity of the Al-Si coating-steel system (composed of several layers), which in turn supports the need for local investigations. The morphology and composition of the coating were shown to be greatly influenced by the hot-stamping process (parameters) and this resulted in considerable variations of the local corrosion and electrochemical behaviour of the coating-steel system.

Keywords: press-hardened steel, hot stamping, hot-dip aluminium-silicon, electrochemical behaviour

COUTO, Camila P. **O efeito do processo de estampagem a quente no comportamento eletroquímico local do aço 22MnB5 revestido com alumínio-silício por imersão a quente**. 2021. 170 p. Tese (Doutorado em Tecnologia Nuclear), Instituto de Pesquisas Energéticas e Nucleares, IPEN-CNEN/SP, São Paulo.

## RESUMO

O aço endurecido por prensagem (PHS- do inglês, *press-hardened steel*) é um aço estratégico para a indústria automotiva. A aplicação desse tipo de aço na estrutura do veículo permite melhoria da segurança, redução de massa e menor consumo de combustível. Devido à sua ultra-alta resistência à tração, os componentes de PHS são produzidos por meio do processo de estampagem a quente. A estampagem a quente é um processo termo-mecânico no qual um branco de aço é aquecido a temperaturas de austenitização e então é transferido para uma ferramenta de prensagem, onde o material é conformado e temperado simultaneamente. O substrato de aço é frequentemente protegido com revestimentos metálicos antes da estampagem a quente para evitar sua oxidação e decarbonetação. Os sistemas baseados em zinco e alumínio são frequentemente usados como revestimentos para aplicações automotivas. No entanto, para estampagem a quente, o sistema de alumínio-silício por imersão a quente (Al-Si) é o mais difundido e utilizado. Este revestimento apresenta boa resistência à corrosão e oxidação em altas temperaturas. No entanto, durante a estampagem a quente, a composição química e microestrutural inicial do revestimento muda completamente devido à difusão. Essas mudanças microestruturais e composicionais ocorrem na etapa de austenitização. Portanto, após a estampagem a quente, toda a camada de revestimento se torna um sistema complexo de múltiplas camadas no qual as subcamadas são enriquecidas tanto em alumínio como em ferro/silício. Consequentemente, as propriedades do revestimento, incluindo as propriedades de corrosão, também mudam após a estampagem a quente. No entanto, pouco se sabe sobre o efeito das mudanças morfológicas e composicionais do revestimento de Al-Si devido ao processo termo-mecânico sobre seu comportamento e desempenho à corrosão. As diferentes subcamadas no revestimento formam diferentes acoplamentos micro-galvânicos, que podem afetar o comportamento eletroquímico global do sistema. Portanto, uma abordagem detalhada baseada em técnicas eletroquímicas locais foi sugerida para avaliar o papel que cada subcamada desempenha no

comportamento eletroquímico. Este trabalho teve como objetivo avaliar o efeito do processo de estampagem a quente no comportamento eletroquímico do aço 22MnB5 revestido com Al-Si por imersão a quente (10% Si em fração de massa). A morfologia-composição da estrutura em camadas foi obtida usando microscopia eletrônica de varredura por emissão de campo (FE-SEM- do inglês, *field emission-scanning electron microscopy*) combinada com espectroscopia de energia dispersiva de raios X (EDS- do inglês, *energy dispersive X-ray spectroscopy*). As propriedades de corrosão global foram avaliadas por potencial de circuito aberto (OCP- do inglês, *open circuit potential*), voltametria de varredura linear (LSV- do inglês, *linear sweep voltammetry*) e teste de corrosão acelerada. No entanto, o efeito de cada subcamada do sistema revestimento-aço no comportamento eletroquímico foi investigado em escala local por duas técnicas complementares: microscopia de varredura de força por sonda Kelvin (SKPFM- do inglês, *scanning Kelvin probe force microscopy*) e microcélula eletroquímica. O primeiro foi realizado na seção transversal das amostras e apresenta alta resolução lateral; enquanto o último foi feito a partir da superfície superior em uma abordagem de perfil de profundidade. Desta forma, isso permitiu a polarização potenciodinâmica local em uma subcamada isolada. Os resultados obtidos durante a implementação deste trabalho destacam a alta complexidade do sistema de revestimento de aço Al-Si (composto por várias camadas), o que por sua vez suporta a necessidade de investigações locais. A morfologia e a composição do revestimento mostraram ser bastante influenciadas pelo processo de estampagem a quente (parâmetros) e isso resultou em variações consideráveis da corrosão local e do comportamento eletroquímico do sistema revestimento-aço.

Palavras-chave: aço endurecido por prensagem, estampagem a quente, alumínio-silício por imersão a quente, comportamento eletroquímico.

COUTO, Camila P. **Het effect van het hot stamping proces op het lokale elektrochemisch gedrag van 22MnB5 staal met een hot-dip aluminium-silicium coating**, 2021. 170 p. Tese (Doutorado em Tecnologia Nuclear), Instituto de Pesquisas Energéticas e Nucleares, IPEN-CNEN/SP, São Paulo.

## SAMENVATTING

*Press-hardened steel* (PHS) is een strategische staalsoort voor de automobiellindustrie. De toepassing van dit type staal in de voertuigstructuur maakt een verbetering van de veiligheid, een vermindering van de massa en een lager brandstofverbruik mogelijk. Wegens hun ultrahoge treksterkte worden PHS-onderdelen vervaardigd door middel van een *hot stamping* proces. *Hot stamping* is een thermo-mechanisch proces waarbij een staalplaat wordt verhit tot austenitiserings temperatuur en vervolgens wordt overgebracht op een perswerktuig, waar het materiaal gelijktijdig wordt gevormd en uitgehard. Het staalsubstraat wordt voor de *hot stamping* vaak beschermd met metaalcoatings om oxidatie en ontkoling te voorkomen. Zink en aluminium gebaseerde coatings worden vaak gebruikt voor toepassingen in de automobielsector. Voor *hot stamping* is het hot-dip aluminium-silicium (Al-Si)-systeem het meest gangbaar en gebruikt. Deze coating biedt een goede weerstand tegen corrosie en oxidatie bij hoge temperaturen. Tijdens de *hot stamping* veranderen de oorspronkelijke microstructuur en de chemische samenstelling van de metaalcoating echter volledig ten gevolge van diffusie. Deze veranderingen in de microstructuur en de samenstelling vinden plaats tijdens de austenitisatie. Door *hot stamping* wordt de gehele deklaag een complex systeem met meerdere lagen, waarin de sublagen verrijkt zijn, hetzij met aluminium, hetzij met ijzer/silicium. Als gevolg van *hot stamping* veranderen ook de coating-eigenschappen en de corrosie-eigenschappen. Er is echter weinig bekend over het effect van de morfologische en chemische veranderingen op het corrosiegedrag en de prestaties van de Al-Si coating ten gevolge van het thermo-mechanische proces. De verschillende sublagen in de coating vormen verschillende micro-galvanische koppelingen, die het algehele elektrochemische gedrag van het systeem kunnen beïnvloeden. Daarom werd een gedetailleerde aanpak voorgesteld op basis van lokale elektrochemische technieken om de rol te evalueren die elke sublaag speelt op het elektrochemisch gedrag. Dit werk heeft als doel het effect van het *hot stamping* proces op het elektrochemisch gedrag van 22MnB5

met een hot-dip Al-Si (10 % Si in massafractie) coating te evalueren. De morfologie en samenstelling van de gelaagde structuur werd bestudeerd met behulp van *field emission scanning electron microscopy* (FE-SEM) in combinatie met *energy dispersive X-ray spectroscopy* (EDS). De corrosie-eigenschappen werden geëvalueerd door middel van *open circuit potential* (OCP), *linear sweep voltammetry* (LSV) en versnelde corrosietest. Het effect van elke sublaag van het coating-staalsysteem op het elektrochemisch gedrag werd op lokale schaal onderzocht met twee complementaire technieken: *scanning Kelvin probe force microscopy* (SKPFM) en elektrochemische microcel. De eerstgenoemde techniek werd uitgevoerd in de dwarsdoorsnede van de monsters en vertoonde een hoge laterale resolutie, terwijl de tweede techniek werd uitgevoerd vanaf het bovenoppervlak in een diepteprofielbenadering. Op deze manier werd de lokale potentio-dynamische polarisatie in een geïsoleerde sublaag mogelijk gemaakt. De resultaten verkregen tijdens de uitvoering van dit werk benadrukken de hoge complexiteit van het Al-Si coating-staal systeem (samengesteld uit verschillende lagen), wat op zijn beurt de noodzaak van lokale onderzoeken ondersteunt. De morfologie en samenstelling van de coating bleken sterk beïnvloed te worden door het *hot stamping* proces (parameters) en dit resulteerde in aanzienlijke variaties van het lokale corrosie- en elektrochemische gedrag van het coating-staalsysteem.

Trefwoorden: *press-hardened steel*, *hot stamping*, hot-dip aluminium-silicium, elektrochemisch gedrag.

## LIST OF ACRONYMS

<b>Acronyms</b>	<b>Description</b>
AHSS	Advanced high-strength steel
AR	As received
BIW	Body-in-white
BSE	Backscattered electrons
CE	Counter electrode
CPD	Contact-potential difference
EDS	Energy dispersive X-ray spectroscopy
FE-SEM	Field emission-scanning electron microscopy
FL	Free layer
GDOES	Glow discharge optical emission spectroscopy
HDA	Hot-dip aluminised steel
HOPG	Highly oriented pyrolytic graphite
HSS	High strength steel
IDL	Interdiffusion layer
LIDL	Lower interdiffusion layer
LNLS	National Synchrotron Light Laboratory (from Portuguese - <i>Laboratório Nacional de Luz Síncrotron</i> )
LSV	Linear sweep voltammetry
OCP	Open circuit potential
PHS	Press-hardened steel
RE	Reference electrode
SE	Secondary electrons
SKPFM	Scanning Kelvin probe force microscopy
SST	Salt spray test
SVET	Scanning vibration electrode technique
UHSS	Ultra-high strength steel
UIDL	Upper interdiffusion layer
WE	Working electrode
WHO	World Health Organization
XRD	X-ray diffraction

## LIST OF SYMBOLS

<b>Symbol</b>	<b>Description</b>
$d$	Interplanar distance
$e$	Electron charge
$E_{\infty}$	Infinity level
$E^*$	Corrosion potential
$E_{BD}$	Breakdown potential
$E_F$	Fermi level
$E_{vac}$	Vacuum level
$i_a$	Current density in the anodic branch
$n$	Order of reflection
$Z$	Atomic number
$\Delta E^*$	Corrosion-potential difference
$\Delta\Psi$	Volta-potential difference
$\mu$	Metastable phase
$\theta$	Incidence angle
$\lambda$	Wavelength
$\Phi$	Work function

## LIST OF FIGURES

Figure 1.1 - Thesis outline showing the three major parts subdivided in chapters.....	34
Figure 2.1 - Diagram of the main steel grades used in automotive industry showing tensile strength versus elongation .....	35
Figure 2.2- Schematic illustration of the two existing modes of hot stamping process showing the main steps: a) direct hot stamping; b) indirect hot stamping.....	37
Figure 2.3 - 22MnB5 steel continuous cooling transformation diagram .....	39
Figure 3.1 -Schematic representation of the different interactions between the electron beam and the sample .....	48
Figure 3.2- General schematic experimental approach used to characterise either the surface or cross section of the different sample conditions (AR - before hot stamping and PHS - after hot stamping) .....	55
Figure 4.1 - Optical microscopic images showing the conditions of the coating layer of (a) AR and (b) PHS, just after the metallographic procedures.....	58
Figure 4.2 - Scanning backscattered electron image showing the surface morphology of 22MnB5 steel coated with Al-Si (10 % Si in mass fraction) composed of precipitates, and semi-quantitative EDS analyses of the whole are scanned, and regions 1 and 2 .....	58
Figure 4.3 - Scanning backscattered electron image showing the surface morphology of press-hardened 22MnB5 steel coated with Al-Si (10 % Si in mass fraction), highlighting the cracks (dashed lines) and the white particles (contamination), and the semi-quantitative EDS analyses.....	59
Figure 4.4 - Cross section morphology of as-received 22MnB5 steel coated with hot-dip Al-Si (Si 10% in mass fraction): (a) scanning backscattered image showing the main different constituents in the coating layer and an inset image highlighting the interface between coating layer and steel substrate; (b) EDS elemental mapping for O, Al, Si and Fe; (c) EDS point ID representing the semi-quantitative composition of the areas highlighted in (a)....	61
Figure 4.5 - Cross section morphology of press-hardened 22MnB5 steel coated with hot-dip Al-Si (Si 10 % in mass fraction): (a) scanning backscattered image showing the main different constituents in the coating layer; (b) EDS point ID representing the semi-quantitative composition of the highlighted areas in (a); (c) EDS elemental mapping for O, Al, Si and Fe .....	62

Figure 4.6 - Phase diagrams either binary or ternary of: (a) Al-Si; (b) Al-Fe; (c) Al-Fe-Si isothermal section at 600 °C; (d) Al-Fe-Si isothermal section at 727 °C; (e) Al-Fe-Si isothermal section at 800 °C .....	64
Figure 4.7 - Schematic diagram of the changes on Al-Si coating morphology due to the chemical diffusion as a function of hot-stamping parameters illustrating the formation of intermetallic sublayers .....	66
Figure 5.1 - Electrochemical tests in a 5 % NaCl solution (% in mass fraction): (a) evolution of <i>OCP</i> for 1 h; (b) linear sweep voltammetry for the AR, bare steel and PHS samples ....	70
Figure 5.2 - Scanning secondary electron images of the surface before and after immersion in 3.5 % NaCl (%in mass fraction): (a) AR sample before immersion; (b) AR sample after 2 h of immersion and an inset image from the attacked area; (c) PHS before immersion; (d) PHS after 2 h of immersion and an inset image from a randomly area in the surface at higher magnification .....	72
Figure 5.3 - Cross-section of 22MnB5 steel coated with hot-dip Al-Si prior hot-stamping process: (a) topographic map; (b) Volta potential map; (c) Volta potential line profile .....	73
Figure 5.4 - Histogram of Volta-potential distribution, based on the Volta-potential map of the AR sample, showing the contribution of the three main areas: steel substrate, interdiffusion layer and the aluminium coating matrix (free layer).....	74
Figure 5.5 - Cross-section of hot-stamped 22MnB5 steel coated with hot-dip Al-Si (a) topographic map; (b) Volta potential map showing the different sub layers present in the coating; (c) Volta potential line profile.....	75
Figure 5.6 - Histogram of Volta potential distribution, based on the cross-section Volta potential map, of the PHS sample, showing the contribution of the steel substrate and the two different sublayers: Al rich and Fe/Si rich.....	76
Figure 5.7 - Average Volta potential difference between as received Al-Si and PHS steel substrates measured versus the reference material .....	77
Figure 6.1 - Schematic experimental approach used during the depth-profile local electrochemical measurements, showing the influence of the hot-stamping process on the 22MnB5 steel coated with hot-dip Al-Si .....	84
Figure 6.2- GDOES profiles for AR sample. (a) sputtering time profile showing by dashed lines the craters obtained after 50 s, 100 s, 250 and 300 s of sputtering; (b) depth profile	

showing the craters obtained as a function of their depth and elemental chemical composition for Al, Si, Fe and O.....	85
Figure 6.3 - GDOES profiles for PHS condition. (a) sputtering time profile showing by dashed lines the craters obtained after 70 s, 140 s, 280 and 400 s of sputtering; (b) depth profile showing the craters obtained as a function of their depth and elemental chemical composition for Al, Si, Fe and O.....	86
Figure 6.4 - Anodic potentiodynamic polarisation curves in 0.1 mol·L <sup>-1</sup> NaCl solution acquired by means of electrochemical micro-cell as a function of the depth and also at the surface for as received 22MnB5 steel coated with hot-dip Al-Si (10 % Si in mass fraction) .....	88
Figure 6.5 - Anodic potentiodynamic polarisation curves in 0.1 mol·L <sup>-1</sup> NaCl solution acquired by means of electrochemical micro-cell in different positions of coating layer and steel substrate for as press-hardened 22MnB5 steel (PHS) coated with hot-dip Al-Si .....	89
Figure 6.6 - Schematic diagram of the proposed corrosion mechanism for 22MnB5 steel coated with hot-dip Al-Si (Si 10 % in mass fraction) showing: (I) initial condition of the system, absent of defects at the surface in which the native oxide layer acts as a protective barrier; (II) damage at the surface and the beginning of the corrosion process of the coating matrix (free layer) localised around the precipitates; (III) damage reaches the interdiffusion layer and the coating matrix play a role of sacrificial anode, corroding preferentially; (IV) the steel substrate is exposed and it corrodes similarly to the interdiffusion layer; moreover, the corrosion process of the coating matrix enhances .....	93
Figure 6.7 - Schematic diagram showing the proposed corrosion mechanism for press-hardened 22MnB5 steel coated with hot-dip Al-Si from: (I) initial condition of the system which already shows several damages at the surface and in the coating layer; (II) as the oxide layer plays a role of protective barrier, the coating sublayers start to corrode, but the corrosion of the Al-rich sublayers is more pronounced as they could behave as sacrificial anode to the Fe/Si-rich layer and the IDL; (III) the coating layer provides a barrier protection to the steel substrate; when it is exposed it corrodes as much as the Al-rich sublayers due to their similar corrosion potential and corrosion rate .....	97
Figure 7.1 - Surface of samples under SST conditions: (a) AR after one day, highlighting the initial scratches; (b) AR after one week, showing pits; (c) AR after two weeks; (d) AR after	

three weeks, pointing out dark (D), light (L) grey and brown (B) areas; (e) PHS after one day showing the growth of reddish-brownish rust at the sample surface; (f) PHS after one week; (g) PHS after two weeks; (h) PHS after three weeks showing the surface completely covered by rust.....	102
Figure 7.2 - SEM secondary electron images for the cross sections of AR samples as: (a) initial condition; (b) one week after SST; (c) two weeks after SST; (d) three weeks after SST showing the probable areas of pitting corrosion by means of dashed circles; (e) semi-quantitative EDS analyses of the sample cross section after three weeks under SST .....	103
Figure 7.3 – SEM secondary electron images for the cross sections of PHS samples as: (a) initial condition; (b) one week after SST; (c) two weeks after SST; (d) three weeks after SST; (e) higher magnification image of the sample cross section after three weeks under SST; (f) semi-quantitative EDS analyses of the sample cross section showed in Figure 7.3 (e) ....	104
Figure 7.4 - Raman spectra of the corrosion products formed at the surface of AR sample after SST; (a) mixture of silicon and bayerite; (b) silicon; (c) amorphous hydroxides mixture; (d) mixture of silicon and bayerite showing its most characteristic peaks magnified; (e) lepidocrocite found only after three weeks under SST .....	106
Figure 7.5 - Raman spectra of the corrosion products formed at the surface of PHS sample after SST; (a) mixture of iron-based compounds after one week under SST; (b) presence of magnetite after one week under SST; (c) mixture of iron-based compounds after two weeks under SST conditions; (d) mixture of iron-based compounds after two and three weeks under SST conditions.....	107
Figure 8.1 - Scanning backscattered electron images showing the cross-section morphologies of 22MnB5 steel coated with hot-dip Al-Si (10 % Si in mass fraction) in different conditions highlighting the different intermetallic phases present in: (a) AR; (b) PHS850; (c) PHS900; and (d) PHS950 .....	116
Figure 8.2 - EDS analyses: (a) punctual identification for the positions highlighted in Figure 8.1; and EDS elemental mappings for Al, Fe, Si and O of (b) AR; (c) PHS850; (d) PHS900; (e) PHS950.....	117
Figure 8.3 - Electrochemical measurements for AR, PHS850, PHS900 and PHS950 in NaCl 5 % solution (in mass fraction): (a) open circuit potential evolution for 1 h; (b) anodic polarisation curves obtained by means of linear sweep voltammetry .....	119

Figure 8.4 - Cross-section image of AR sample measured by means of SKPM: (a) topographic map; (b) Volta-potential map; (c) Volta-potential line profile for the line indicated in (b).....	121
Figure 8.5 - Cross-section image of PHS850 sample measured by means of SKPM: (a) topographic map; (b) Volta-potential map; (c) Volta-potential line profile for the line indicated in (b).....	122
Figure 8.6 - Cross-section image of PHS900 sample measured by means of SKPM: (a) topographic map; (b) Volta-potential map; (c) Volta-potential line profile for the line indicated in (b).....	123
Figure 8.7 - Cross-section image of PHS950 sample measured by means of SKPM: (a) topographic map; (b) Volta-potential map; (c) Volta-potential line profile for the line indicated in (b).....	124
Figure 8.8 - Histograms based on the Volta-potential map highlighting the contribution of different phases for: (a) AR; (b) PHS850; (c) PHS900; (d) PHS950 .....	125
Figure 8.9 - Average Volta potential of the steel substrate as function of different austenitisation temperatures.....	127
Figure 8.10 - Schematic overview representing the changes in the Al-Si coating morphology as function of temperature: (a) AR condition; (b) AR condition at austenitisation temperatures showing the melted coating layer and the solid intermetallics; (c) coating morphology austenitised at 850 °C; (d) coating morphology austenitised at 900 °C; (e) coating morphology austenitised at 950 °C .....	128
Figure 8.11 - Average Volta potential of the coating layer, the steel substrate, and the difference between them ( $\Delta\Psi$ ) for each sample condition: AR, PHS850, PHS900 and PHS950 .....	129
Figure 9.1- <i>In loco</i> apparatus for <i>in-situ</i> synchrotron X-ray diffraction integrated to (a) XRD2 beam line at LNLS highlighting (b) monitoring cell and (c) electrolyte injector.....	133
Figure 9.2 - Detailed specifications of (a) monitoring cell and (b) electrolyte injector, showing the dimensions in mm and scale 1:1.....	134
Figure 9.3 - Sequence of diffraction patterns for AR sample condition. Each cycle consists of immersing the sample in NaCl 3.5% (mass fraction) for 20 min and 40 min of exposure to the air for the measurements.....	136

Figure 9.4 - Sequence of diffraction patterns for PHS sample condition. Each cycle consists of immersing the sample in NaCl 3.5% (mass fraction) for 20 min and 40 min of exposure to the air for the measurements ..... 137

Figure 9.5 - Schematic diagram for a generic coated sample representing the steps of immersion and measurements by X-ray diffraction. The alternating procedure promotes the formation and growth of corrosion products at the top surface of the sample ..... 141

Figure 10.1 - Overview of the main findings related to the effect of hot stamping on the Al-Si coating structure-composition and the consequent effect on the corrosion properties . 152

## LIST OF TABLES

Table 2.1 - Boron-manganese steel grades used for hot-stamping applications showing the maximum % of the alloy elements (% in mass fraction).....	38
Table 2.2 - Advantages and challenges related to alternative coatings systems for hot-stamping applications .....	41
Table 3.1 - Nominal chemical composition of 22MnB5 steel in terms of maximum % in mass fraction.....	46
Table 3.2 - Samples' identification and their corresponding conditions .....	47
Table 5.1 - Average values of <i>OCP</i> , <i>E*</i> and their corresponding standard deviation values for bare steel, AR and PHS samples in 5.0 % NaCl solution (% in mass fraction).....	71
Table 6.1 - Average <i>E*</i> , <i>E<sub>BD</sub></i> , and their corresponding standard deviations, determined from anodic potentiodynamic polarisation curves in 0.1 mol·L <sup>-1</sup> NaCl at the surface and different depths in the AR sample .....	88
Table 6.2 - Average <i>E*</i> , <i>E<sub>BD</sub></i> , and their standard deviation values, determined from anodic potentiodynamic polarisation curves in 0.1 mol·L <sup>-1</sup> NaCl at the surface and different depths in the PHS sample.....	90
Table 8.1 - Steel samples' identification and their corresponding experimental conditions .....	115
Table 8.2 - Average <i>OCP</i> , <i>E*</i> and their corresponding standard deviation values for AR, PHS850, PHS900 and PHS950 samples measured in 5% NaCl solution (in mass fraction) .....	120
Table 9.1 - Characterisation of the main peaks present in the sequence of diffraction pattern for the AR sample, indicating the most suitable phases .....	139
Table 9.2 - Characterisation of the main peaks present in the sequence of diffraction pattern for the PHS sample, indicating the most suitable phases .....	140

## CONTENTS

<b>ABSTRACT</b> .....	<b>ix</b>
<b>RESUMO</b> .....	<b>xi</b>
<b>SAMENVATTING</b> .....	<b>xiii</b>
<b>LIST OF ACRONYMS</b> .....	<b>xv</b>
<b>LIST OF SYMBOLS</b> .....	<b>xvi</b>
<b>LIST OF FIGURES</b> .....	<b>xvii</b>
<b>LIST OF TABLES</b> .....	<b>xxiii</b>
<b>CHAPTER 1 - Introduction and objective</b> .....	<b>29</b>
1.1 General introduction .....	29
1.2 Objective.....	32
1.2.1 Specific objectives .....	32
1.3 Outline .....	32
<b>CHAPTER 2 - Literature review</b> .....	<b>35</b>
2.1 Advanced-high strength steel.....	35
2.2 Hot stamping.....	36
2.3 Press-hardened steel.....	38
2.4 Coatings for press-hardened steel .....	40
2.4.1 Hot-dip aluminium-silicon.....	41
2.4.1.1 Formation and growth of intermetallic phases on hot-dip Al-Si .....	42
2.4.1.2 Corrosion mechanism of hot-dip Al-Si.....	43
2.5 Press-hardened steel coated with hot-dip Al-Si.....	44
<b>CHAPTER 3 - Materials and methods</b> .....	<b>46</b>
3.1 Materials and samples' preparation .....	46
3.2 Methods .....	47
3.2.1 Morphological and compositional analyses.....	48
3.2.1.1 Field emission-scanning electron microscopy (FE-SEM) combined with energy dispersive X-ray spectroscopy (EDS).....	48
3.2.1.2 Glow discharge optical emission spectroscopy (GDOES) .....	49
3.2.1.3 Raman spectroscopy .....	50
3.2.1.4 Synchrotron X-ray diffraction .....	50

3.2.2 Global electrochemical techniques .....	51
3.2.2.1 Open circuit potential.....	51
3.2.2.2 Polarisation curves .....	52
3.2.3 Accelerated corrosion test.....	52
3.2.4 Local electrochemical techniques .....	53
3.2.4.1 Scanning Kelvin probe force microscopy.....	53
3.2.4.2 Electrochemical micro cell .....	55
3.3 Overview.....	55
<b>CHAPTER 4 - The effect of hot stamping on Al-Si coating morphology .....</b>	<b>57</b>
4.1 Introduction.....	57
4.2 Experimental procedure .....	57
4.3 Results.....	58
4.3.1 Surface characterisation .....	58
4.3.2 Cross-section characterisation .....	60
4.4 Discussion .....	63
4.5 Conclusion .....	66
<b>CHAPTER 5 - Electrochemical behaviour of 22MnB5 steel coated with hot-dip Al-Si before and after hot-stamping process investigated by means of scanning Kelvin probe microscopy .....</b>	<b>68</b>
5.1 Introduction.....	68
5.2 Experimental procedure .....	68
5.2.1 Global electrochemical measurements and immersion tests .....	68
5.2.2 Scanning Kelvin probe microscopy .....	69
5.3 Results.....	69
5.3.1 Electrochemical measurements.....	69
5.3.2 Immersion test.....	71
5.3.3 Scanning Kelvin probe force microscopy.....	73
5.4 Discussion .....	77
5.5 Conclusion .....	81

<b>CHAPTER 6 - Depth profiling approach to evaluate the influence of hot stamping on the local electrochemical behaviour and galvanic series of hot-dip Al-Si coating on 22MnB5 steel .....</b>	<b>82</b>
6.1 Introduction.....	82
6.2 Experimental procedure .....	83
6.2.2 Electrochemical micro cell .....	83
6.3 Results.....	84
6.3.1 GDOES depth profile.....	84
6.3.2 Local anodic potentiodynamic polarisation using electrochemical micro cell as a function of depth.....	87
6.4 Discussion.....	91
6.4.1 GDOES as a sample tool preparation .....	91
6.4.2 Local electrochemical measurements .....	92
6.4.3 Influence of hot stamping on the electrochemical depth profile.....	94
6.4.4 Influence of the electrolyte concentration on the electrochemical behaviour of the system before and after hot stamping .....	97
6.5 Conclusion .....	98
<b>CHAPTER 7 - Salt spray test and analysis of corrosion products by means of Raman spectroscopy for 22MnB5 steel coated with hot-dip Al-Si: the effect of hot stamping .....</b>	<b>100</b>
7.1 Introduction.....	100
7.2 Experimental procedure .....	101
7.2.1 Continuous salt spray test .....	101
7.2.2 Raman spectroscopy .....	101
7.3 Results.....	101
7.3.1 Macroscopic characterisation of corroded samples' surface after SST .....	101
7.3.2 Cross-section characterisation .....	102
7.3.3 Raman spectroscopy .....	105
7.4 Discussion.....	108
7.5 Conclusion .....	112

<b>CHAPTER 8 - Influence of different austenitisation temperatures during hot-stamping process on the local electrochemical behaviour of 22MnB5 steel coated with hot-dip Al-Si .....</b>	<b>114</b>
8.1 Introduction.....	114
8.2 Experimental procedure .....	114
8.3 Results.....	115
8.3.1 Cross-section coating characterisation as function of different austenitisation temperatures.....	115
8.3.2 Electrochemical measurements of the coated systems as function of austenitisation temperature .....	118
8.3.3 Scanning Kelvin probe force microscopy analyses .....	120
8.4 Discussion.....	127
8.5 Conclusion .....	130
<b>CHAPTER 9 - Use of Synchrotron based X-ray diffraction for monitoring <i>in situ</i> surface modifications of the Al-Si coated 22MnB5 steel for hot stamping as function of exposure in chloride containing solutions.....</b>	<b>132</b>
9.1 Introduction.....	132
9.2 Experimental procedure .....	133
9.2.1 Synchrotron X-ray diffraction .....	133
9.2.2 Phase analysis .....	135
9.3 Results.....	135
9.3.1 Synchrotron X-ray diffraction .....	135
9.3.2 Indexing patterns.....	138
9.4 Discussion.....	141
9.5 Conclusion .....	143
<b>CHAPTER 10 - Conclusion and outlook .....</b>	<b>147</b>
10.1 Conclusion .....	147
10.2 Outlook .....	153
<b>References.....</b>	<b>155</b>
<b>SUMMARY .....</b>	<b>164</b>
<b>RESUMO EXPANDIDO.....</b>	<b>167</b>

## **Part I**

Introduction, objective,  
literature review,  
materials and methods

## CHAPTER 1 - Introduction and objective <sup>1</sup>

### 1.1 General introduction

Environmental issues such as climate change have forced different industrial sectors to change their production strategies in order to achieve a more sustainable level. From the manufacturing segment, the automotive industry can be highlighted. A study has shown that the exhaust fumes from vehicles represent 30 % of the global gas emissions; from those, 17 % regarding the CO<sub>2</sub> emissions [1]. Carmakers have been planning actions in order to attend the worldwide requirements to reduce greenhouse gas emissions [2–4]. Simultaneously, they have to improve the safety of the new vehicles produced. According to the World Health Organization (WHO), unsafe vehicles have been pointed out as one of the reasons for the high number of deaths in road crashes [5].

Among all strategies to combine safety improvement and reduction on the greenhouse emissions, the lightweight design methods have been pointed out as one of the most efficient [2,3]. These methods include replacement of materials, as well as new manufacturing processes and joining technologies [2]. The lightweight design of the vehicle body-in-white (structure) may represents a decrease of around 30 % of the total vehicle mass [4]. The application of advanced-high-strength steels (AHSS) and ultra-high-strength steels (UHSS) in body-in-white (BIW) allows that the automotive industry attends the demands for lightweight structures, aiming at reducing fuel consumption and at improving safety and crashworthiness properties. Due to the reduced thickness and the higher tensile strength of AHSS and UHSS in comparison with conventional steels, they have become the current trend for new vehicles [6–9].

When tensile strength increases, the plastic forming of metals may decrease and a springback effect appears due to residual stresses. Consequently, in order to improve the

---

<sup>1</sup> This chapter is partially based on:

COUTO, C. P.; REVILLA, R. I.; COLOSIO, M. A.; COSTA, I.; PANOSSIAN, Z.; DE GRAEVE, I.; TERRYN, H.; ROSSI, J. L. Electrochemical behaviour of 22MnB5 steel coated with hot-dip Al-Si before and after hot-stamping process investigated by means of scanning Kelvin probe microscopy. *Corrosion Science*, v. 174, n. June, p. 108811, set. 2020. <https://doi.org/10.1016/j.corsci.2020.108811>

COUTO, C. P.; ANDREATTA, F.; LANZUTTI, A.; COSTA, I.; PANOSSIAN, Z.; DE GRAEVE, I.; TERRYN, H.; ROSSI, J. L.; REVILLA, R. I. Depth profiling approach to evaluate the influence of hot stamping on the local electrochemical behaviour and galvanic series of hot-dip Al-Si coating on 22MnB5 steel. *Corrosion Science*, 2021 <https://doi.org/10.1016/j.corsci.2021.109435>

formability of AHSS and UHSS, the hot-stamping process has been used as an alternative forming method [10]. Hot stamping is a thermo-mechanical process where the steel blank is heated for a few minutes at austenitisation temperatures and then, transferred from furnace to the press tool (die). The design of the die consists of a water cooling system which allows simultaneous forming and quenching of the steel blank [6,11–14]. As an industrial process, the austenitisation temperature, the soaking time, as well as the transfer time and the cooling rate may vary among manufactures. In previous studies, it had been found that the austenitisation temperatures vary from 880 °C to 950 °C, the soaking time varies from 3 min to 13 min, the transfer step may take 7 s maximum and the cooling rate must be at least 27 °C·s<sup>-1</sup> [6,7,15–18].

The boron-manganese steel has been pointed out as the most suitable material for the hot-stamping process [6]. The 22MnB5 is the steel grade widely used in automotive industries to produce hot-stamped components. Before the hot-forming process, the steel consists of a ferrite-pearlite microstructure and shows a tensile strength of about 600 MPa. At the end of the thermo-mechanical process the steel microstructure becomes fully martensitic and the tensile strength reaches approximately 1500 MPa [6,13,14,19,20]. Depending on the steel grade, the tensile strength may reach 2000 MPa at the end of the process [6]. Boron-manganese steel combined with the hot-stamping process is known as press-hardened steel (PHS). The production of PHS components has been increasing since early 2000 and the prediction is that, in the next few years, about 600 millions of PHS parts will be produced worldwide [21,22]. In fact, the carmakers have been presenting an increase of hot-stamping components in new vehicles. One of the carmakers have shown that 50 % of a new vehicle structure consists of UHSS, in which 15 % comprises of PHS [23].

PHS are usually protected with metallic coatings prior to hot stamping in order to avoid both scale formation and decarburisation [6,7,11,14,16,24]. Zinc-based coatings are often applied onto steel substrate [12,25,26]. The main advantage of these coating systems is related to the cathodic protection corrosion mechanism which guarantees the integrity of metallic components in an economical and safe way [27]. In this mechanism, the cathodic protection is achieved by supplying the electrons to the steel substrate (cathode). The driving force to provide cathodic protection is the difference of (corrosion) potential between the anode and the cathode. In this scenario, the anode is known as sacrificial anode, which is less noble than the cathode, and corrodes preferentially. The higher the potential difference, the higher the driving force for cathodic protection [27–30].

Despite the advantages of Zn-based systems, their main limitation for hot-stamping applications is the liquid-metal-induced embrittlement [21]. The austenitisation temperatures lead to the formation of liquid zinc which can penetrate into the steel matrix and therefore, promote irregular fracture [21]. Consequently, for hot-stamping applications a different metallic system has been used. The hot-dip aluminium-silicon (10 % Si in mass fraction) is the most widely applied metallic coating onto steel before hot stamping. This coating has already been used for exhaust systems, power generation plants and heating equipment due to its well-known corrosion and oxidation resistance at high temperatures [31,32].

The initial condition of the Al-Si coating consists of an aluminium matrix with cathodic precipitates and an interdiffusion layer enriched in iron. [8,16,31,33]. However, the coating structure changes during the hot-stamping process into a multi-layered system as a consequence of the diffusion which occurs during the austenitisation step. The coating's sublayers become enriched in either aluminium or iron/silicon. [8,16,19,24]. The structure of the coating is significantly influenced by some process parameters, such as austenitisation temperature and soaking time [19,34,35].

The corrosion properties of Al-Si coatings for hot stamping are still subject of investigation. Most of the published corrosion studies have used either standard electrochemical measurements or accelerated corrosion tests to evaluate the corrosion properties of coated PHS [7,11,26,36]. By means of cyclic corrosion tests, Dosdat et al. [11] have compared the corrosion resistance of Al-Si and Zn-based coatings (galvanised and galvanized) for hot-stamping applications. The results pointed out the Al-Si coating as the most suitable system for hot-stamping applications because Zn-based coatings are much more sensitive to the thermo-mechanical process parameters. Allély et al. [7] also evaluated the corrosion resistance of PHS coated with Al-Si using standard electrochemical tests and corrosion accelerated methods. They have shown that even considering that the Al-Si coating does not provide cathodic protection for the steel substrate, due to small potential differences between the steel substrate and the coating layer, it is a suitable coating system for hot stamping [7]. However, these methods only show the global behaviour of the system and they do not give any insights concerning the local electrochemical behaviour of the different sublayers present in the coating layer.

## 1.2 Objective

This work aimed at evaluating the influence of hot-stamping processes on the local corrosion properties of the 22MnB5 steel grade coated with hot-dip Al-Si (10 % Si in mass fraction).

The need for local electrochemical investigation is supported by the high complexity of these multi-layered systems, in which the morphology and composition of the sublayers, and the presence of defects (micro cracks and voids) is highly influenced by the process parameters. For this reason, a detailed approach combining complementary characterisation methods and local electrochemical techniques was carried out within the frame of this thesis. Understanding the electrochemical behaviour and the micro-galvanic relation between the different sublayers in the coating is of paramount importance. Since in the case of scratches or damage to the coatings, the different sublayers as well as the steel substrate may become exposed. This also relates to the exposure of cut-edge and issues related to joining-processes, such as welding and adhesives.

### 1.2.1 Specific objectives

- I. Evaluating the local electrochemical behaviour of the system (coating/substrate) in ambient conditions.
- II. Effect of an electrolyte exposure on the electrochemical behaviour of each sublayer using a depth profile approach and local electrochemical measurements.
- III. Corrosion damage of the system exposing it to severe conditions and characterisation of corrosion products nature.
- IV. Effect of different austenitisation temperatures during hot stamping on the electrochemical behaviour of the system.
- V. Feasibility study about the use of synchrotron X-ray diffraction to monitor *in situ* the sample surface under the effect of an electrolyte.

## 1.3 Outline

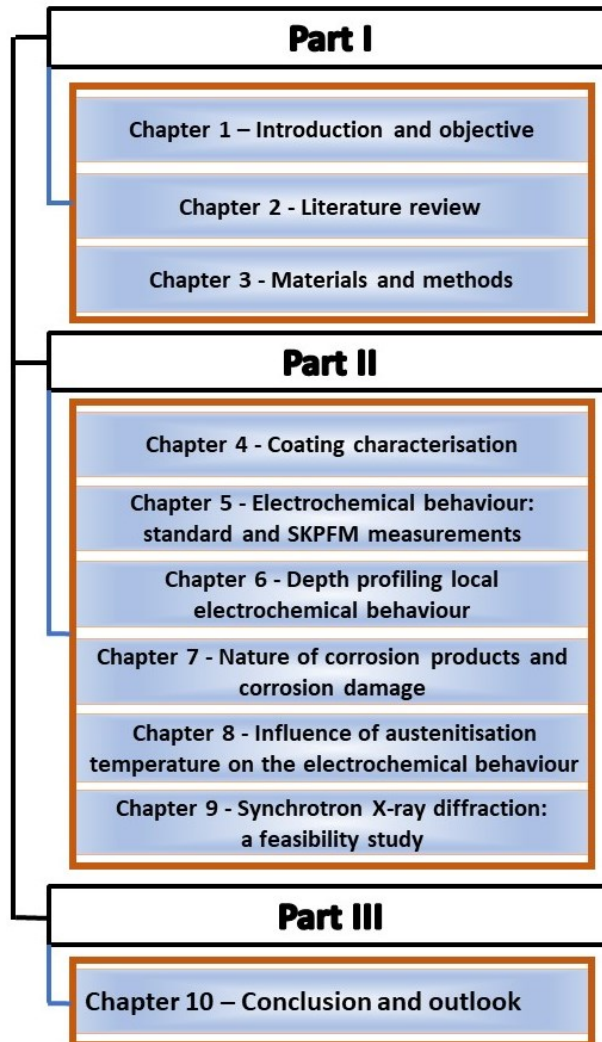
This doctorate thesis is divided in three major parts, as shown in Figure 1.1, which presents the general outline. Besides the general introduction and the presentation of the objectives in this research, Part I also includes a literature review about the main topics related to coated press-hardened steels in Chapter 2. Chapter 3 ends the Part I describing the samples used in

this research as well as providing a brief theoretical background of the main techniques used to characterise the influence of hot stamping on the Al-Si coatings.

Part II comprises the results and discussion, subdivided in six chapters. Chapter 4 shows the influence of hot stamping process on the morphology and composition of the Al-Si coating. The findings in this chapter support the discussion of the following chapters. Chapter 5 shows the influence of hot-stamping process on the electrochemical behaviour of the system (coating/steel), before and after hot stamping. Global and local electrochemical measurements were carried out. In Chapter 6, the electrochemical behaviour of each sublayer of the system was evaluated combining a depth profile approach with local electrochemical measurements. Chapter 7 shows the influence of hot stamping on the nature of corrosion products and on the coating corrosion damage. The same approach presented in Chapter 5 was used in Chapter 8 to evaluate the effect of different austenitisation temperatures on the electrochemical behaviour of the system. Finally, Chapter 9 is a feasibility study based on synchrotron X-ray diffraction to monitor *in situ* the influence of an electrolyte on the Al-Si coating, before and after hot stamping.

Part III closes this thesis with Chapter 10, presenting the conclusion and suggesting future works which could complement the present research.

Figure 1.1 - Thesis outline showing the three major parts subdivided in chapters



Source: Author

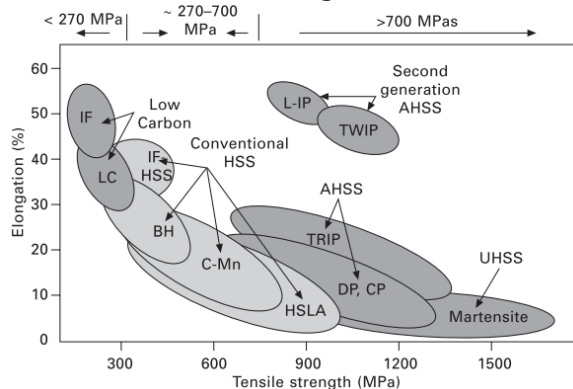
## CHAPTER 2 - Literature review

### 2.1 Advanced-high strength steel

The development of new steel grades has started in the early 1970's enhanced by the first petroleum crisis [37]. Since then, carmakers have been planning actions in order to meet the worldwide requirements to reduce greenhouse gas emissions [1]. Simultaneously, the safety of the new vehicles produced should be improved [10,14,38]. Among all strategies to combine sustainability- including environmentally friendly processes and products- and safety, the lightweight-design methods have been identified among the most efficient [3,14]. These methods include replacement of materials, as well as new manufacturing processes and joining technologies [14]. The lightweight design of the vehicle's structure may lead to decrease of approximately 30 % of the total vehicle mass [4].

Moreover, the use of these new grades allows safety/crashworthiness improvement. These key factors are achieved due to their higher-tensile strength and thinner thickness than the conventional steels [7,9–11,14,39]. Figure 2.1 shows the diagram which correlates the main steel grades used in automotive industry as function of their elongation (%) by their tensile strength (MPa).

**Figure 2.1 - Diagram of the main steel grades used in automotive industry showing tensile strength versus elongation**



Source: Horvath [37]

According to Figure 2.1, the steel grades are classified according to their tensile strength. Low carbon steels, also known as mild steels, show tensile strength lower than 270 MPa. They comprise the interstitial free (IF) and low carbon steels (LC). The conventional high-strength steel (HSS) grades present tensile strength from 270 MPa to 700 MPa. Interstitial free high-strength steels (IF-HSS), bake hardening (BH), carbon-

manganese (C-Mn), and high strength low alloys (HSLA) are examples of conventional HSS [37]. Either low carbon steels or conventional HSS are used for outer panels application (door skins, roof, hood and trunk) [40]. However, C-Mn and HSLA may also be considered as advanced-high strength steels if their tensile strengths reach up to 700 MPa. The AHSS comprise the following grades: dual phase (DP), complex phase (CP), transformation induced plasticity (TRIP), twinning induced plasticity (TWIP) and lightweight steels with induced plasticity (L-IP). These AHSS are used in the main structure and inner panels where high-tensile strength and formability are required. The martensitic steels are classified as ultra-high strength steels (UHSS), showing tensile strength above 1500 MPa [37].

The AHSS and UHSS have some disadvantages in comparison with the conventional steels related to the premature wear of tools, reduced formability and the tendency for springback phenomenon [10]. Consequently, the components obtained will present design, dimensions and even mechanical properties different from those projected [14,41,42].

In order to increase the steel plastic formability, to decrease the springback effects, forming methods are being under development, which include the use of high-temperatures processes, such as hot stamping [10,12,14,43].

## **2.2 Hot stamping**

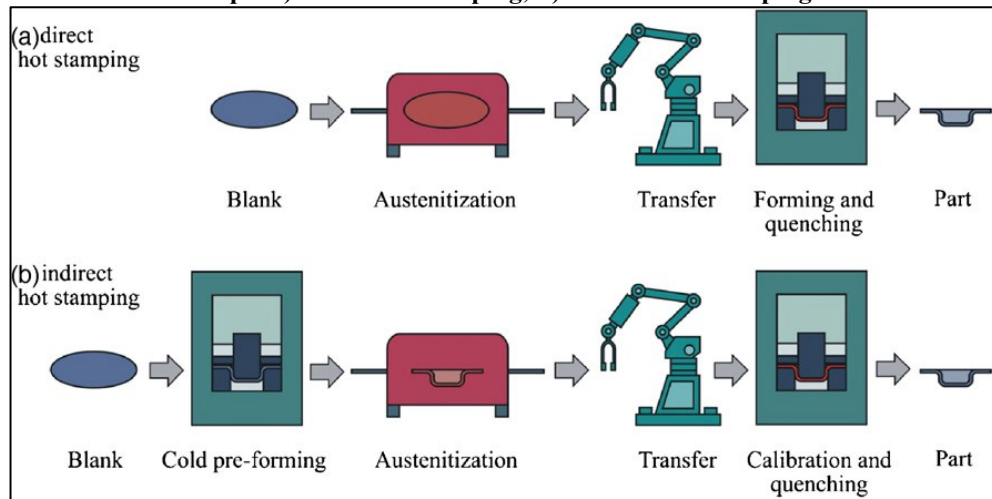
The hot-stamping process, also known as hot-press forming, press hardening or die quenching [15,18], is a non-isothermal process, widely applied for AHSS and UHSS, where the heated steel blank is formed and cooled down at the same time in a water-cooled die tool [9,10,17].

The hot-forming technology was developed and patented by the Swedish company Plannja Hard Tech in 1973 and in 1977, respectively [6,15,17,18]. As of 1984, the technology has been used to produce automotive components [6,17].

There are two different methods for hot stamping: the direct and indirect modes, as shown in Figure 2.2. The direct method (Figure 2.2 (a)) consists of heating the steel blank at austenitisation temperatures, and then transferring it from the furnace to the press tool for simultaneous forming and quenching of the material. The design of the die consists of a water-cooling system which allows that the steel blank is formed and quenched at the same time [6,11–14]. The difference between the direct and the indirect method is an additional

step, where the steel blank is pre-cold formed before the austenitisation in the indirect method, as seen in Figure 2.2 (b) [11]. Moreover, the indirect method is most used to produce parts with larger dimensions, complex design and for specific coating systems, such as zinc based. The indirect hot stamping enables lower process austenitisation temperatures in comparison with the direct method [6,18].

**Figure 2.2- Schematic illustration of the two existing modes of hot stamping process showing the main steps: a) direct hot stamping; b) indirect hot stamping**



Source: Karbasian et al. [6]

As an industrial process, the austenitisation temperature and the time, as well as the transfer time and the cooling rate may vary among the manufacturers. In previous studies, it had been reported that the process range for heating temperature is from 880 °C to 950 °C, the austenitisation time varies from 3 min to 13 min, the transfer step may take 7 s maximum and the cooling rate must be at least 27 K·s<sup>-1</sup>. This cooling rate is recommended to promote the fully martensitic transformation at the end of the process [6,7,15–18].

The main advantage of the thermo-mechanical process is to produce AHSS/UHSS components with the absence of springback. However, there are some drawbacks related to the current hot-stamping process [14]. It is an expensive process because of the equipment needed, mainly the furnaces and press tooling. In addition, these equipment require a very large structure due to their size. The maintenance of the equipment, mainly of the die, has a very high cost. Another drawback is regarding the use of one steel grade which leads to limited mechanical properties of the components, which are also used in limited applications: safety components [14].

Nonetheless, the hot-stamping process has been improved in order to diminish the current drawbacks. The development of new heating systems, such as resistances and

inductions, has led to a shorter heating time. Consequently, the process gets faster and the number of components produced increases. In addition, the mechanical properties of the components may be higher due to the new steel grades for hot stamping under development [14].

### 2.3 Press-hardened steel

Hot stamped boron-manganese steel components, also known as press-hardened steels (PHS), were used for the first time in a vehicle structure in 1984 by Saab Automobile AB [6,14]. However, its application has only become larger in structural vehicles applications from early 2000's [37]. Different boron-manganese steel grades have been developed, including the 20MnB5, 22MnB5, 27MnCrB5 and 37MnB4 [6]. They show slight differences in chemical composition as seen in Table 2.1, mainly related to the carbon, manganese and the chromium content.

**Table 2.1 - Boron-manganese steel grades used for hot-stamping applications showing the maximum % of the alloy elements (% in mass fraction)**

Steel	Al	B	C	Cr	Mn	N	Ni	Si	Ti
20MnB5	0.04	0.001	0.16	0.23	1.05	-	0.01	0.40	0.034
22MnB5	0.03	0.002	0.23	0.16	1.18	0.005	0.12	0.22	0.040
27MnCrB5	0.03	0.002	0.25	0.34	1.24	0.004	0.01	0.21	0.042
37MnB4	0.03	0.001	0.33	0.19	0.81	0.006	0.02	0.31	0.046

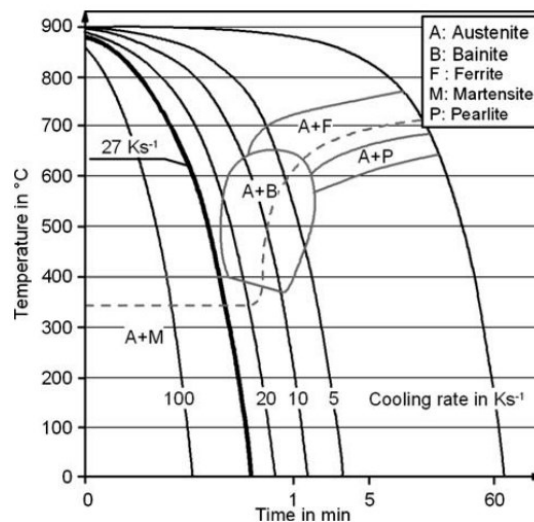
Source: Adapted from Karbasian et al. [6]

Each alloy element presented in Table 2.1 plays an important role on the steel properties. Hardenability, the ability of full martensite transformation [44], is the major property for PHS. The addition of carbon, chromium, manganese and boron content in the steel composition further the martensite transformation and suppress the formation of soft phases (ferrite and pearlite) [18]. The addition of boron has been pointed out as the most effective way to improve the steel hardenability, because just a little amount (in order of ppm) has a great effect on the martensite transformation. The proposed mechanism considers the drop of the interfacial energy at the grain boundaries as boron segregates towards these areas. Consequently, the nucleation of ferrite at the austenite grain boundaries is retarded [9,18,45]. On the other hand, boron has a high affinity with nitrogen which results on the formation of BN precipitates [18]. Thus, titanium and aluminium are added as alloying elements to promote the formation of AlN and TiN precipitates. Moreover, these precipitates segregate at the grain boundaries hindering their growth and consequent steel softness [18].

Although the steel chemical composition has an influence on the steel hardenability, the hot-stamping parameters must be considered to obtain a fully martensite microstructure at the end of the process. The austenitisation temperature and the cooling rate influence the final microstructure of the steel [9]. Considering the austenitisation temperature from 850 °C to 950 °C, for an hypoeutectoid steel (carbon content less than 0.76 % in mass fraction), only at temperatures above 912 °C the microstructure becomes fully austenitic, whereas at intercritical temperatures (between 723 °C and 912 °C), both ferrite and austenite co-exist. However, the higher the carbon content, the lower the ferrite volume fraction at this intercritical temperature. Therefore, a high-volume fraction of martensite can be obtained after quenching [44].

Martensite has a carbon super-saturated microstructure in which its transformation cannot be predicted by the equilibrium iron-cementite (Fe-Fe<sub>3</sub>C) diagram [44]. However, the continuous cooling temperature (CCT) diagrams show all the possible phases formation considering the cooling rate. Among the boron-manganese steel grades the 22MnB5 has been mostly applied for hot-stamping applications [9]. Its CCT diagram is shown in Figure 2.3. According to the diagram, the minimum cooling rate for 22MnB5 is 27 K · s<sup>-1</sup>.

**Figure 2.3 - 22MnB5 steel continuous cooling transformation diagram**



Source: Tekkaya et al. [46]

Due to the high temperatures during the hot-stamping process, the formation of oxides at the surface and the decarburisation of the steel can occur during the transfer of the blank from the furnace to the press tool [6,16,24]. The oxide layer formed has high hardness, which can promote premature wear of the stamping dies [16,24]. Conversely, the

decarburisation directly affects the final properties of the component, since carbon in combination with atmospheric oxygen ceases to exercise its steel hardening function [6,7,11,18,20,47,48]. The formation of a thermal oxide scale onto bare steel surface besides causing deleterious damage to the press tool it also reduces the painting adhesion. For these reasons an additional production step, such as blasting, is often carried out [24]. However, an additional step increases the product cost [11]. As an alternative, the steel was protected with metallic coatings prior hot stamping.

#### **2.4 Coatings for press-hardened steel**

Different metallic coating systems have been developed and evaluated specifically for hot-stamping applications as reviewed by Fan et al. [16]. The main required properties for a coating, developed specifically for hot stamping, include oxidation resistance at high temperatures, good formability at room and high temperatures, good corrosion resistance, providing barrier and cathodic protection mechanisms to the steel substrate, painting adhesion and weldability [16,24]. Among the metallic coating systems, Al and Zn-based coatings have been the most evaluated. These systems are known for forming thermodynamically stable oxides which play a role of a barrier protection [19]. However, Zn-based coatings are much more sensitive to the variations of hot-stamping process parameters. Additionally, the high susceptibility to liquid-metal induced embrittlement is one of the main drawbacks related to the zinc systems for direct hot stamping [12,21]. Nevertheless, other coating systems have been under investigation for hot-stamping applications, e.g., zinc-nickel and hybrid coatings. Table 2.2 summarises the advantages and challenges of different coating systems for hot-stamping applications based on the review done by Fan et al. [16]. However, the hot-dip aluminium-silicon (Al-Si) with a near eutectic composition (7 % to 12 % Si in mass fraction) has been the most applied system for hot stamping [6–8,19].

**Table 2.2 - Advantages and challenges related to alternative coatings systems for hot-stamping applications**

System	Advantages	Challenges
Aluminium-silicon (Al-Si)	Oxidation resistance Barrier protection No need for phosphating	Coating brittleness Liquid Al adhesion No cathodic protection
Galvanised (GI)	Cathodic protection	Liquid metal induced embrittlement Liquid Zn adhesion Oxide scale Coating brittleness
Galvannead (GA)	Cathodic protection No liquid metal induced embrittlement	Coating brittleness
Zinc-nickel (Zn-Ni)	High melting temperature Cathodic protection No liquid metal induced embrittlement	Nickel cost
Hybrid organic-inorganic matrix (Mg, Ti, Al)	Cathodic protection	Brittle Fe-Al intermetallics; Melting of Al and Mg; High cost

Source: Adapted from Fan et al. [16]

#### 2.4.1 Hot-dip aluminium-silicon

Type 1 hot-dip aluminised (HDA) consists of an aluminium-silicon alloy near to the eutectic composition (7 % to 12 % Si in mass fraction). It has been applied in several industrial sectors due to its high corrosion and thermal resistance, such as: manufacturing exhaust systems, heat shields, heating boilers and cookers [16]. Al-Si is also the most widespread coating system applied to PHS prior the thermo-mechanical process [6,12,16,19,24,49].

The hot-dip Al-Si has been extensively investigated in terms of structure-morphology and corrosion properties (not for hot-stamping applications) [31,33,50,51]. The coating consists of different sublayers: the aluminium coating matrix and the interdiffusion layers. The aluminium matrix, also known as free layer (FL), is thicker than the interdiffusion layer and contains cathodic Al-Fe-Si precipitates. The interdiffusion part of the coating is composed of an upper and a lower interdiffusion layer (UIDL and LIDL, respectively). The LIDL is known as a hard and brittle Al-Fe intermetallic phase, often reported as  $\eta$  -  $\text{Fe}_2\text{Al}_5$ , adjacent to the steel substrate. The silicon addition suppresses the growth of the LIDL and promotes a smoother interface between the steel and the coating. The UIDL is characterised as a mixture of  $\theta$ - $\text{Fe}_4\text{Al}_{13}$  and  $\tau_5$ - $\text{Fe}_2\text{Al}_7\text{Si}$  intermetallics, more ductile than the LIDL ( $\eta$ -  $\text{Fe}_2\text{Al}_5$ ) [31,50,51].

#### 2.4.1.1 Formation and growth of intermetallic phases on hot-dip Al-Si

The coating morphology as well as its properties are related to the hot-dipping process parameters, mostly to the chemical composition of the molten bath, dipping temperature and time [32]. The steel substrate has also an influence on the final coating morphology [32,51,52]. During hot dipping, diffusion takes place between the chemical elements which comprise the molten bath and the steel substrate [52]. Consequently, intermetallic phases are formed. Cheng et al. [52] have shown that the pure aluminium coating comprises a thick intermetallic layer of  $\eta$  -  $\text{Fe}_2\text{Al}_5$  at the interface with the steel substrate and a thin layer of  $\theta$ - $\text{Fe}_4\text{Al}_{13}$  at its top. The intermetallic phases are brittle, mainly the  $\eta$ - $\text{Fe}_2\text{Al}_5$ , and they grow in an irregular manner, presenting a finger-like morphology [52]. Consequently, they are detrimental for several properties, such as corrosion and mechanical strength, as they play a role of cracking initiation. Therefore, the main challenge is to decrease the thickness of the intermetallic phase promoting a smoother interface and enhancing the formation of more ductile phases.

Cheng et al. [51] and Yin et al. [53] have investigated the influence of silicon in the aluminium molten bath on the growth of the intermetallic phases. The authors have shown that the higher the silicon content, the smoother the interface at the steel substrate and the thinner the intermetallic phase. Cheng et al. [52] found out that  $\eta$ - $\text{Fe}_2\text{Al}_5$  phase grows preferentially along the [001] direction, due to its crystalline defects. Hence, silicon occupies the vacancies in the lattice suppressing the growth of  $\eta$  -  $\text{Fe}_2\text{Al}_5$  [51,53]. Lemmens et al. [54] have shown that the silicon enrichment at the grain boundaries of the  $\eta$  -  $\text{Fe}_2\text{Al}_5$  phase could also hinder its growth.

The silicon addition also promotes the formation of ternary Fe-Al-Si intermetallics [33,51,53]. Lemmens [49] have highlighted the difficulty in determining these ternary intermetallics due to their very similar chemical composition. Consequently, different studies have been done in order to characterise the intermetallic phases in the Fe-Al-Si system [37,49,51,53,55–58]. Nevertheless, contradictory results related to the stoichiometry of the intermetallics in the Al-Fe-Si system can be often found in the literature. Thus, Lemmens [49] has suggested the use of high resolution diffraction methods to characterise them.

#### 2.4.1.2 Corrosion mechanism of hot-dip Al-Si

The protection mechanism afforded by Al-Si coatings is substantially influenced by the environmental conditions. Panossian et al. [25] have investigated whether flame spraying Al and hot-dip Al-Si (13 % Si in mass fraction) could provide cathodic protection to the steel substrate against atmospheric corrosion. They have found out that only in atmospheres with high chloride concentrations the Al and the Al-Si coatings ensure cathodic protection to the steel substrate, since the coatings lost their passive properties because of chloride ions. On the other hand, in chloride free atmospheres or very small ion concentrations, the Al and Al-Si coatings keep their passive properties due to the oxide layer, which is formed on the metal surface. In the passive state, Al and Al-Si coatings did not provide cathodic protection to steel substrate [25]. In this case the coating layer is nobler than the steel substrate and the protection mechanism is by barrier protection [7].

De Graeve et al. [31] evaluated the influence of silicon content using a depth profile approach combined with electrochemical micro cell. This methodology enables the characterisation of each sublayer composing the coating. The authors have shown, considering the corrosion potential ( $E^*$ ), that the free layer (FL) would corrode preferentially compared to the steel substrate and the interdiffusion layer (IDL), but the steel would be protected mainly by barrier mechanism provided by the IDL (as the IDL had higher  $E^*$  than the interstitial free steel). Additionally, they were able to investigate the electrochemical behaviour of the lower interdiffusion layer (LIDL), which presented the noblest value of  $E^*$ . Lemmens et al. [50] investigated the addition of 1 % of silicon (in mass fraction) in HDA steels using glow discharge optical emission spectroscopy (GDOES) combined with scanning vibration electrode technique (SVET). The methodology employed provided insights about the current distribution of the different coating sublayers in  $0.05 \text{ mol}\cdot\text{L}^{-1} \text{ NaCl}$ . In general, the authors pointed out that the FL presented a very low activity when silicon is not added in the aluminium molten bath. However, the silicon addition promoted irregular anodic current distribution in the FL, which was attributed to the presence of precipitates. Conversely, cathodic currents were measured for the upper interdiffusion layer (UIDL), LIDL and the steel substrate. The highest cathodic current was measured in the LIDL. These findings were in agreement with the work by Vu et al. [59], whom analysed the sacrificial behaviour in cut-edge steel coated with Al-Si exposed in chloride media by means of *in situ* current and pH measurements. The authors have shown that in chloride media the corrosion

of the coating starts locally, which results in both local activation and depassivation of the coating. Consequently, the coating behaves sacrificially versus the steel [59].

## 2.5 Press-hardened steel coated with hot-dip Al-Si

The complex structure of such Al-Si coatings changes completely due to the hot-stamping process. The coating morphology becomes much more complex because of the iron diffusion into the coating. The sublayers formed are enriched in either aluminium or iron [8,19,47]. The silicon, seen as precipitates in the initial condition, is present in the press-hardened condition in solid solution [8,19]. Furthermore, silicon plays an important role hindering the growth of the brittle aluminium-rich layers. The aluminium-rich sublayers show low fracture toughness and hardness of 900 HV<sub>0.05</sub> to 1150 HV<sub>0.05</sub> whereas the iron-rich sublayers have been reported to present high fracture toughness and hardness of 300 HV<sub>0.05</sub> to 600 HV<sub>0.05</sub> [8]. Windmann et al. [8] have shown that the volume fraction of the iron-rich phases increases (AlFe) while that of the aluminium-rich phases (Al<sub>5</sub>Fe<sub>2</sub>) decreases when longer soaking time at high austenitisation temperatures are set during hot stamping. After the hot stamping, the interface between the coating and the steel substrate consists of a single interdiffusion layer (IDL) enriched in iron and little amount of aluminium and silicon. The presence of voids, often seen in the IDL, is a consequence of the fast diffusion; their volume ratio increases with time and temperature [24]. The presence of voids in the IDL promotes the initiation of cracks, being detrimental to the general coating properties [8,35,60].

The corrosion resistance of coated PHS is still a subject of investigation. The corrosion resistance of PHS coated with Al-Si has been evaluated mostly by means of standard corrosion tests, such as electrochemical measurements and accelerated corrosion tests [7,11]. By means of cyclic corrosion tests, Dosdat et al. [11] compared the corrosion resistance of different metallic coating systems for hot-stamping applications. The cosmetic, the cut-edge and the perforation corrosion resistance of the Al-Si system was compared with that of Zn-based coatings (galvanised and galvanized). The results pointed out the Al-Si coating as the most suitable system for hot-stamping applications because, as already mentioned, Zn-based coatings are much more sensitive to the hot-stamping process parameters. Additionally, the high susceptibility to liquid metal embrittlement is one of the drawbacks related to the Zn-based systems for hot stamping [12,21].

Allély et al. [7] evaluated the corrosion resistance of PHS coated with Al-Si. According to the authors, although the coating does not provide cathodic protection to the steel substrate, due to the small potential difference between the steel substrate and the coating layer, it is a suitable coating system for hot stamping. The authors also characterised the corrosion products of PHS coated with Al-Si after accelerated tests, either cyclic or continuous. They showed that the nature of the corrosion products is influenced by the pH variations. In the cyclic accelerated tests, the pH varies and promotes the formation of hydroxides and aluminosilicates. In the continuous salt spray, the pH variation is very limited and the corrosion products have a predominant amorphous characteristic and were a mixture of aluminium, silicon and iron oxides [7].

## CHAPTER 3 - Materials and methods

### 3.1 Materials and samples' preparation

Industrial blanks of 22MnB5 steel, 1.4 mm thick, coated with hot-dip Al-Si (10 % Si in mass fraction) were received from a steelmaker for this study. These samples were designated in this work as **AR** (as-received). On the other hand, the **PHS** samples (press-hardened steel), coated with Al-10 % Si in mass fraction (prior hot stamping), were cut from a door beam structural component, produced on industrial scale. This component was provided for this research by a carmaker; therefore, the hot-stamping conditions were not provided. Table 3.1 shows the nominal chemical composition of the 22MnB5 bare steel in terms of maximum % in mass fraction, according to the steelmaker specifications [61].

**Table 3.1 - Nominal chemical composition of 22MnB5 steel in terms of maximum % in mass fraction**

Grade	C	Si	Mn	P	S	Al	B	Ti + Nb	Cr + Mo
22MnB5	0.25	0.4	1.4	0.03	0.01	0.1	0.005	0.12	1

Source: ArcelorMittal [61]

According to the specifications [62], the coating applied to the AR samples was the AS150, which has a thickness of 25  $\mu\text{m}$  per side and a mass of 150  $\text{g}\cdot\text{m}^{-2}$  double-sided. On the other hand, the PHS samples were prior coated with the AS80 coating. This coating has thickness of 14  $\mu\text{m}$  per side and mass of 80  $\text{g}\cdot\text{m}^{-2}$  double-sided.

Some AR samples were submitted to a hot-stamping process on laboratory scale. The samples were heated at different austenitisation temperatures (850 °C, 900 °C and 950 °C) for 8 min. The transfer time from the furnace to the press tool was lower than 7 s. The stamping tool was composed of a cooling system by water ducts with flow rate of 13  $\text{L}\cdot\text{min}^{-1}$  and the ducts temperatures were maintained at 5 °C. The press tool had a clamping force of 79 t and a contact pressure was maintained at 70 MPa. There was no mechanical deformation of the specimens. There was only compressive strain, as they were kept flat. All samples' conditions used in this work are summarised in Table 3.2.

As a standard sample preparation method, the specimens were cut into small samples suitable for characterisation and electrochemical analyses. A cut-off machine with cooling system was used to cut the samples in small dimensions. After that, the samples were cleaned in isopropanol and dried by a cold stream of air. The samples' cross section were prepared following the standard metallographic methods: hot mounted in Bakelite, ground with silicon carbide papers and polished with colloidal silica suspension as the final step.

**Table 3.2 - Samples' identification and their corresponding conditions**

Sample ID	Condition
Bare steel	22MnB5 steel grade uncoated
AR	22MnB5 coated with hot-dip Al-Si (Si 10 % in mass fraction)
PHS850	AR condition heated at 850 °C for 8 min and hot stamped
PHS900	AR condition heated at 900 °C for 8 min and hot stamped
PHS950	AR condition heated at 950 °C for 8 min and hot stamped
PHS	Press-hardened door beam produced on industrial large scale

Source: Author

### 3.2 Methods

Complementary techniques were used to link the structure composition of the layered coating systems (either before or after hot stamping) with the global and local corrosion properties.

The morphology-composition of the layered structure was obtained using field emission-scanning electron microscopy (FE-SEM) combined with energy dispersive X-ray spectroscopy (EDS), glow discharge optical emission spectroscopy (GDOES), Raman spectroscopy and synchrotron X-ray diffraction (XRD).

Global and local corrosion properties were obtained using different techniques as listed hereunder:

- Global electrochemical tests: open circuit potential (*OCP*) and linear sweep voltammetry (*LSV*).
- Accelerated corrosion tests: continuous salt spray test (*SST*)
- Local electrochemical techniques: scanning Kelvin probe force microscopy (*SKPFM*) and electrochemical micro cell.

Background of the methods used is summarised in this chapter. However, the specific operational conditions were added in the chapters where the results were given (Part II).

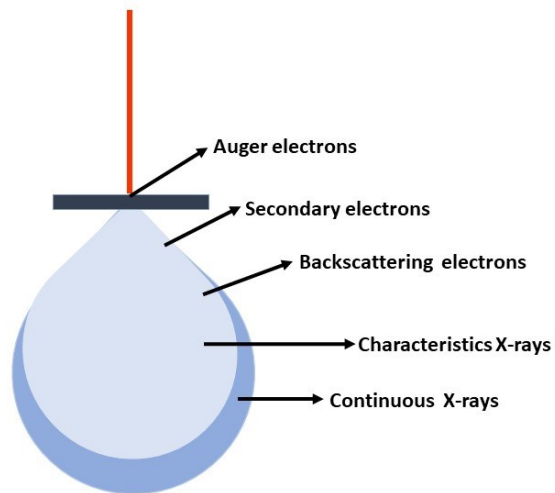
### 3.2.1 Morphological and compositional analyses

#### 3.2.1.1 Field emission-scanning electron microscopy (FE-SEM) combined with energy dispersive X-ray spectroscopy (EDS)

Scanning electron microscopy is a widely used technique applied for morphological observations in different research fields [63]. Moreover, it provides high resolution and high magnification images up to 10 nm level [63]. Conventionally, a vacuum of  $10^{-10}$  torr is used in most FE-SEM where metals are investigated [63].

The principle is based on the interaction between the electron beam (primary electron) and the sample. The main electron sources are the tungsten wire filament, the lanthanum hexaboride ( $\text{LaB}_6$ ) and the field emission electron guns (FE). The choice of the electron gun has an influence on the brightness, on the energy spread and on the source size [63]. Different interactions may take place between the primary electron and the sample, as illustrated in Figure 3.1. They consist of either elastic or inelastic electrons' scatterings which are detected either for image formation or chemical microanalyses. The actual volume which the electron beam interacts with in the sample is known as interaction volume. This is related to the acceleration voltage and sample's characteristics, mainly the atomic number ( $Z$ ). Higher acceleration voltage and lower  $Z$  enhances the interaction volume [63,64].

**Figure 3.1 -Schematic representation of the interaction of a primary beam and the different responses which can be obtained as function of the volume interaction**



Source: Author

Images are formed by the detection of either secondary electrons (SE) or backscattered electrons (BSE) [63]. The SE results from the inelastic scattering and provides topographical images. Usually, secondary electrons with low escape depth are used for contrast imaging to provide information about the morphology/topography. The elastic scattering results in BSE, which indicate differences on elemental compositions by means of the image contrast. Heavier elements show brighter contrast than lighter elements due to a difference in yield [63].

The inelastic scattering also results in the generation of the characteristic X rays; their detection enables the characterisation of the elemental composition of the sample [63]. Both energy-dispersive X-ray spectrometer (EDS) and wavelength-dispersive spectrometer (WDS) are detectors used to carry out compositional micro-analyses. The EDS is mostly used as it allows faster data acquisition than the WDS. On the other hand, the WDS analysis is usually done when a precise detection of one element is required. The limit of detection of WDS is 10 ppm to 100 ppm, whereas for EDS it is 1000 ppm to 3000 ppm. Scanning of the primary electron beam facilitates the mapping of individual elements as function of the morphology present in the sample [63].

### 3.2.1.2 Glow discharge optical emission spectroscopy (GDOES)

GDOES provides an elemental profile as function of depth. The sample is placed close to the anode (usually a copper tube) within argon. A potential difference is applied between the sample (cathode) and the anode, which promotes the formation of a plasma of argon ions. Through a plasma discharge, the sample is cathodic sputtered from the surface. The removed atoms are excited by the collisions with argon ions. When the excited atoms return to their ground state, they emit photons with characteristic wavelength for each element. A holographic diffraction grating separates and focuses the wavelengths [49,55,65].

In addition to its advantages as a characterisation technique, such as fast acquisition data, GDOES has been used as a sample preparation tool for local electrochemical techniques as function of depth profile [31,50,66–68]. In this investigation, GDOES was also used as sample preparation tool for electrochemical depth-profile analyses as shown further in Chapter 6.

### 3.2.1.3 Raman spectroscopy

Raman spectroscopy enables the characterisation of both organic and inorganic compounds [69]. The principle of the technique is based on the vibrational frequency shift (in wavelength) of the inelastic scattering resulting from the interaction between an electromagnetic radiation and the molecules [70,71]. Each molecule has its own vibrational frequency, for this reason the Raman spectra can be considered as a “fingerprint” for each compound [71]. Raman imaging spectroscopy consists of coupling a spectrometer to a microscope, which enables a precise selection of the area in the sample to be analysed. Moreover, line-scanning and mappings analyses can also be carried out [69].

### 3.2.1.4 Synchrotron X-ray diffraction

Synchrotron radiation or synchrotron light is an electromagnetic radiation which is emitted when electrons from an electron gun are injected throughout the linac to the booster ring. Then the storage ring, where electrons are moving at the speed close to the light, changes their direction due to the magnetic field. The radiation diverges from the storage ring and goes into the beamlines, usually tangential to the storage ring. At the beamlines, the radiation is refined by means of monochromators and mirrors; then a specific wavelength in a range from infrared to highest X-ray energy can be chosen [72,73].

Each synchrotron facility has a different number of beamlines and techniques available. However, some of them are common in most of light source facilities, for example the X-ray diffraction (XRD). The XRD is an important tool to characterise crystalline materials; and the biggest advantage to combine this technique with synchrotron is the possibility to select the most adequate wavelength for each experiment as well as the possibility of collimating the beam.

As the crystal structure is composed of atoms regularly spaced from each other by an interatomic distance, forming several planes of atoms with an interplanar distance  $d$  (with the same  $hkl$  Miller indices), the phenomenon of diffraction is possible [74]. The Bragg’s Law, seen in Equation (3.1), shows the conditions for diffraction:

$$n\lambda = 2d_{hkl} \sin \theta \quad (3.1)$$

where  $n$  is the order of reflection (an integer number),  $\lambda$  is the wavelength of an incident beam (monochromatic and in-phase),  $\theta$  is the incidence angle on the interatomic planes.

These planes are separated by a distance  $d$ . The planes shall present the same  $hkl$  Miller indices [74].

The diffraction angle can be determined by means of a diffractometer. It is an equipment which consists basically of an X-ray source and a detector (counter). The sample condition influences greatly the results. The more randomly orientated the material to be analysed, the more diffracted angles detected [74]. This is the opposite case of sheet steel plates as they show a preferential orientation (texture) which may hide some angles that could be diffracted [74].

### 3.2.2 Global electrochemical techniques

Within corrosion studies, it is important to evaluate both the thermodynamic and kinetics of cathodic and anodic reactions, which take place locally at the interface of a metal electrode (metal/ electrolyte interphase). The immersion of a metal in an electrolyte leads to the formation of an electrical double layer [75,76] and the so called electrode potential is measured at this interface (with respect to a reference electrode) [29,75,76].

#### 3.2.2.1 Open circuit potential

If for instance, the electrode potential is measured and there is no connection with an external circuit, it is named as open circuit potential (*OCP*). The variation of *OCP* within time indicates that the anodic and cathodic reactions are different. If one of these reactions is the oxidation of a metal, the *OCP* is also the corrosion potential ( $E^*$ ) [75]. Therefore, the *OCP* measurement is one of the main techniques used for corrosion studies. The evaluation of *OCP* within time enables the correlation with different phenomena in the system which is relevant in this research context. Some examples of what can be correlated with the *OCP* evolution are:

- dissolution of an oxide layer due to the drop of the potential;
- formation and repassivation of metastable pits in passive materials as a consequence of small potential variation;
- ennoblement of the system by shifting the potential towards nobler values;
- equilibrium at the steady-state due to *OCP* stabilisation.

### 3.2.2.2 Polarisation curves

If an external voltage (overpotential) is applied to the system, it will cause a variation on the electrode potential, resulting in its polarisation. The overpotential may be applied either in favour of the cathodic reactions or enhancing the anodic reactions. The polarisation curves can be acquired experimentally and they enable the analysis of the electrochemical kinetics, allowing, therefore, the analysis of the electrochemical reaction rates and in some cases mass transport [75]. Electrochemical reaction rates are usually obtained by the Tafel extrapolation method, where the linear branch of the anodic and cathodic reactions is extrapolated. The intersection of these two curves represents the corrosion potential and the corrosion current (most associated with the corrosion rate) [75]. However, this method is only valid when the polarisation curves present the linear branch related to the activation polarisation [29].

Linear sweep voltammetry (LSV) can be considered as one of the most used techniques to acquire experimentally the polarisation curves and then evaluating the electrode processes. The principle consists of a continuous time-varying potential to the working electrode and the measurement of the current density. The technique is often used at stationary electrodes but it can also be used at hydrodynamic electrodes [75]. The sweep influences on the results. Usually, it is slow enough to guarantee at least the quasi steady-state conditions at the electrode surface. For example, reversible reactions characterised at slow sweep rates may be presented as quasi-reversible at high sweep rates [55,75].

In this research, the investigation was focused on the anodic branch of the polarisation curves. This enables the evaluation of some aspects of the system such as:

- passive or active behaviour in a specific medium;
- breakdown of the passive layer and the correlation with precipitates in the system;
- current density and the influence of an oxide layer and intermetallic phases on the electrochemical behaviour.

### 3.2.3 Accelerated corrosion test

Continuous salt spray test has been used since 1914 and it became a standard test in 1939 by ASTM (B 117 method) [77]. Despite its large applications, mainly in the industry, there is an agreement that the continuous accelerated tests do not represent the actual material performance as the weathering tests, which are the most accurate way to determine corrosion rate/resistance [78]. The main drawback of the continuous accelerated tests is related to the

uninterrupted exposure to a wet stage in a high chloride medium [77–80]. However, the biggest advantage of the accelerated tests in comparison with a field-test is the fast access to the corrosive process; whereas an outdoor exposure requires at least two years, the accelerated tests just demand few cycles [78]. In order to improve the performance of the continuous salt spray, they have been replaced by the cyclic accelerated tests. These tests consist of wet and dry cycles similar to weathering tests [77–79]. Nonetheless, the continuous salt spray test has still been used mainly as quality control [77]. In addition to this, the accelerated tests provide insights about the nature of the corrosion products formed under severe environments, e.g. high chloride media [7,11].

### 3.2.4 Local electrochemical techniques

Local electrochemical techniques are based on either scanning or small-area electrode methods [81–83]. They allow for corrosion studies to have information about the location and roles of anodes and cathodes in the overall corrosion mechanism. In this thesis, one technique from each principle was used. The scanning Kelvin probe force microscopy (SKPFM) was chosen because it presents a higher lateral resolution compared with other scanning techniques. The lateral resolution is lower than 100 nm and the potential sensitivity is lower than 1 mV [84]. However, the measurements of the Volta potential by SKPFM are carried out at ambient conditions (without an electrolyte). On the other hand, the electrochemical micro-cell technique enables the isolation of a small area in the sample. This ensures a precise investigation of the electrochemical process locally. Conversely to the scanning techniques, small-area electrode methods enable standard electrochemical measurements and the direct measurement of the current density. Moreover, the current resolution is greatly improved reaching a range from pA to fA. This allows the investigation of corrosion process in a nanometre scale [81,83].

#### 3.2.4.1 Scanning Kelvin probe force microscopy

The SKPFM technique enables the concomitant analysis of the surface topography, in a nanometre scale, and the mapping of the Volta-potential difference (contact-potential difference (CPD)) of a conductive plate with respect to a reference, i.e., between the sample and the AFM tip [55,84,85]. When they are electrically connected an electron flow occurs, in order to establish an electrochemical potential equilibrium among them [84,86,87]. Therefore, when their Fermi levels ( $E_F$ ) are the same. The electron flow is related to the work

function, a characteristic for each material and highly sensitive to slight changes on the material surface as well as in the structural levels [88–90]. The work function is defined as the minimum energy required to remove an electron from the bulk structure (Fermi level) to a position just outside the surface (vacuum level ( $E_{vac}$ )) [85–87,90]. Thus, the electrons flow from the material which presents the highest work function to the material which has the lowest one [55,87], resulting in a work function difference which is directly related to the Volta-potential difference, measured by SKPFM. Thus, if the work function of the reference (tip) is known, it is possible to obtain the work function of the sample, according to Equation (3.2) as follows [91]:

$$\Delta\psi = \frac{\phi_2 - \phi_1}{e} \quad (3.2)$$

where  $\Delta\Psi$  is the Volta-potential difference,  $\Phi$  is the work function of the sample ( $\Phi_2$ ) and of the tip ( $\Phi_1$ ), and  $e$  is the electron charge ( $-1.6 \times 10^{-19}$  C).

However, there is a slight difference between the definition of work function and the Volta potential; the latter is related to the minimum energy required to bring a charge from the infinity ( $E_\infty$ ) to the vacuum level [86,87,92].

The AFM tip and the sample form a capacitor. An AC voltage is applied to the tip promoting its oscillation and a DC voltage is applied in order to nullify the current flow between the tip and the sample. Consequently, the DC voltage applied is equal to the Volta-potential difference between the tip and the sample [85,86,92,93]. As the tip is biased during the measurements, the potential signal recorded is mathematically inverted (multiplied by - 1) in order to reflect the true relation of the Volta-potential values and the surface under investigation [31,90,94,95].

Once the signal inversion is done, the Volta potential maps will be in accordance with the electrochemical nobility of the metals (galvanic series). For instance, high potentials will indicate cathodic areas, whereas low potentials will represent more anodic areas [87]. Indeed, a linear relationship between Volta potential and corrosion potential was demonstrated [92]. For this reason, the technique has been widely used to access the electrochemical behaviour of different alloys in local scale [94–99].

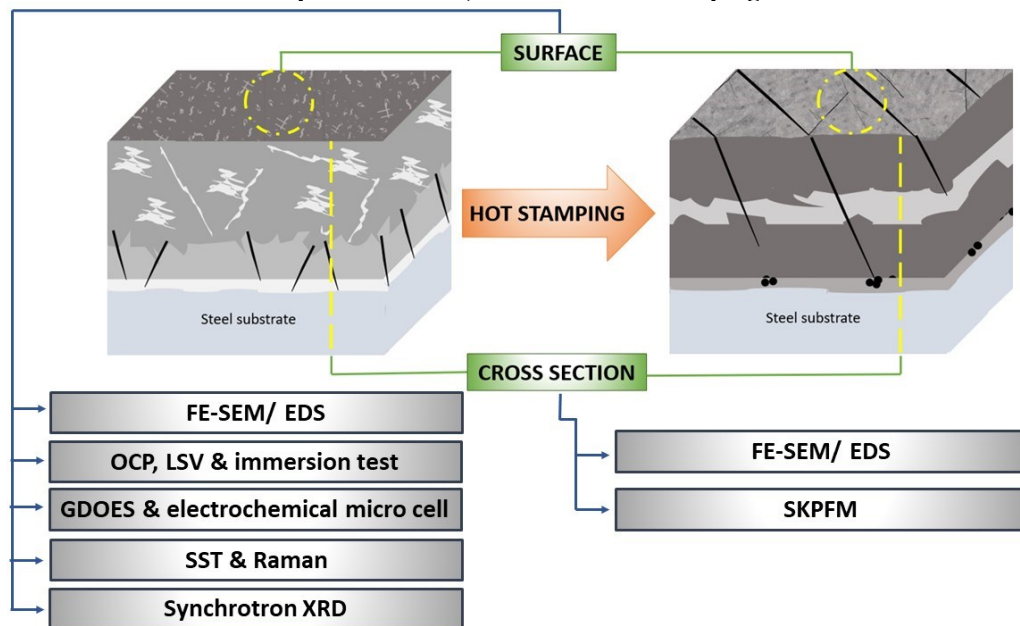
### 3.2.4.2 Electrochemical micro cell

This technique is based on the principle of decreasing the area to be analysed in a range of micrometres and still carrying out the standard electrochemical measurements [66,68,81,82,100]. The use of the electrochemical micro cell was first introduced by Suter et al. [83]. The micro cell consists of a capillary glass (filled with an electrolyte) and counter electrode connected with the reference electrode. The micro cell is fixed in the place of one of the objectives lens of an optical microscope. [81–84]. The capillary glass is used to position a droplet of electrolyte in the sample's surface based on two different techniques: free droplet or silicone rubber gasket. The former depends on the surface tension of the electrolyte to hold the droplet in the position to guarantee the capillary at position above 10  $\mu\text{m}$  of the sample surface. Conversely, when a silicone rubber gasket is placed at the mouth of the capillary, it confines the electrolyte in a small area [81–84].

### 3.3 Overview

In the schematic drawing, Figure 3.2, it is shown how the structural and compositional analysis of the coating/steel was combined with different local electrochemical methods.

**Figure 3.2- General schematic experimental approach used to characterise either the surface or cross section of the different sample conditions (AR - before hot stamping and PHS - after hot stamping)**



Source: Author

## **Part II**

### Results and discussion

## CHAPTER 4 - The effect of hot stamping on Al-Si coating morphology<sup>2</sup>

### 4.1 Introduction

The hot-stamping conditions promote the diffusion of the chemical elements which comprise the system (coating/steel) [6,8,14,19,24]. This chapter provides a general characterisation of the Al-Si coating (10 % Si in mass fraction) before and after hot stamping. Moreover, a clear view about the changes in the coating morphology and composition, due to hot stamping, is of paramount importance to support the discussion of the next chapters in which the electrochemical behaviour will be correlated.

### 4.2 Experimental procedure

The AR and PHS samples were prepared according to standard metallographic procedures: hot mounted in Bakelite, ground and polished. The cross-section images of the AR (a) and PHS (b) samples after the metallographic procedures are shown in Figure 4.1. The samples were characterised by means of FE-SEM; the microscope was set to operate with 15 kV acceleration voltage, 12 pA probe current and a working distance of approximately 10 mm. The semi-quantitative elemental analyses were undertaken by means of energy dispersive X-ray spectroscopy (EDS). The EDS analyses were performed in two different ways: local identification (point ID) and elemental mappings. The EDS results from the point ID method, may indicate some uncertain elements in the sample composition due to their low concentration in the analysed area. These elements were presented by the red colour.

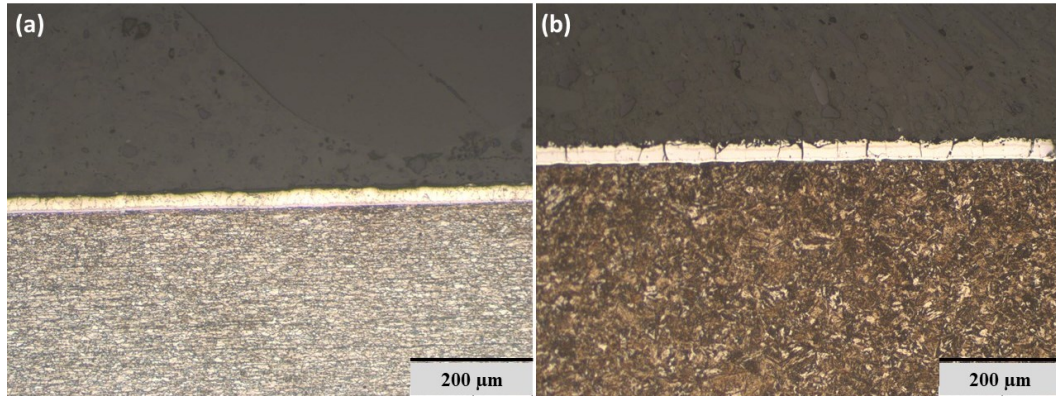
---

<sup>2</sup> This chapter is partially based on:

COUTO, C. P.; REVILLA, R. I.; COLOSIO, M. A.; COSTA, I.; PANOSSIAN, Z.; DE GRAEVE, I.; TERRYN, H.; ROSSI, J. L. Electrochemical behaviour of 22MnB5 steel coated with hot-dip Al-Si before and after hot-stamping process investigated by means of scanning Kelvin probe microscopy. *Corrosion Science*, v. 174, n. June, p. 108811, set. 2020. <https://doi.org/10.1016/j.corsci.2020.108811>.

COUTO, C. P.; ANDREATTA, F.; LANZUTTI, A.; COSTA, I.; PANOSSIAN, Z.; DE GRAEVE, I.; TERRYN, H.; ROSSI, J. L.; REVILLA, R. I. Depth profiling approach to evaluate the influence of hot stamping on the local electrochemical behaviour and galvanic series of hot-dip Al-Si coating on 22MnB5 steel. *Corrosion Science*, 2021. <https://doi.org/10.1016/j.corsci.2021.109435>.

**Figure 4.1 - Optical microscopic images showing the conditions of the coating layer of (a) AR and (b) PHS, just after the metallographic procedures**



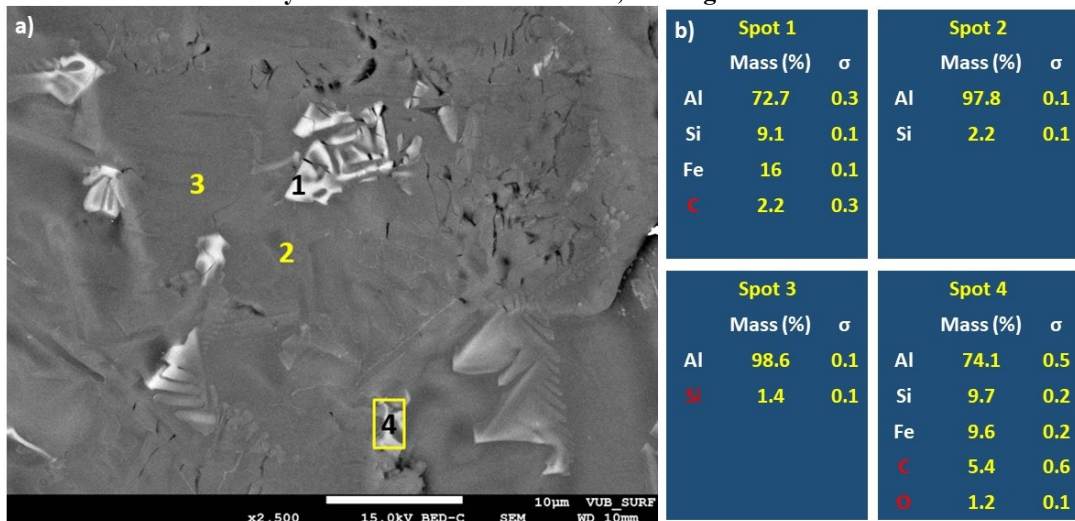
Source: Author

### 4.3 Results

#### 4.3.1 Surface characterisation

The surface morphology of AR condition, as well as its semi-quantitative elemental analysis is shown in Figure 4.2. The coating surface consists of a matrix with some precipitates distributed in it. The EDS results, Figure 4.2 (b), shows that the coating matrix is mostly composed of aluminium (spots 2 and 3). On the other hand, the precipitates are ternary intermetallic composed of Al-Si-Fe, as presented in Figure 4.2 (b) (spots 1 and 4).

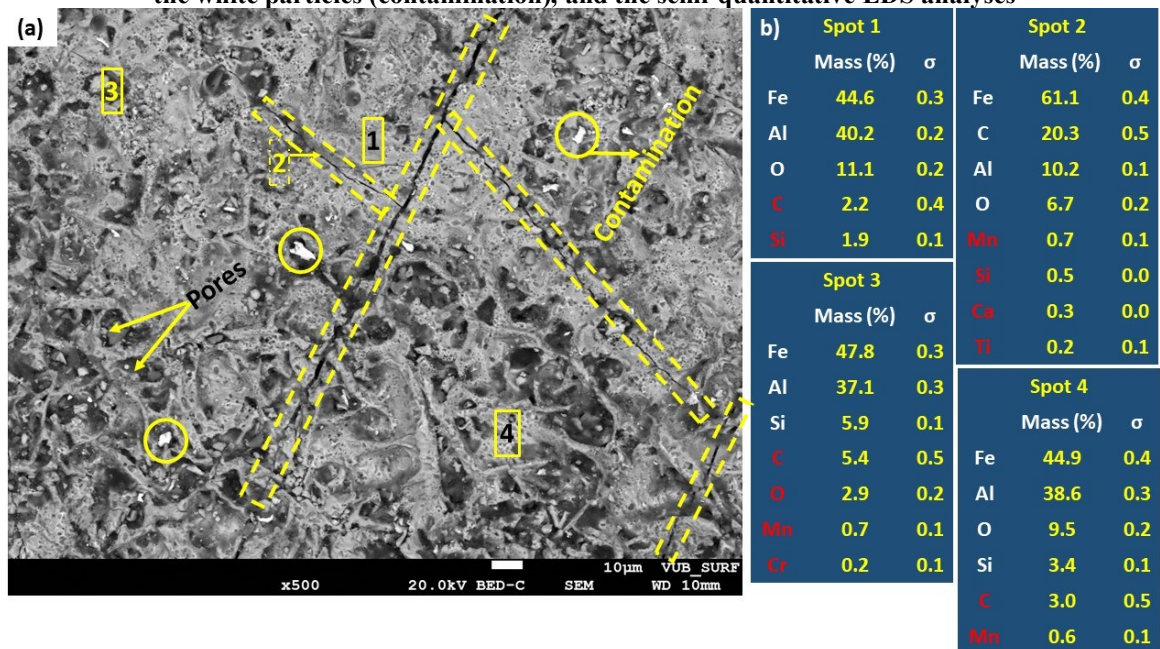
**Figure 4.2 - Scanning backscattered electron image showing the surface morphology of 22MnB5 steel coated with Al-Si (10 % Si in mass fraction) composed of precipitates, and semi-quantitative EDS analyses of the whole are scanned, and regions 1 and 2**



Source: Author

The Al-Si coating's surface morphology after hot stamping is presented in Figure 4.3. The first highlight is concerning the presence of cracks at the surface (dashed yellow lines). In addition to this, the surface is rough, and it contains pores (darker areas). Moreover, intermetallics are no longer seen at the surface. The white particles are contamination; the EDS analysis (not shown) indicates a mixture of different elements. It is important to point out here that these samples are industrial based. Therefore, small contaminations are often presented.

**Figure 4.3 - Scanning backscattered electron image showing the surface morphology of press-hardened 22MnB5 steel coated with Al-Si (10 % Si in mass fraction), highlighting the cracks (dashed lines) and the white particles (contamination), and the semi-quantitative EDS analyses**



Source: Author

As seen in the results shown in Figure 4.3, the surface becomes enriched in iron after hot stamping. The spot 1 shown in Figure 4.3 (b) can be considered as the coating matrix (light grey areas) which comprises mostly iron and aluminium. However, the iron content is higher than the aluminium one. Moreover, a little amount of silicon is also identified in the coating matrix indicating the formation of solid solution in the Fe-Al phase. Additionally, the presence of a high oxygen content suggests the formation of an oxide layer composed of a mixture of iron, aluminium and silicon oxides. The hot-stamping conditions enhance the iron diffusion from the steel substrate into the coating layer, while aluminium

diffuses towards the steel substrate. The silicon diffusion to the surface has already been discussed by Windmann et al. [8].

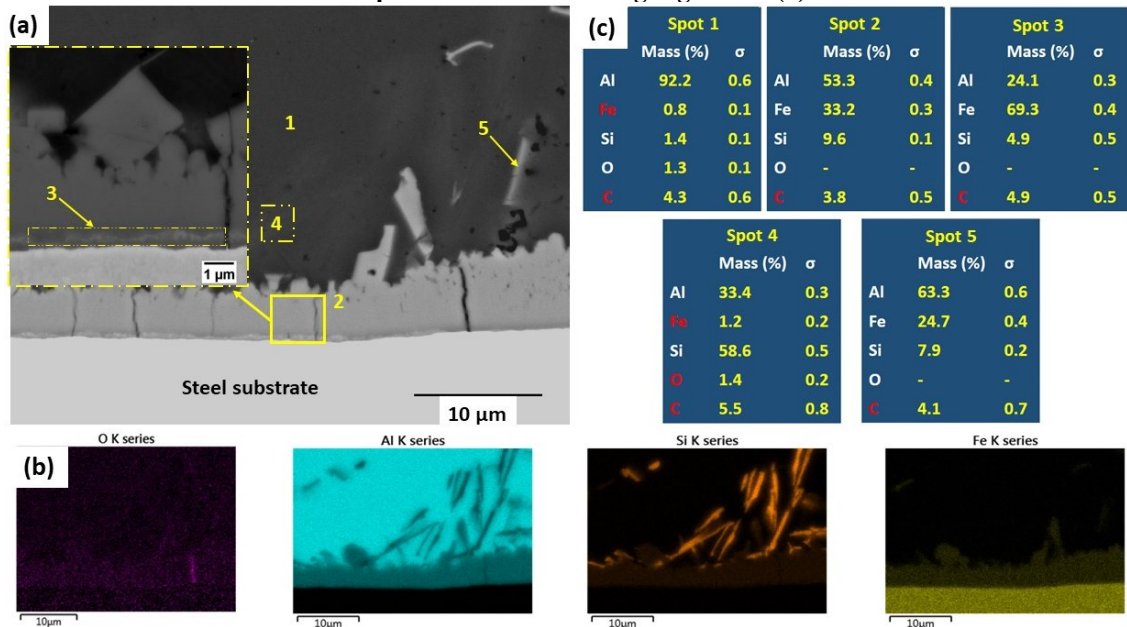
#### 4.3.2 Cross-section characterisation

The cross-section morphology of the AR sample and the EDS analyses are shown in Figure 4.4. The coating comprises of two main layers (1 and 2) and a thin and discontinuous layer adjacent to the steel substrate (3). The first layer is often called the outer layer or free aluminium layer (FL) due to the high amount of aluminium present Figure 4.4 (c) - spot 1) [31,50]. In addition, two different precipitates are seen in this first outer layer. According to the EDS mappings in Figure 4.4 (b), the precipitates consist of either Si or Fe-Al-Si. On the other hand, the spot 4 in Figure 4.5 (c) suggests the formation of Al-Si precipitates. However, the aluminium content in this spot is mostly related to its presence in the matrix which influences the punctual EDS analyses due to the interaction volume. Thus, the EDS mapping in Figure 4.4 (b) is related to the eutectic Si [49]. The second layer is known as an interdiffusion layer (IDL); the amount of iron increases in this layer due to the chemical diffusion which takes place during the hot-dipping process [31,33,50,51]. Moreover, the amount of silicon in the IDL is also near to the molten bath chemical composition (Figure 4.4 (c) - spot 2). Nevertheless, it has been reported that the IDL in hot-dip aluminised steels is actually composed of two sublayers: the upper and the lower interdiffusion layer (UIDL and LIDL, respectively) [31,33,50]. This is clearly seen in the inset image in Figure 4.4 (a), highlighting the layer 2 in which the two sublayers are present. The LIDL is characterised as the discontinuous thin layer (3) adjacent to the steel substrate; it comprises higher iron and lower silicon content in comparison with the UIDL (Figure 4.4 (c) - spot 3).

From Figure 4.4 (a), a smooth interface is observed between the steel substrate and the coating layer; it has been attributed to the effect of silicon addition [31,51]. Moreover, silicon has an influence on the thickness of the LIDL which is a hard and brittle phase [31,51,53]; the cracks seen in the interdiffusion layer are probably originated in the LIDL. The proposed mechanism, suggested in the literature, is that silicon occupies the vacancies in the lattice of the corresponding phase for the LIDL, suppressing its growth and promoting the growth of the UIDL which is a ductile phase [8,19,51,52]. The exact stoichiometry of the two different phases formed in the IDL after hot-dipping process is still a subject of many controversies in the literature. These phase formation and growth are

strongly dependent on the molten bath chemical composition and on the hot-dip process parameters [51,52,101].

**Figure 4.4 - Cross section morphology of as-received 22MnB5 steel coated with hot-dip Al-Si (Si 10% in mass fraction): (a) scanning backscattered image showing the main different constituents in the coating layer and an inset image highlighting the interface between coating layer and steel substrate; (b) EDS elemental mapping for O, Al, Si and Fe; (c) EDS point ID representing the semi-quantitative composition of the areas highlighted in (a)**

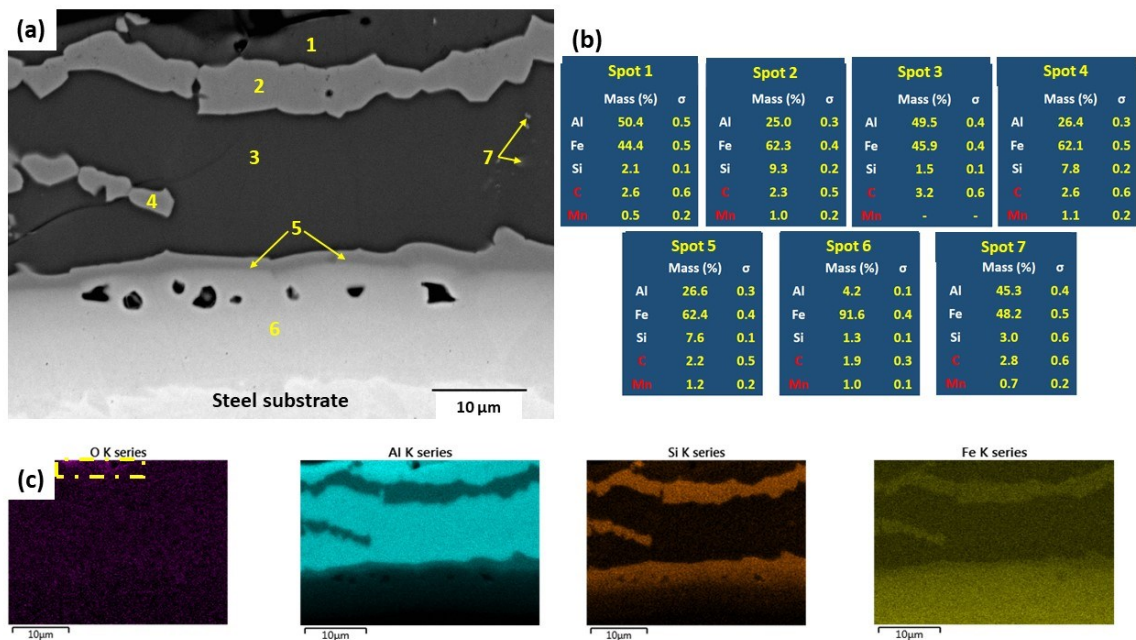


Source: Author

The effect of hot stamping on the coating morphology is shown in Figure 4.5 (a). After the thermo-mechanical process a multi-layered structure is formed, mostly related to the diffusion of iron from the steel substrate into the coating layer [6,8,14,16,18,19,24]. The first highlight is related to the coating thickness which is higher than the specified one for the AS80 coating (14 μm) [62]. The PHS condition presents a coating layer around 25 μm thick. This increment is also related to the diffusion of iron from the steel substrate towards the coating layer [8,16,19,24]. The coating on the PHS sample can be characterised by six different sublayers. Nevertheless, according to the semi-quantitative analyses shown in Figure 4.5 (b), layers 1 and 3 have similar composition, being enriched in aluminium and designated as Al-rich phases. The layers 2, 4 and 5 also show similarity in their chemical compositions being characterised as Fe/Si-rich sublayers, based on the results shown in Figure 4.5 (b) and also the EDS mappings shown in Figure 4.5 (c). As seen in Figure 4.5 (a) the sublayers 2 and 5 are continuous, except for the presence of damages often seen in PHS (see Figure 4.1 (b)), such as cracks, which may cause their discontinuity. On the other hand,

the sublayer 4 is discontinuous and often seen as islands morphology, similar to the small precipitates indicated by arrows as spot number 7. Fan et al. [24] have shown that changing the process parameters, such as austenitisation time, promotes the formation of sublayers initially present as islands of precipitates.

**Figure 4.5 - Cross section morphology of press-hardened 22MnB5 steel coated with hot-dip Al-Si (Si 10 % in mass fraction): (a) scanning backscattered image showing the main different constituents in the coating layer; (b) EDS point ID representing the semi-quantitative composition of the highlighted areas in (a); (c) EDS elemental mapping for O, Al, Si and Fe**



Source: Author

The IDL (Figure 4.5 (a) - number 6) adjacent to the steel substrate is mainly composed of iron and little amounts of aluminium and silicon. Although, the spot number 6 in Figure 4.5 (b) shows little amounts of aluminium and silicon, the EDS mapping in Figure 4.5 (c) shows that mainly the silicon content decreases gradually throughout the IDL. Moreover, voids are seen mainly in the IDL, indicating different diffusion among the chemical elements [8,16,24].

It is important to point out the absence of precipitates in the coating cross section. After the thermo-mechanical process, silicon is present in solid solution and its concentration varies among the sublayers [8,19]. However, a high silicon content is seen in the Fe-rich layers (Figure 4.5 (a) - layers 2, 4 and 5). According to the literature, the number of sublayers as well as their chemical composition are strongly dependent on the austenitisation conditions during hot stamping [19,52]. Oxygen is seen in the EDS mappings for both conditions. It suggests the presence of an oxide layer at the outer surface which may play an

important role on the corrosion mechanism. However, as seen at the top surface presented in Figure 4.3, and less evident in the EDS oxygen map for PHS (yellow dashed line in Figure 4.5 (c)), the concentration of oxygen seems to be higher, suggesting that the oxide layer formed at the outer surface after hot stamping is thicker than for AR sample, as also shown in previous studies [8,19,24]. This thicker oxide layer may play an important role in the corrosion behaviour of the PHS samples.

#### 4.4 Discussion

The hot-stamping process alters both surface and cross-section morphology of the Al-Si coating system, mainly influenced by the iron diffusion. The austenitisation temperatures during hot stamping exceed the melting temperature of the aluminium-silicon alloy, which is 577 °C, as shown in the equilibrium diagram in Figure 4.6 (a). However, even though the exact stoichiometry of the intermetallics has not been established, the equilibrium diagrams shown in Figure 4.6 (c-e) indicate that liquid phase can be formed in the Al-Fe-Si ternary system from 600 °C to 800 °C. On the other hand, the binary intermetallic phases formed in the Al-Fe system (Figure 4.6 (b)) show high melting temperatures, exceeding the austenitisation temperature during hot stamping. Therefore, the first phenomenon which takes place during austenitisation is the partial melting of the primary Al-Si structure; including the aluminium coating matrix and some ternary intermetallics. Then, the metallurgical reactions occur in the solid/liquid state. The former precipitates may become enriched in iron, as it diffuses from the steel substrate, and they are rearranged forming sublayers.

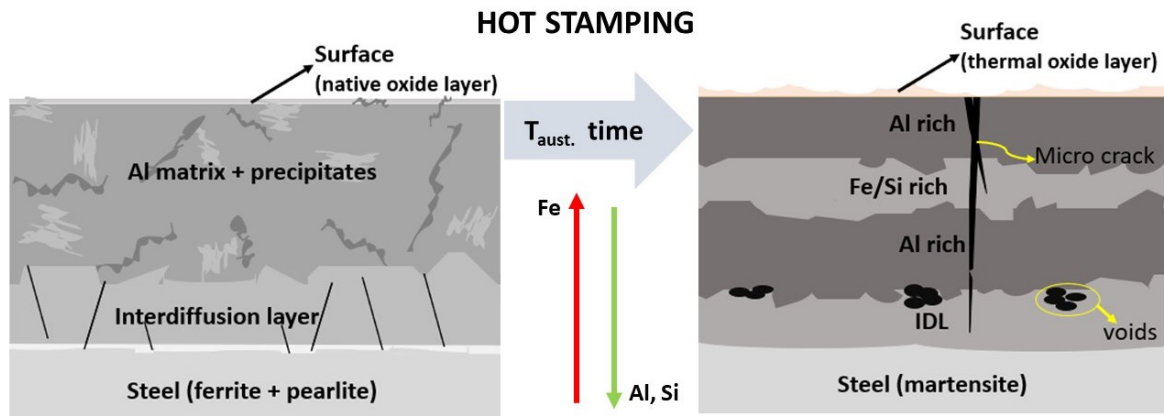
After hot stamping, the precipitates are not seen at the surface. Those precipitates have been reported to be nobler than the aluminium coating matrix [31]. Therefore, their absence after hot stamping may decrease the susceptibility for localised corrosion of the system. However, micro cracks are seen which may be detrimental for several properties, such as corrosion and mechanical properties. According to the literature, the cracks are related to the thermal expansion during hot stamping [24,60]. Nonetheless, the preferential direction of the cracks at the surface (Figure 4.3) may indicate that they are probably formed due to mechanical load (forming step).



The PHS surface is also rough and pores are present. Fan et al. [18] have attributed the roughness to the formation of Al-Fe intermetallic phases and the contact with the press tools. Indeed, the hot stamping conditions further the diffusion of iron towards the surface. Allély et al. [7] have characterised the surface of PHS sample as a mixture of oxides which consists of aluminium, iron and silicon. This finding agrees with the EDS analyses, Figure 4.5, which indicates iron, aluminium and silicon in combination with oxygen. Nevertheless, there is a lack in literature about the nature of the oxide layer for PHS coated with Al-Si. Most of the studies have focused on the effect of the formation of Fe-based oxides at the surface of bare steel showing that it is detrimental to the Al-Si coating adhesion [102]. Fan et al.[24] investigated the formation of thermal oxides on PHS coated with Al-Si. They pointed out that the oxidation is very limited due to the low diffusion of oxygen throughout the coating layer. In addition, Fan et al. [16] highlighted the influence of the oxide layer of PHS on the resistance spot-welding (RSW) process, demonstrating that, due to its small thickness and good electrical conductivity of the Al-Fe phases, the PHS coated with Al-Si shows good welding properties.

As displayed in Figure 4.5, hot stamping promotes the formation of a sublayered system seen in the cross section. It is important to point out that, before hot stamping, silicon is presented as precipitates in the cross section of the coating matrix but, during the thermo-mechanical process, it is rearranged in different sublayers. The influence of silicon addition in hot-dip aluminised steels, used for hot-stamping applications, was intensively discussed by Windmann et al. [8,19]. Silicon plays an important role on the formation of Fe-Al intermetallic compounds. The transformation of these compounds has a direct relationship with the hot-stamping parameters, such as austenitisation temperature and soaking time. The formation of  $Al_{13}Fe_4$  ( $\theta$ -phase) is attributed to the silicon content [52,60]; the higher the silicon addition, the more pronounced formation of ternary Al-Fe-Si intermetallics and the more reduced the formation rate of  $Al_{13}Fe_4$ . In addition, as other authors pointed out, silicon suppresses the formation of  $Al_5Fe_2$  ( $\eta$ -phase), occupying the vacancies in its lattice [52,60]. Figure 4.7 summarises the changes on the coating morphology due to chemical diffusion which takes place during hot stamping.

**Figure 4.7 - Schematic diagram of the changes on Al-Si coating morphology due to the chemical diffusion as a function of hot-stamping parameters illustrating the formation of intermetallic sublayers**



Source: Author

Voids and micro cracks are also observed in the cross section of the PHS sample (Figure 4.1 and Figure 4.5); both are related to the fast chemical diffusion during the hot-stamping process. The Kirkendall effect is often pointed out in the literature as the reason for a void formation. This is a consequence of the diffusion rate difference of two atoms: in this case Fe and Al. The difference in diffusion rate causes a net flux of vacancies at the interface resulting in voids [60,103]. The Kirkendall voids play a crucial role in crack initiation and it has been reported that the number of voids increases as the soaking time (austenitisation temperature) is prolonged. The cracks are also a consequence of the low fracture toughness of the sublayers which means that the sublayers formed after hot stamping are brittle [8,35,56,60,104].

However, the cracks do not reach the steel substrate and they are limited to the IDL, as represented in Figure 4.7. The reason is related to the similar thermal expansion coefficient of the IDL and the steel substrate [60]. In fact, the IDL is mainly composed of iron; however, it has ferritic microstructure whereas the steel substrate may present a fully martensitic microstructure. The aluminium diffusion towards the steel substrate, present in the IDL, plays an important role on the ferrite stabilisation inhibiting the martensite transformation during the quenching [19].

#### 4.5 Conclusion

The hot stamping process changes the surface conditions as well as the cross-section morphology of the Al-Si coating. The main highlights can be drawn:

- i. Diffusion is the major phenomenon which alters the coating morphology and the composition.
- ii. The whole coating layer becomes enriched in iron. Even the surface comprises higher iron content than aluminium.
- iii. The thermo-mechanical process promotes the formation of defects, such as micro cracks and voids. The latter is related to the fast diffusion whereas the former is a consequence of the thermal expansion and the mechanical load.
- iv. Precipitates seen in the AR sample condition are no longer present in a PHS sample. The coating morphology consists of a multi-layered system in which the sublayers are either enriched in Al or in Fe/Si.
- v. The formation of PHS coating morphology consists of a partial melting of the coating and the enrichment of the primary precipitates in iron; then, they are rearranged as sublayers.

## CHAPTER 5 - Electrochemical behaviour of 22MnB5 steel coated with hot-dip Al-Si before and after hot-stamping process investigated by means of scanning Kelvin probe microscopy<sup>3</sup>

### 5.1 Introduction

The standard electrochemical measurements show the overall behaviour of the sample conditions in different corrosive media. However, due to the complexity of the metallic coating system, either before or after the hot-stamping process, local electrochemical measurements are required in order to evaluate the effect of each sublayer at the cross section in terms of corrosion properties. Hence, this chapter aimed at investigating the effect of the hot-stamping process on the electrochemical behaviour of 22MnB5 steel coated with hot-dip Al-Si (10 % Si in mass fraction) by means of general and localised electrochemical techniques, with a special focus on the influence of each sublayer of the metallic coating on the corrosion behaviour.

### 5.2 Experimental procedure

#### 5.2.1 Global electrochemical measurements and immersion tests

Electrochemical tests were carried out using a three-electrode cell configuration consisting of an Ag|AgCl| 3 mol·L<sup>-1</sup>·KCl as a reference electrode (RE), a platinum grid as counter electrode (CE) and the samples working electrode (WE). Bare steel (ferrite-pearlite microstructure), AR and PHS samples were evaluated. The open circuit potential (*OCP*) was measured in aerated 5.0 % NaCl solution (in mass fraction) for 1 h. After *OCP* measurements, anodic polarisation curves were obtained by means of linear sweep voltammetry (*LSV*), starting from 200 mV below the *OCP* with sweep rate of 1 mV·s<sup>-1</sup>, which is a standard procedure. All tests were carried out at room temperature and the working electrode surface was a circular region with 1 cm in diameter. Moreover, AR and PHS

---

<sup>3</sup> This chapter has been published as a scientific paper. COUTO, C. P.; REVILLA, R. I.; COLOSIO, M. A.; COSTA, I.; PANOSSIAN, Z.; DE GRAEVE, I.; TERRY, H.; ROSSI, J. L. Electrochemical behaviour of 22MnB5 steel coated with hot-dip Al-Si before and after hot-stamping process investigated by means of scanning Kelvin probe microscopy. *Corrosion Science*, 2020. <https://doi.org/10.1016/j.corsci.2020.108811>

samples were also immersed in 3.5 % NaCl solution (% in mass fraction) for 120 min. The samples were removed from the solution after 10 min, 30 min, 60 min and 120 min of exposure and then rinsed in deionized water and dried in a cold stream of air.

### 5.2.2 Scanning Kelvin probe microscopy

The Volta potential and topography analyses were carried out, at the samples' cross-section, by means of a scanning Kelvin probe force microscopy (SKPFM) technique at a commercial atomic force microscope. These measurements were performed under ambient conditions using rectangular conductive cantilevers with a Pt/Ir coating, a resonant frequency of 50 kHz to 70 kHz and a spring constant of  $1 \text{ N}\cdot\text{m}^{-1}$  to  $5 \text{ N}\cdot\text{m}^{-1}$ . Moreover, highly oriented pyrolytic graphite (HOPG) was used as a reference material for the calibration of the measured Volta potential. The cross sections of AR and PHS samples were analysed.

Topographic and corresponding potential images were simultaneously obtained using a dynamic mode with a single pass methodology. The potential signal recorded was mathematically inverted (multiplied by -1) in order to reflect the true relation of the Volta potential values and the surface under investigation [31,90,94,95]. Furthermore, the distribution of Volta potential will be represented by means of histograms. The histograms were constructed based on the Volta potential map, correspondent to a scanned area of  $40\times 40 \mu\text{m}^2$  which corresponds to a mapping of  $512\times 512$  pixels. Each pixel represents a potential value. Therefore, each histogram is constructed with  $512\times 512$  of potential. The intensity represents the count frequency.

## 5.3 Results

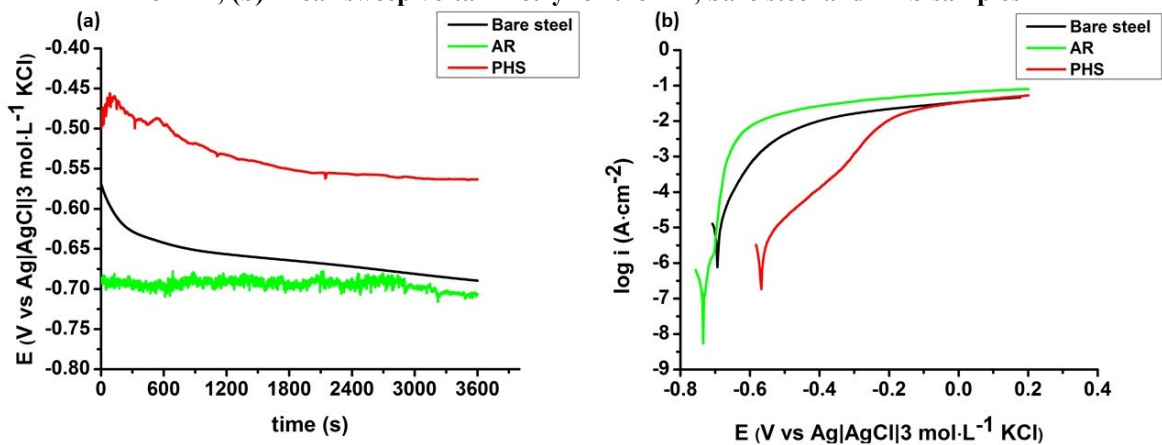
### 5.3.1 Electrochemical measurements

The evolution of *OCP* for 1 h of immersion in a 5.0 % NaCl solution (% in mass) and the anodic polarisation curves obtained by linear sweep voltammetry (LSV) technique, after *OCP* measurements, are displayed in Figure 5.1. These results were selected out among the others obtained and they represent the trend for each sample condition. According to Figure 5.1 (a), after 1 h of immersion, it is seen that both PHS and bare steel samples show a slight decrease on the *OCP* (about 100 mV) from the beginning to the end of the measurements. This may be related to the dissolution of the oxide layer in the corrosive medium [29]. On the other hand, the AR condition present the smallest *OCP* variation ( $\pm 10 \text{ mV}$ ) during the

measurement. However, despite its small *OCP* variation the AR condition shows the noisiest potential evolution among the tested conditions. This is a characteristic of metastable pits which consists of continuous localised breakdown and repassivation of the oxide layer [98]. The *OCP* of PHS sample is higher than that corresponding to the AR one, suggesting that the driving force for cathodic protection may decrease after hot stamping. Nevertheless, after 1 h of measurement the *OCP* of all samples were stable.

The average *OCP* values, at  $t = 3600$  s, (and the corresponding standard deviation values) for each sample condition are shown in Table 5.1. PHS sample shows the highest average *OCP* while the AR presents the lowest average one. These results show that the hot-stamping process causes the ennoblement of the coating. The shift of *OCP* towards nobler values may be related to the iron enrichment into the coating layer and the formation of a thermal oxide layer as well. However, the bare steel sample presents *OCP* values between PHS and AR. This suggests that the application of Al-Si coating onto steel substrate increases the susceptibility to corrosion of the substrate exposed at the pores. Based on the average *OCP* values a galvanic series can be established:  $OCP_{AR} < OCP_{bare\ steel} < OCP_{PHS}$ .

Figure 5.1 - Electrochemical tests in a 5 % NaCl solution (% in mass fraction): (a) evolution of *OCP* for 1 h; (b) linear sweep voltammetry for the AR, bare steel and PHS samples



Source: Author

The representative anodic polarisation curves of the sample's conditions are shown in Figure 5.1 (b). All curves present an active behaviour in 5.0 % NaCl solution (% in mass fraction). This behaviour for the AR sample can be related to the breakdown of the passive layer in high  $Cl^-$  medium [25]. Moreover, a sudden increase of the current is seen just after the corrosion potential ( $E^*$ ) for all samples. However, the PHS sample displays the slowest increment of the current. This could be related to the presence of a thermal oxide layer. Another hypothesis is the presence of the Fe/Si-rich sublayers present in the PHS coating (as

seen in Figure 4.4 (a)). Although the LSV measurements were carried out at the samples surfaces, at the end of the tests it was seen the exposure of the steel substrate. This may be the reason why at the end of the measurements the curves show very close values of current density in the anodic branch (order of  $10^{-2}$  A·cm<sup>-2</sup>). However, the plateau present in Figure 5.1 (b) may also indicate concentration polarisation. In this case, mass transport is predominantly controlled by diffusion [75]. Nevertheless, to confirm this hypothesis, a different experimental set up should be considered, which includes a rotating disc electrode [75]. Table 5.1 also shows the average values  $E^*$  and their standard deviations.

**Table 5.1 - Average values of  $OCP$ ,  $E^*$  and their corresponding standard deviation values for bare steel, AR and PHS samples in 5.0 % NaCl solution (% in mass fraction)**

Sample condition	$OCP$ ( $t = 3600$ s)		$E^*$	
	(V vs Ag AgCl KCl sat.)		(V vs Ag AgCl KCl sat.)	
	Average	Standard deviation	Average	Standard deviation
Bare	-0.664	0.037	-0.668	0.037
AR	-0.722	0.022	-0.705	0.045
PHS	-0.562	0.002	-0.563	0.008

Source: Author

Based on the results presented in Table 5.1 the average  $E^*$  shows the same trend of the  $OCP$ . The PHS sample has the noblest average  $E^*$  (-0.563 V vs Ag|AgCl|KCl sat.) whereas the AR condition present the lowest one (-0.705 V vs Ag|AgCl|KCl sat.). Additionally, the average  $E^*$  difference between the bare steel and the AR condition is small, only 37 mV. Allély et al. [7] have pointed out that the minimum potential difference for cathodic protection is 50 mV. Nevertheless, the electrochemical results ( $OCP$  and LSV) shows that the hot-stamping process enhances the corrosion potential of the material.

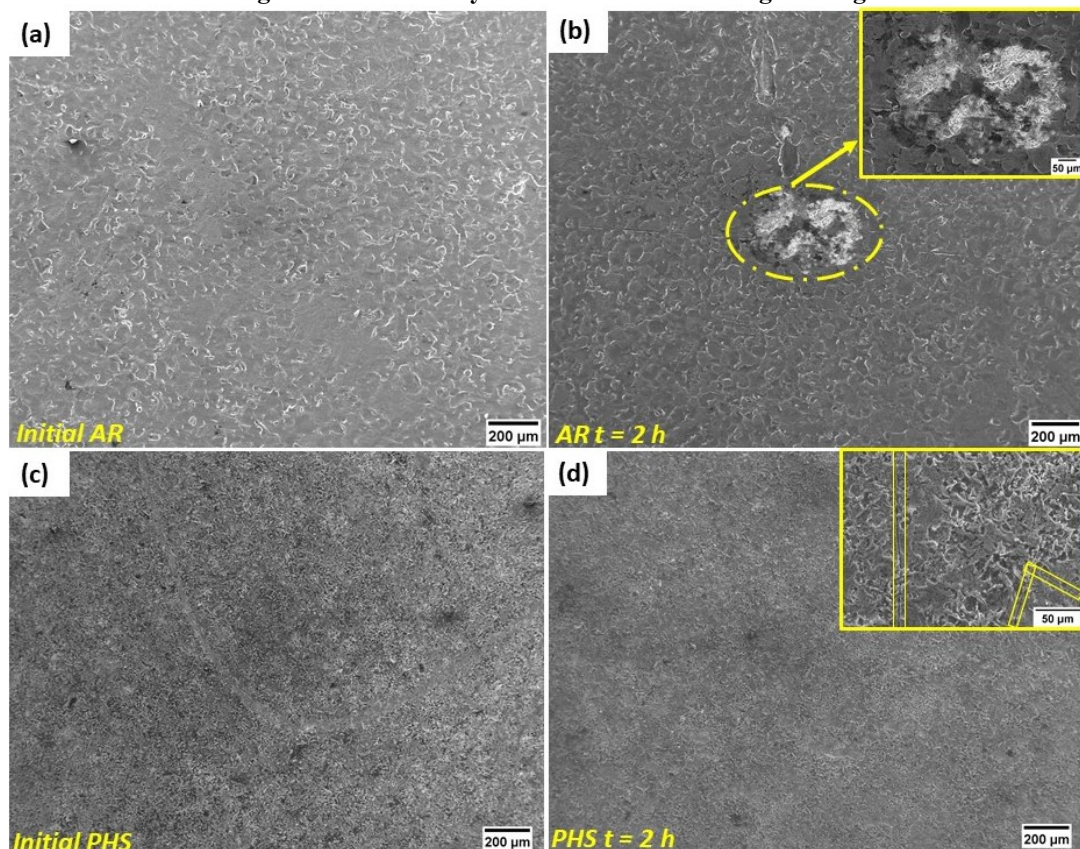
### 5.3.2 Immersion test

In order to understand the influence of hot stamping on the corrosion initiation, immersion tests were performed in a 3.5 % NaCl solution (% in mass fraction) for 2 h. The surfaces of the AR and PHS samples before and after 2 h of immersion are presented in Figure 5.2.

The surface of the AR sample seen in Figure 5.2 (a) is in agreement with the results previously presented in Figure 4.2 (a). The coating surface consists of an aluminium matrix with some precipitates randomly distributed. From the first 10 min of immersion, initiation of localised corrosion was observed at the top surface of the AR sample. Although the  $OCP$  measurements were carried out for 1 h, it was observed that the corrosive attack progressed by increasing the immersion time. After 2 h in chloride medium, severe localised

corrosion was observed at the sample surface, as shown in Figure 5.2 (b) (and its inset image at higher magnification). The coating corrosion starts around the precipitates which, according to the literature, behave cathodically versus the aluminium matrix [31]. Therefore, they play a role of preferential site for cathodic reaction. Even though the surface of the PHS condition consists of micro cracks and pores (seen in Figure 4.3 but not shown in the selected area in Figure 5.2 (c)), localised corrosion is not observed in Figure 5.2 (d). This can be better seen in the inset image in Figure 5.2 (d) which displays cracks and the roughness characteristic of the PHS surface. Moreover, a brightest contrast can be observed in the inset image which may be correlated to the corrosive attack, and consequently, the formation of corrosion products.

**Figure 5.2 - Scanning secondary electron images of the surface before and after immersion in 3.5 % NaCl (%in mass fraction): (a) AR sample before immersion; (b) AR sample after 2 h of immersion and an inset image from the attacked area; (c) PHS before immersion; (d) PHS after 2 h of immersion and an inset image from a randomly area in the surface at higher magnification**



Source: Author

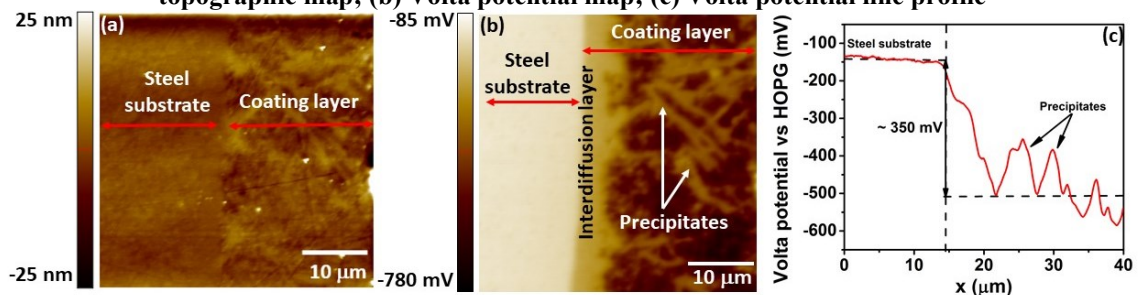
Despite that small area analysed and the short time of immersion, the immersion tests indicate the corrosion mechanism in which sample condition is more prone: localised corrosion in the AR sample and generalised corrosion in the PHS. The latter has been

confirmed by Dosdat et al. [11]; furthermore, the authors have pointed out the high iron content at the coating outer layer to explain the generalised corrosion mechanism.

### 5.3.3 Scanning Kelvin probe force microscopy

The topographic map (a), the Volta-potential map (b) and a randomly chosen line-profile (c) across the coating for AR condition are shown in Figure 5.3. From the topographic map, Figure 5.3 (a), it is difficult to distinguish the two different layers present in the coating. However, these two layers and the precipitates can be easily distinguished in the Volta-potential map (Figure 5.3 (b)), due to their different contrasts. In addition, the Volta-potential map shows the cathodic behaviour of the steel substrate versus the coating layer. The brighter contrast of the interdiffusion layer and the precipitates indicates that they are nobler than the aluminium coating matrix which is in agreement with previously reported studies [31,94].

**Figure 5.3 - Cross-section of 22MnB5 steel coated with hot-dip Al-Si prior hot-stamping process: (a) topographic map; (b) Volta potential map; (c) Volta potential line profile**



Source: Author

The Volta-potential line profile, Figure 5.3 (c), shows that there is a high potential difference between the steel substrate and the coating layer. This difference is around 350 mV with the steel substrate being nobler than the coating layer. Based on this Volta-potential difference, the coating layer could probably provide some cathodic protection to the steel substrate. However, as already mentioned, the anodic behaviour of Al-Si coatings depends on the concentration of chloride ions in the environment [25]. The Volta potential decreases across the coating layer which may be attributed to the decrease of iron content from the interdiffusion layer towards the outer layer. Moreover, the potential varies in the coating layer due to the presence of different precipitates characterised in Figure 4.4. Both Volta-potential map and line profile prove that the precipitates behave cathodically in comparison with the coating aluminium matrix. Therefore, it justifies the local attack in the AR sample as suggested by the immersion test Figure 5.2.

The histogram plot of the Volta-potential map, from the cross section of the AR sample, Figure 5.3 (b), is seen in Figure 5.4. The histograms represent a multimodal Gaussian distribution. The peaks in the histograms can be correlated to different constituents in the area measured by means of SKPFM. Moreover, it is possible to evaluate the contribution of every different constituent on the Volta-potential distribution [96,105,106].

**Figure 5.4 - Histogram of Volta-potential distribution, based on the Volta-potential map of the AR sample, showing the contribution of the three main areas: steel substrate, interdiffusion layer and the aluminium coating matrix (free layer)**

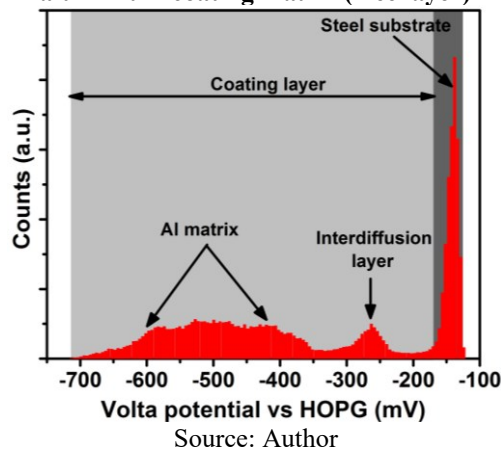
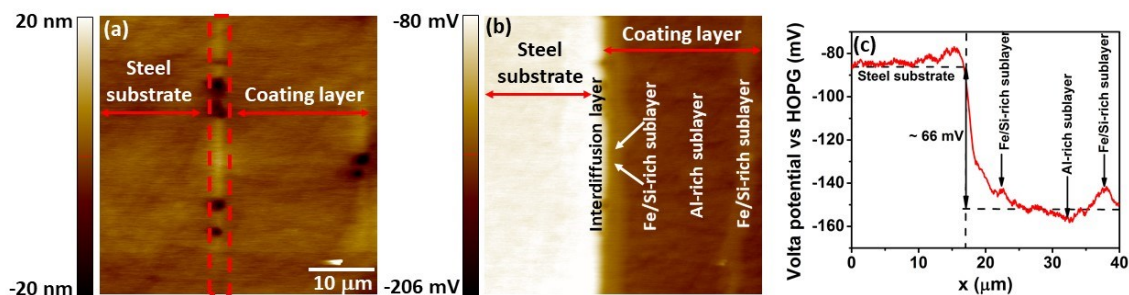


Figure 5.4 shows that three different constituents contribute to the Volta-potential distribution. The sharpest peak seen at the highest potential region, with an average value around -138 mV vs HOPG, is related to the steel substrate. The corresponding shape of the peak may be related to the major presence of iron in the steel substrate. If different constituents with different electrochemical activities are present around the same potential region, the peaks tend to be broader. The interdiffusion layer, which is composed of Fe-Al, presents a quite symmetric peak due to its composition homogeneity. The intensity is lower because it is a thinner layer in comparison with the steel substrate and the coating matrix, as clearly seen in Figure 5.3 (b). The potential of the interdiffusion layer has an average value around -263 mV vs HOPG. The peak corresponding to the Al-Si coating matrix is broader than the others, showing clear variations in Volta potential. The average potential value of the coating matrix is around -488 mV vs HOPG. Moreover, a tail-like shape is observed in the left side of the broader area. The findings from the histogram in Figure 5.4 are in accordance with those previously reported by Sarvghad-Moghaddam et al. [106]. They have attributed the presence of precipitates in the Al matrix as the cause of the deviation in the Volta potential, leading to a broader peak. In addition to this, the tail-like shape may be related to the aluminium signal, less noble phase than the precipitates. As shown in the Volta-

potential line profile (Figure 5.3 (c)), the histogram (Figure 5.4) confirms that the steel substrate has the noblest Volta potential, while the aluminium has the lowest one. The interdiffusion layer presents an intermediate potential, however, the Volta potential is shifted towards the Volta potential of the steel substrate due to the high amount of iron in this layer.

The topographic map (a), the Volta-potential map (b) and the Volta-potential line profile (c) for a randomly chosen line from the Volta-potential map are displayed in Figure 5.5 for the PHS condition. From the topographic map, Figure 5.5 (a), it is not clear the difference between the steel substrate and the coating layer. However, correlating the topographic map with the Volta-potential map, Figure 5.5 (b), it is possible to distinguish a brighter contrast line which indicates the transition from the steel substrate to the coating layer. It is characterised as the interdiffusion layer, preferential site for Kirkendall voids formation [60]. From the Volta-potential map, the cathodic behaviour of the steel substrate versus the coating layer is seen. Moreover, it is possible to differentiate the sublayers which comprise the coating. Correlating Figure 4.5 and Figure 5.5 (b), it is seen that the brighter sublayers are corresponding to the Fe/Si-rich phases. Nevertheless, the contrast difference among the sublayers in the coating are not very pronounced. This indicates that there is not a high Volta-potential difference among the sublayers, as indicates Figure 5.5 (c), Volta-potential line profile. In addition to this, according to Figure 5.5 (c) the Volta-potential difference between the steel substrate and the coating greatly decreases after the hot-stamping process. This can be associated with the iron diffusion during the hot-stamping process. After the thermo-mechanical process, the Volta-potential difference between the steel substrate and the coating layer is approximately 66 mV. Additionally, the potential difference among the sublayers in the coating is small, as already indicated by the contrast difference in Figure 5.5 (b).

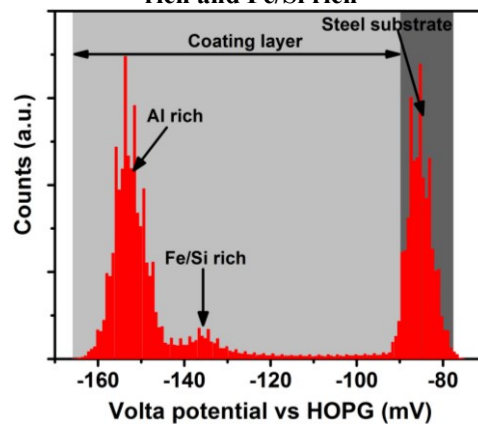
**Figure 5.5 - Cross-section of hot-stamped 22MnB5 steel coated with hot-dip Al-Si (a) topographic map; (b) Volta potential map showing the different sub layers present in the coating; (c) Volta potential line profile**



Source: Author

The Fe/Si-rich sublayers present slightly higher Volta potential than the Al-rich ones. According to the galvanic series, iron and silicon are nobler than aluminium [27–30,107] which justifies the lower potential of the Al-rich sublayers. Due to the small differences of Volta potential among the sublayers, it is hard to establish an accurate potential difference. However, in order to evaluate the contribution of the sublayers, in terms of Volta potential, the histogram of the Volta-potential map for the PHS sample is plotted in Figure 5.6.

**Figure 5.6 - Histogram of Volta potential distribution, based on the cross-section Volta potential map, of the PHS sample, showing the contribution of the steel substrate and the two different sublayers: Al rich and Fe/Si rich**



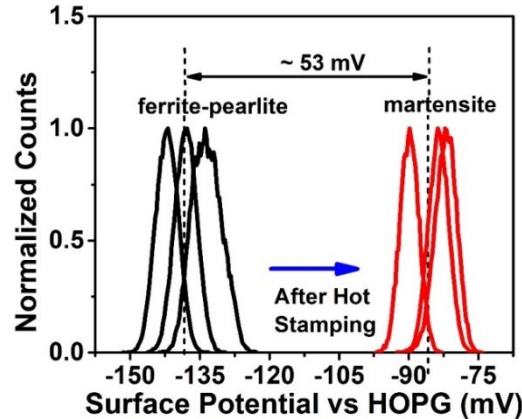
Source: Author

Three different constituents are seen in the histogram (Figure 5.6), which has a substantial influence on the Volta-potential distribution. The steel substrate and the Al-rich layer, which are the most abundant phases in the potential map shown in Figure 5.5 (b), can be identified as the two largest peaks in the histogram Figure 5.6. This is a consequence of the major influence of iron in the steel substrate and aluminium in the Al-rich layer. Additionally, they have the higher contribution on the Volta-potential distribution due to their total area size in the sample cross section, as shown also in Figure 5.5 (b). The potential of the steel substrate is around -85 mV vs HOPG, while the average potential of the Al-rich layer is approximately -154 mV vs HOPG. However, the Fe/Si-rich sublayers are thinner and discontinuous, being probably the reason why the peak corresponding to these phases is less sharp and much smaller than the others. Moreover, this phase has lower contribution on the Volta potential distribution than the others. The steel substrate shows a higher Volta potential than the two different sublayers in the coating. From the histogram, it is seen that

the Volta potential of the two sublayers in the coating are close. The Volta-potential difference between the Fe/Si-rich and Al-rich sublayer is approximately 16 mV.

The hot-stamping process also changes the potential of the steel substrate and it may be correlated with the microstructure transformation during the thermo-mechanical process. Several SKPFM measurements were performed for both, AR and PHS samples using HOPG as reference material. The average Volta-potential difference between the AR and PHS steel substrates is seen in Figure 5.7. This difference is about 53 mV. Before hot stamping the steel substrate shows a ferrite-pearlite microstructure, and its Volta potential is around -150 mV vs. HOPG. In the end of the thermo-mechanical process, a fully martensitic transformation takes place, and the Volta potential of the martensite increases to approximately -90 mV vs. HOPG.

**Figure 5.7 - Average Volta potential difference between as received Al-Si and PHS steel substrates measured versus the reference material**



Source: Author

#### 5.4 Discussion

The galvanic series drawn based on the electrochemical results from Figure 5.1, suggests that, in terms of cathodic protection, only the Al-Si coating, before hot stamping, could behave as a sacrificial anode to the steel substrate. It is important to point out that these electrochemical measurements were performed at the surface of the samples. From the microscopic characterisation, Figure 4.2, it was shown that, before hot stamping, the coating matrix is mainly composed of aluminium which is less noble than iron, according to the galvanic series [27–30,107]. After the thermo-mechanical process, the top layer surface of the coating is enriched in iron due to the chemical diffusion during hot stamping. Thus, iron enrichment of the coating layer can be the reason for the nobler corrosion potential of the

PHS sample when compared with the AR. However, the iron enrichment does not justify the reason why the *OCP* of the PHS is higher than the bare steel. In this case, it can be attributed to the presence of an oxide layer formed during the hot-stamping process as evidenced in Figure 4.5. This oxide layer can play an extra role on the protection barrier mechanism, shifting the *OCP* to nobler values.

The electrochemical results shown in Figure 5.1 are slightly different from those presented by Allély et al. [7]. In their investigation, the PHS and 22MnB5 bare steel samples stabilised at similar *OCP* values (-770 mV vs SCE), after 1 h of measurement in a 5.0 % NaCl solution (% in mass fraction). Conversely, the *OCP* of AR sample of the present work is about 100 mV lower. In terms of the corrosion potential, the galvanic series presented by Allély et al. [7] showed that the 22MnB5 bare steel had the highest corrosion potential this is the main difference from the galvanic series therewith presented. The controversies on the results can be probably explained by the possible differences in the process parameters during hot stamping. As already mentioned, these parameters vary among manufacturers, influencing the diffusion of the chemical elements and, consequently, the coating properties. It has been shown in the literature that hot-stamping parameters greatly influence the morphology-composition of the coating layer [24]. Both austenitisation temperature and soaking time are critical parameters which enhance mainly the iron diffusion into the coating layer. Furthermore, these parameters may also influence the thermal oxide layer formed during hot stamping. The nature of this thermal oxide layer, i.e., its composition, may have an effect on the electrochemical behaviour of the system. For instance, if the process conditions promote substantially the iron diffusion into the coating resulting in a thermal oxide layer mostly composed of iron oxides, the latter may play a different role on the electrochemical behaviour when compared with a material in which the process parameters promote the formation of a top layer consisting of a mixture of oxides (aluminium, iron, silicon). The controversies between the findings from Allély et al. [7] and the results presented in Figure 5.1 could be confirmed if standard procedures were adopted to produce hot-stamping components, mainly the austenitisation temperature and soaking time. Additionally, the characterisation of the oxide layer just after hot stamping is recommended to confirm the influence of the thermal oxide layer on the electrochemical behaviour.

From the electrochemical results, it is seen that there is a small corrosion potential difference between the bare steel and AR. Therefore, there is a small driving force for the Al-Si coating to provide cathodic protection to the steel substrate [7,11]. Panossian et al. [25] have found out that only in atmospheres with high chloride concentrations, Al and

Al-Si coatings offer cathodic protection to steel substrates since the coatings passive properties are lost due to  $\text{Cl}^-$  ions. However, in chloride free atmospheres, or with very low ion concentrations, Al and Al-Si coatings preserve their passive properties due to the oxide layer on the metal surface.

The immersion tests (Figure 5.2) present the high susceptibility to localised corrosion in the AR sample whereas the PHS tends to corrode in a generalised way. As Dosdat et al. [11] pointed out the appearance of red rust in PHS samples is rather related to the high amount of iron at the top coating layer than to the coating damage. The suggested higher resistance to localised corrosion for the PHS sample can be attributed to the fact that the outer layer of the coating is composed of a homogeneous Fe-Al matrix without precipitates. Despite the presence of cracks in the coating, the PHS presents the noblest corrosion potential and no localised corrosion.

The scanning Kelvin probe force microscopy has been very often reported as a useful technique to evaluate the effect of alloy elements on the formation of intermetallic phase and its influence on corrosion mechanism [81,86,91,94,97,105,108]. As shown in Figure 4.4 and Figure 4.5, both AR and PHS consist of different intermetallic phases with different properties. This layered structure might play a crucial role on the corrosion mechanism.

The Volta potential is often related to the corrosion potential. Many authors cite the study of Schmutz et al. [92] who found a linear relationship between the Volta potential and the corrosion potential for different metals. However, it is known that this behaviour has a strong dependence on the electrolyte [31]. Nevertheless, the electrochemical measurements (Figure 5.1) and the SKPFM results (Figure 5.3 and Figure 5.5) are in good agreement. Both methods indicate the ennoblement of the system after hot stamping. In addition to this, from the SKPFM analysis, it is shown that the thermo-mechanical process increases the Volta potential of both the steel substrate and the coating layer. This may be attributed to a synergistic contribution, the microstructure transformation from ferrite-pearlite into martensite, and the iron diffusion from the steel substrate towards the coating layer. The works of Sarkar et al. [109] and Fushimi et al. [110] show that martensite has higher corrosion potential than ferrite, which is in perfect agreement with our SKPFM results. In a dual-phase steel, ferrite acts as anode and the martensite plays the role of the cathode. On the other hand, even though martensite was shown to be nobler than ferrite, in earlier studies martensite was also reported to have a relatively higher corrosion rate compared to ferrite. According to Fushimi et al. [110], the electrochemical behaviour of the martensite is related

to its supersaturated structure in carbon, as well as the residual stress involved during its microstructural transformation. The latter can alter the electronic properties of the steel matrix. This influences the Fermi level and, consequently, the work function of the material.

Regarding cathodic protection, the galvanic series based on the standard electrochemical measurements, Figure 5.1, indicate that only the Al-Si coating before hot stamping could provide some cathodic protection to the steel substrate. However, care must be taken before drawing some conclusions, especially on the comparison with the SKPFM results. As already mentioned, the standard electrochemical tests were conducted at the top surface, where there is the influence of the oxide layer, even considering that the chloride ions cause the breakdown of these layers. Moreover, the steel substrate evaluated was a bare 22MnB5 steel before hot stamping (pearlite-ferrite microstructure). Therefore, an ideal approach would include also a hot-stamped bare steel (martensite microstructure) in this investigation.

The electrochemical results presented an average OCP difference between the AR condition and the bare steel of 58 mV whereas the SKPFM measurements show a Volta potential difference of 350 mV. These discrepancies can be correlated to different factors. First, principles; the standard electrochemical tests enable the measurement of the electrode potential at the electrical double layer while the SKPFM allows the measurement of the Volta potential in ambient condition (without an electrolyte). Another factor to be considered is the approach; the standard electrochemical measurements were conducted at the top surface whereas the Volta potential was scanned in the cross sections of the samples by SKPFM. It is known that Volta potential values are substantially influence by the size effect, i.e., the most predominant phase in the system may cause depletion on the smaller phase in the system [111,112]. In this case, in the PHS condition, the Volta potential of the Fe/Si-rich sublayers may be influenced by the Al-rich phases around them. Moreover, the surface of the industrial samples (see Figure 4.3) has a very high roughness, and it also presents several micro-cracks, which makes it almost impossible to carry out the local SKPFM measurements.

The main contribution that the SKPFM provides concerns the analysis of the micro-galvanic interactions between the different sublayers and constituents/precipitates within the Al-Si metallic coating. It shows that the hot-stamping process clearly decreases the driving force for cathodic protection of the steel substrate by the coating.

## 5.5 Conclusion

The hot-stamping process changes the coating morphology and, consequently, the electrochemical behaviour. The main findings can be summarised as follows:

- i. Electrochemical measurements show that the PHS sample presents the noblest corrosion potential and the slowest increment of the current in the anodic branch.
- ii. The local Volta potential shows that before hot stamping the pearlite-ferrite steel substrate is nobler than the coating layer. The SKPFM results pointed out that the interdiffusion layer and the precipitates behave cathodically to the aluminium matrix.
- iii. The Volta-potential difference between the steel substrate and the coating layer decreases substantially after the thermo-mechanical process. Before hot stamping this difference is around 350 mV whereas after hot stamping it is 66 mV.
- iv. The ennoblement of the coating layer is related to the iron enrichment while the martensite transformation is the reason for a nobler Volta potential of the steel substrate after hot stamping.
- v. A concurrent mechanism is thoroughly established, i.e., while the press hardening increases both Volta and corrosion potential of the system (steel and metallic coating) through diffusion, it diminishes the cathodic protection afforded by the coating.

## CHAPTER 6 - Depth profiling approach to evaluate the influence of hot stamping on the local electrochemical behaviour and galvanic series of hot-dip Al-Si coating on 22MnB5 steel<sup>4</sup>

### 6.1 Introduction

The effect of the hot stamping on the electrochemical behaviour of 22MnB5 steel coated with hot-dip Al-Si (Si 10 % in mass fraction) was evaluated by means of scanning Kelvin probe force microscopy (SKPFM) presenting a good lateral resolution. It was shown that the thermo-mechanical process has a great influence on the driving force for cathodic protection, since the difference of (Volta) potential between the steel substrate and the coating layer decreases. However, this technique provides insights into the behaviour of the galvanic coupling (steel/coating) in its ambient condition, considering the absence of an electrolyte. Therefore, it does not provide information about the local current flow, an important parameter to determine the kinetics of the corrosion process. This is actually the major drawback of the scanning techniques which do not allow direct corrosion current measurement [82,83,113]. Conversely, with the small-area electrode techniques, the measurement of current is directly possible.

In this chapter, the influence of hot stamping on the coating corrosion properties, considering each sublayer, was evaluated using a depth profile approach combined with localised electrochemical measurements. Layer by layer of the coating, either before or after hot stamping, was exposed by means of glow discharge optical emission spectroscopy (GDOES), after which, the electrochemical activity of each layer was evaluated using an electrochemical micro cell. This approach has been chosen to provide a better insight of thermodynamic and kinetic parameters of the localised corrosion mechanism induced by the galvanic couplings between the different layers of the coating and the steel substrate.

---

<sup>4</sup> This chapter has been published as a scientific paper: COUTO, C. P.; ANDREATTA, F.; LANZUTTI, A.; COSTA, I.; PANOSSIAN, Z.; DE GRAEVE, I.; TERRY, H.; ROSSI, J. L.; REVILLA, R. I. Depth profiling approach to evaluate the influence of hot stamping on the local electrochemical behaviour and galvanic series of hot-dip Al-Si coating on 22MnB5 steel. *Corrosion Science*, 2021. <https://doi.org/10.1016/j.corsci.2021.109435>.

## 6.2 Experimental procedure

### 6.2.1 Glow discharge optical emission spectroscopy

GDOES was equipped with a standard 4 mm diameter anode, a polychromator with 28 acquisition channels, an RF-generator (13.6 MHz) and a Quantum XP software. The analysis conditions were: argon pressure of 620 Pa and applied power of 35 W. The instrument was equipped with a 0.5 m polychromator with nitrogen purged optical path. The calibration was performed with 28 samples selected among setting up samples (SUS) and certified reference material (CRM) which were ground and polished before use. The different sputtering times to reach the different sublayers have been chosen based on a complete depth profile for each sample condition (AR and PHS).

The sputtering times established for the AR condition were: 50 s, 100 s, 250 s and 350 s. These sputtering times represent a depth of approximately 2.5  $\mu\text{m}$ , 7.5  $\mu\text{m}$ , 12.5  $\mu\text{m}$  and 17.5  $\mu\text{m}$ , respectively. Moreover, a longer sputtering was performed in order to reach the steel substrate. Otherwise, the sputtering times established for the PHS samples were: 70 s, 140 s, 280 s and 400 s; these times represent a depth close to 3  $\mu\text{m}$ , 7  $\mu\text{m}$ , 15  $\mu\text{m}$  and 21  $\mu\text{m}$  respectively. Additional sputtering of 500 s and 1000 s to reach the steel substrate were also carried out.

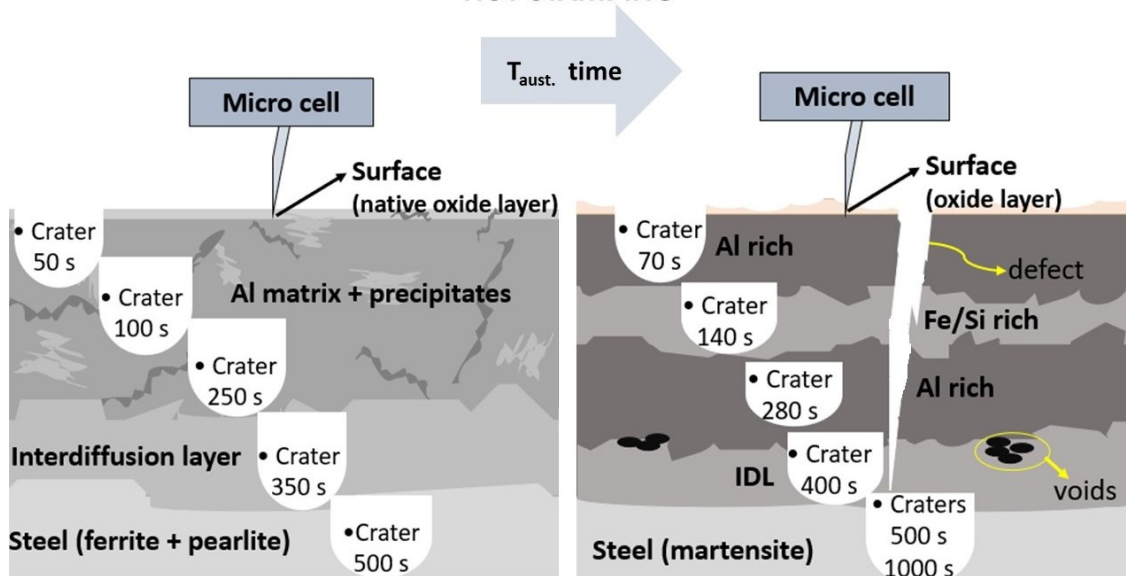
### 6.2.2 Electrochemical micro cell

Localised anodic potentiodynamic polarisation measurements were carried out in the different craters obtained by GDOES for the AR and PHS samples using the electrochemical micro-cell technique. A capillary glass with an internal diameter of 800  $\mu\text{m}$  was selected to perform the measurements. This corresponds to an area of the working electrode of  $5 \times 10^{-3} \text{ cm}^2$ . This capillary size was chosen because it is large enough to obtain results, which are less influenced by changing the amount of precipitates and / or of defects in the area of investigation (as seen in Figure 4.1), but small enough to have the ability to perform 3 to 4 measurements per crater [81].

The measurements were carried out with a current resolution in the order of 10 fA. The micro cell presented a three-electrode configuration: the sample under investigation as working electrode, a Pt counter electrode and a Ag|AgCl|3 mol·L<sup>-1</sup> KCl reference electrode. The potentiodynamic polarisations were started after a short stabilisation time without recording the open circuit potential (*OCP*). This was necessary to avoid leakage of solution from the micro capillary during the potentiodynamic polarisation tests. The scan

started at  $-200$  mV vs *OCP*, with scan rate of  $1 \text{ mV}\cdot\text{s}^{-1}$  in  $0.1 \text{ mol}\cdot\text{L}^{-1}$  NaCl solution. For each layer, at least three polarisation curves were recorded. Additionally, localised anodic potentiodynamic polarisations were recorded on the non-sputtered top surfaces of AR and PHS samples. Finally, to confirm the position of the craters made by GDOES, they were also sectioned after the potentiodynamic polarisation and analysed by SEM (results not shown). The schematic experimental approach of the depth-profile local electrochemical measurements is shown in Figure 6.1. Nevertheless, it is important to mention that it was used a different sample for each crater made.

**Figure 6.1 - Schematic experimental approach used during the depth-profile local electrochemical measurements, showing the influence of the hot-stamping process on the 22MnB5 steel coated with hot-dip Al-Si**



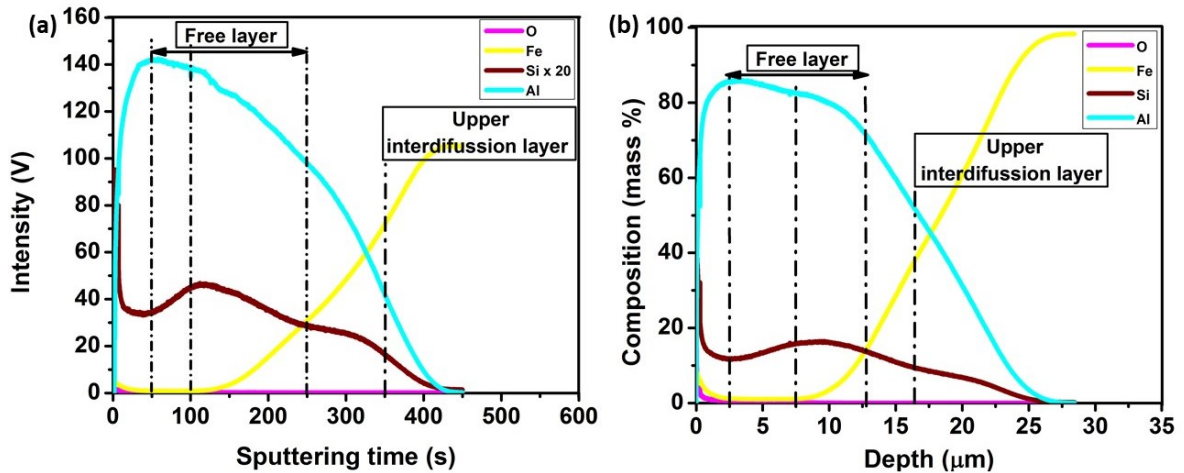
## 6.3 Results

### 6.3.1 GDOES depth profile

GDOES is used here as a tool for sample preparation for electrochemical depth profiling with the micro cell, but of course it also gives valuable compositional data that shows the diffusion profile of the elements from the coating layer towards the steel substrate and vice-versa. The GDOES depth profiles for the AR sample are shown in Figure 6.2. From the depth profile (Figure 6.2 (b)), it is seen that the thickness of the coating layer is about  $25 \mu\text{m}$ , mainly composed of aluminium, in agreement with the results shown in Figure 4.4. The

amount of aluminium decreases towards the steel substrate, while the iron content increases from the depth of 10  $\mu\text{m}$ . The diffusion interface for the Al-Fe diffusion couple is approximately at 17  $\mu\text{m}$ . At this depth, the composition of both aluminium and iron is about 45 % in mass fraction. The silicon profile shows that it is distributed in the whole coating layer. The distribution of silicon seen in the GDOES profile is also supported by the morphology of the cross section presented in Figure 4.4 in which silicon is seen in the free layer (FL) randomly distributed precipitates.

**Figure 6.2- GDOES profiles for AR sample. (a) sputtering time profile showing by dashed lines the craters obtained after 50 s, 100 s, 250 and 300 s of sputtering; (b) depth profile showing the craters obtained as a function of their depth and elemental chemical composition for Al, Si, Fe and O**

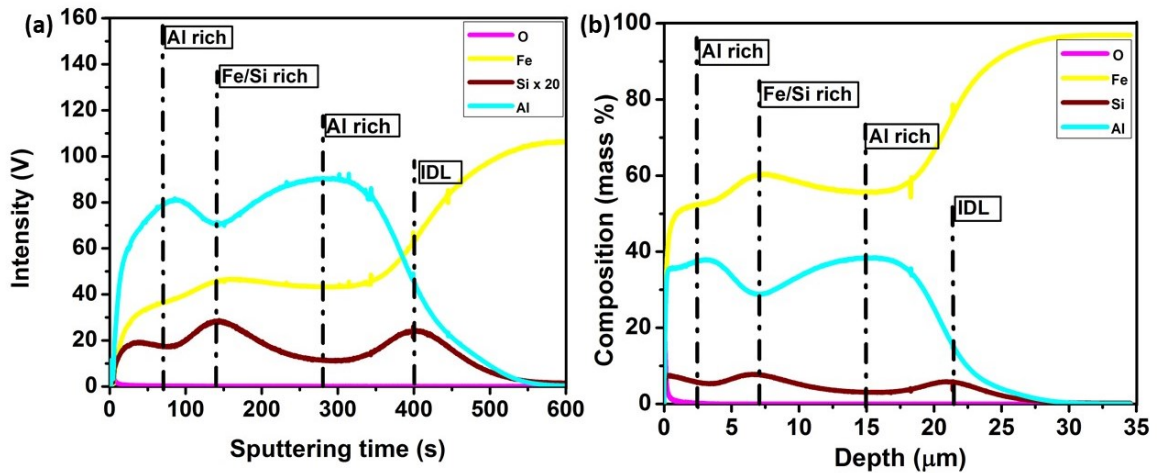


Source: Author

Based on the entire depth profile of the AR sample, it was possible to determine where the craters should be made to perform the local electrochemical measurements. Each crater was determined by the change in the slope shown in the depth profile. These results were essential in the choice of the sputtering times for the sample preparation (for the micro-cell analyses that are presented in the next section). Correlating Figure 4.4 and Figure 6.2 (b), it is possible to determine that the craters obtained for 50 s, 100 s and 250 s of sputtering are regarding the FL (Figure 4.4 (c) - spot 1). Additionally, the crater obtained after 350 s of sputtering is related to the interdiffusion layer (IDL); most probably to the upper interdiffusion layer (UIDL) (Figure 4.4 (c) - spot 2). It is possible that there is some residual elementary contribution of the adjacent layer in the UIDL crater. Additionally, a deeper sputtering was made in order to obtain a crater in the steel substrate (not shown in Figure 6.2). The position of the craters was confirmed by SEM analysis of their cross-section.

The GDOES profiles for the PHS sample which were used as reference to determine where the craters should be made are shown in Figure 6.3. The depth profile for the PHS sample, Figure 6.3 (b), confirms that the top surface of PHS sample is enriched in iron as the EDS results presented in Chapter 4 (Figure 4.3). Moreover, the depth profile shows that the coating layer also has a thickness of around 25  $\mu\text{m}$ . It is important to highlight that when the iron content increases (characterised by slight peaks in the iron profile - yellow line in Figure 6.3 (b)) the amount of silicon also increases, while the aluminium content decreases (see line profiles in Figure 6.3). Based on this, the different sublayers of the coating can be easily identified. Each crater determined in Figure 6.3 can be correlated with the sublayers in Figure 4.5.

**Figure 6.3 - GDOES profiles for PHS condition. (a) sputtering time profile showing by dashed lines the craters obtained after 70 s, 140 s, 280 and 400 s of sputtering; (b) depth profile showing the craters obtained as a function of their depth and elemental chemical composition for Al, Si, Fe and O**



Source: Author

The craters obtained after a sputtering for 70 s and 280 s reached the sublayers 1 and 3 which are Al-rich sublayers (see Figure 4.5 - spots 1 and 3). The crater after 140 s of sputtering is correlated to layer 2 which is Fe/Si-rich (Figure 4.5 - spot2); and the crater obtained at 400 s of sputtering is correlated to the IDL (Fe-rich layer). Although Figure 4.5 (b) - spot 6 shows that the IDL consists of a low silicon content (1.3 % in mass fraction), the GDOES depth profile shows that the crater obtained after 300 s of sputtering presents a high silicon content (about 10% in mass fraction). Thus, it was established that the crater made in the IDL corresponds to the region with voids in the top section of the IDL (see Figure 4.5 (a)), because at this position the silicon content is higher as suggested by the EDS mapping in Figure 4.5 (c). In addition to the craters made in the coating layer, two extra craters were

made in order to reach the steel substrate at 500 s and 1000 s of sputtering (not shown in Figure 6.3). As already mentioned, the position of the craters was also confirmed by their cross-section SEM analyses (not presented).

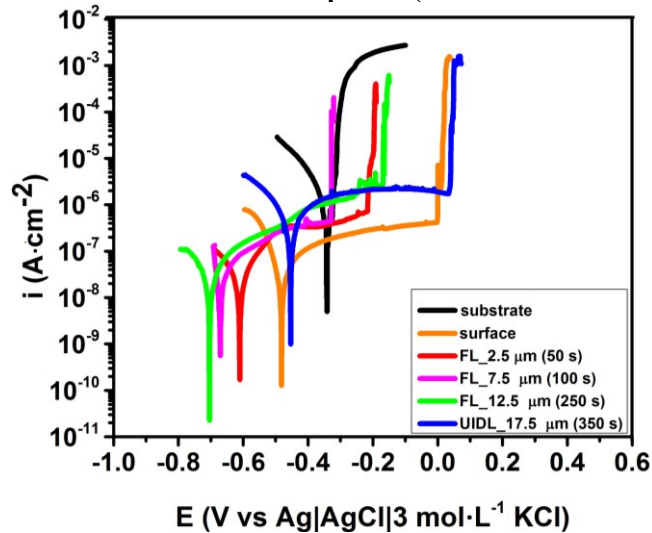
### 6.3.2 Local anodic potentiodynamic polarisation using electrochemical micro cell as a function of depth

Representative anodic potentiodynamic polarisation curves obtained in the craters made at different positions of the coating layer, on the steel substrate and on the surface of the sample for the AR material are shown in Figure 6.4. These individual curves were selected out of the several measurements for each position (at least three). They are not average curves, but they do show the important electrochemical trends. Table 6.1 shows the average values of corrosion potential ( $E^*$ ) the breakdown potential ( $E_{BD}$ ) and their corresponding standard deviations.

As can be seen in Figure 6.4, except for the substrate, the shape of all the curves is very similar. A passive behaviour is seen in all of them and a sudden increase of the current is observed at a potential, known as the breakdown potential ( $E_{BD}$ ), specific for each curve, which represent the breakdown of the passive film [31]. On the contrary, for the substrate the anodic potentiodynamic polarisation curve shows an active behaviour, characteristic of carbon steel in chloride media [31].

The passive behaviour of the coating layers is characteristic of Al-based alloys [95,114]. Additionally, De Graeve et al. [31] have reported that after sputtering by GDOES an oxide layer may be formed in the bottom of the craters which support the passive behaviour of the curves shown in Figure 6.4. The UIDL has the highest average  $E_{BD}$  (0.022 V vs Ag|AgCl|KCl sat.) followed by the surface's average  $E_{BD}$  (0.002 V vs Ag|AgCl|KCl sat.). The FL  $E_{BD}$  values show a variation without a trend as a function of depth.

Figure 6.4 - Anodic potentiodynamic polarisation curves in 0.1 mol·L<sup>-1</sup> NaCl solution acquired by means of electrochemical micro-cell as a function of the depth and also at the surface for as received 22MnB5 steel coated with hot-dip Al-Si (10 % Si in mass fraction)



Source: Author

Table 6.1 - Average  $E^*$ ,  $E_{BD}$ , and their corresponding standard deviations, determined from anodic potentiodynamic polarisation curves in 0.1 mol·L<sup>-1</sup> NaCl at the surface and different depths in the AR sample

AR sample	$E^*$		$E_{BD}$	
	(V vs Ag AgCl KCl sat.)		(V vs Ag AgCl KCl sat.)	
	Average	Standard deviation	Average	Standard deviation
Surface	-0.46	0.02	0.002	0.012
FL_2.5 μm	-0.59	0.03	-0.192	0.054
FL_7.5 μm	-0.62	0.05	-0.364	0.033
FL_12.5 μm	-0.70	0.02	-0.205	0.035
UIDL_17.5 μm	-0.42	0.04	0.022	0.028
Steel substrate <sup>a</sup>	-0.36	0.08	-	-

<sup>a</sup> ferrite/pearlite microstructure

Source: Author

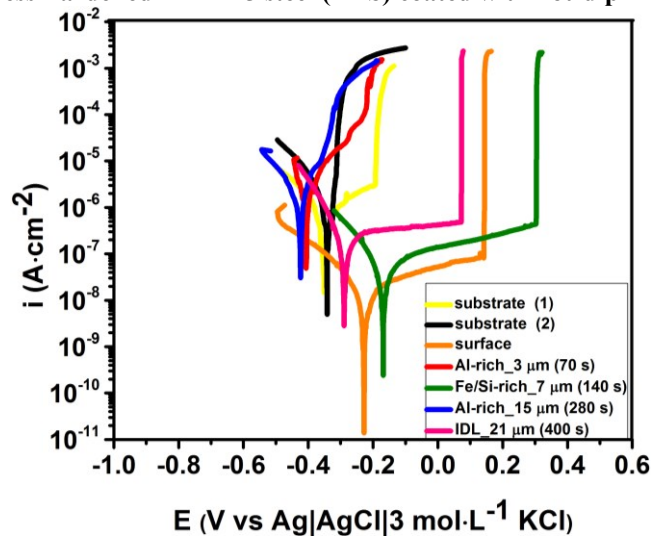
According to Figure 6.4 and Table 6.1, the surface presents higher average  $E^*$  (-0.46 V vs Ag|AgCl|KCl sat.) than the three underlying FL which present low values independent of the depth. The difference between the average corrosion potentials ( $\Delta E^*$ ) of the three curves in the FL is small; the highest  $\Delta E^*$  value is around 0.11 V (FL at 12.5 μm and FL at 2.5 μm). As the less noble layer, the FL layers could provide cathodic protection to its adjacent UIDL; especially the FL at 12.5 μm which presents the lowest value of  $E^*$ . The steel substrate shows the noblest average  $E^*$  (-0.36 V vs Ag|AgCl|KCl sat.). Therefore, the whole coating layer could provide cathodic protection to the steel substrate. However, the average potential difference between the UIDL and the steel substrate is about 0.06 V, indicating a low driving force for the UIDL to behave as a sacrificial anode. This difference increases to 0.34 V if the comparison is made between the steel substrate and the FL at

12.5  $\mu\text{m}$ . From this analysis, it is possible to establish the following galvanic series, considering the average values of  $E^*$ :  $E^*_{\text{FL}_{12.5\mu\text{m}}} < E^*_{\text{FL}_{7.5\mu\text{m}}} \approx E^*_{\text{FL}_{2.5\mu\text{m}}} < E^*_{\text{UIDL}} < E^*_{\text{surface}} < E^*_{\text{steel}}$ .

The qualitative analysis of the current density in the anodic branch ( $i_a$ ) indicates that the surface and the FL displays a lower  $i_a$  than the UIDL and the steel substrate. In particular, the steel substrate shows the highest  $i_a$ , indicating high corrosion susceptibility in  $0.1 \text{ mol}\cdot\text{L}^{-1}$  NaCl solution.

Figure 6.5 displays the most representative curves obtained by means of anodic potentiodynamic polarisation acquired at the surface and in the craters at different coating sublayers and in the steel substrate for the PHS. It is important to mention that, during the measurements, the Al-rich layers and the surface presented both passive and active behaviour. Even the steel substrate showed a small passivity in one of the measurements. On the other hand, the Fe/Si-rich layer and the IDL presented only passive behaviour. The curves of Figure 6.5 were selected among the curves (at least three) obtained for each position. For the Al-rich layer, only curves presenting active behaviour were selected because of the influence of iron enrichment as discussed further. The average values of  $E^*$  and  $E_{BD}$ , as well as their standard deviation values, are summarised in Table 6.2.

**Figure 6.5 - Anodic potentiodynamic polarisation curves in  $0.1 \text{ mol}\cdot\text{L}^{-1}$  NaCl solution acquired by means of electrochemical micro-cell in different positions of coating layer and steel substrate for as press-hardened 22MnB5 steel (PHS) coated with hot-dip Al-Si**



Source: Author

**Table 6.2 - Average  $E^*$ ,  $E_{BD}$ , and their standard deviation values, determined from anodic potentiodynamic polarisation curves in  $0.1 \text{ mol}\cdot\text{L}^{-1}$  NaCl at the surface and different depths in the PHS sample**

PHS sample	$E^*$		$E_{BD}$	
	(V vs Ag AgCl KCl sat.)		(V vs Ag AgCl KCl sat.)	
	Average	Standard deviation	Average	Standard deviation
Surface	-0.30	0.08	0.165	0.334
Al-rich_3 $\mu\text{m}$	-0.40	0.05	0.149	0.120
Fe/Si-rich_7 $\mu\text{m}$	-0.23	0.06	0.270	0.181
Al-rich_15 $\mu\text{m}$	-0.41	0.08	0.104	0.072
IDL_21 $\mu\text{m}$	-0.32	0.03	0.148	0.075
Steel substrate <sup>b</sup>	-0.38	0.07		

<sup>b</sup> martensite microstructure

Source: Author

From Figure 6.5, it can be seen that the hot-stamping process shifts the overall  $E^*$  of the coating layer towards nobler values. Moreover, the  $\Delta E^*$  among the curves is very small. Based on Table 6.2, the average  $E^*$  of the surface increases around 0.16 V after the thermo-mechanical process. The average  $E^*$  values of the Al-rich layers are very similar to each other (-0.40 V and -0.41 V Ag|AgCl|KCl sat.). Furthermore, they are lower than the Fe/Si-rich layer (-0.23 V vs Ag|AgCl|KCl sat.) and very close to the IDL (-0.32 V vs Ag|AgCl|KCl sat.) and the substrate (-0.38 V vs Ag|AgCl|KCl sat.). Therefore, Al-rich sublayers could play the role of sacrificial anode for the Fe/Si-rich layer and the IDL, but not for the substrate. For the steel substrate the Al-rich layers can only protect by forming a barrier. Based on the average values of  $E^*$ , shown in Table 6.2, the following galvanic series is presented:  $E^*_{\text{Al-rich}} < E^*_{\text{steel}} < E^*_{\text{IDL}} < E^*_{\text{surface}} < E^*_{\text{Fe/Si-rich}}$ .

As already mentioned, the polarisation curves obtained from different samples in the Al-rich layers showed both passive and active behaviour. Moreover, the average  $E_{BD}$  of the curves with passive behaviour had a high standard deviation. These results suggest a high heterogeneity of the exposed area on which the curves were obtained. This fact can be ascribed to the lack of the flatness (see Figure 4.5) and of the depth heterogeneity of the Al-rich sublayers. The latter was verified in previous studies [8,19,24].

Comparing Table 6.1 and Table 6.2, it can be verified that after hot stamping there is a shift towards nobler values of all coating sublayers. The Fe/Si-rich layer has the highest average  $E_{BD}$  (0.270 V vs Ag|AgCl|KCl sat.), while the Al-rich layers have an average  $E_{BD}$  in the range from 0.104 V to 0.149 V vs Ag|AgCl|KCl sat.). Based on the average values, the  $E_{BD}$  sequence can be drawn as:  $E_{BD} - \text{Al-rich} \approx E_{BD} - \text{IDL} < E_{BD} - \text{surface} < E_{BD} - \text{Fe/Si-rich}$ . Concerning  $i_a$ , the qualitative analysis shows that the surface and the Fe/Si-rich sublayer

presented the lowest  $i_a$  in the passive range of the polarisation curve. On the other hand, the Al-rich sublayers and the steel substrate have the highest  $i_a$  indicating their high corrosion susceptibility in  $0.1 \text{ mol}\cdot\text{L}^{-1}$  NaCl.

The results indicate that the hot-stamping process has a large influence on the electrochemical behaviour of the Al-Si coating. On the other hand, even though the steel substrate had changed its microstructure from pearlite-ferrite into martensite, due to the thermo-mechanical process, the electrochemical behaviour of the steel in terms of average  $E^*$  and  $i_a$  is not affected by the hot stamping process.

## 6.4 Discussion

### 6.4.1 GDOES as a sample tool preparation

In general, it is possible and relatively simple to correlate the surface of the craters with the different sublayers in the coatings identified by FE-SEM / EDS analyses. However, one of the drawbacks of using GDOES as a sample preparation technique is the difficulty of sputtering the rough interfaces and exposing the entire surface of the thin sublayers [31,50,115]. Consequently, there will be an influence of other phases exposed together with the desired phase on the electrochemical results. This was probably the case for the crater in the UIDL for the AR sample, and the craters in the Al-rich sublayers and in the IDL for the PHS condition. The UIDL (AR) may also experience the influence of the LIDL which is very thin. This was further confirmed by the craters' cross-sections (not shown). However, a clear distinction/trend was obtained in the general electrochemical behaviour of the different sublayers analysed. It is important to highlight that the sputtering of the PHS sample sublayers was more difficult. This is due to the difference in hardness among the phases (sublayers) and the non-uniform morphology of the sublayers [8,24]. Another drawback can be related to the oxide layers on the bottom of the craters. As already mentioned, De Graeve et al. [31] reported that the sputtering may lead the formation of oxide layer on the bottom of the craters. However, a thin oxide layer will always be present, mainly in the Al-rich sublayers, as the sputtering changes the surface characteristics. Therefore, a long interval between the procedure of making the crater by GDOES and carrying out the electrochemical measurements may cause the thickening of the oxide layer on the bottom of the craters.

#### 6.4.2 Local electrochemical measurements

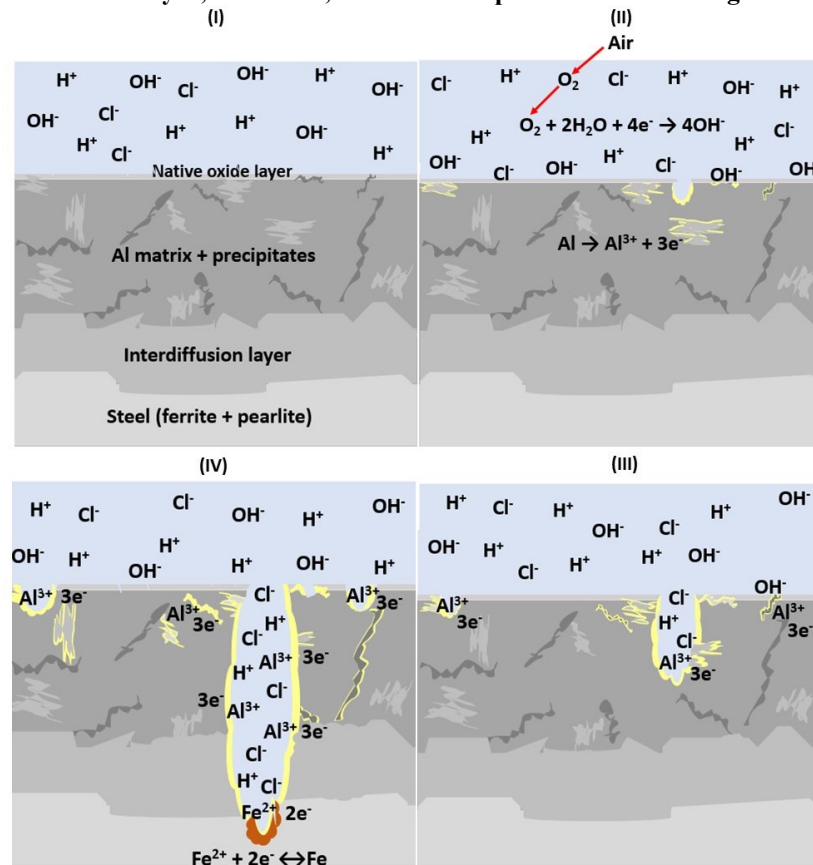
As result shown in Figure 6.4 and Table 6.1, the high average  $E^*$  of the outer surface can be attributed to the native oxide layer which is characteristic of Al-based alloys [114]. This thin oxide layer contributes for the passive behaviour of the surface. If a damage occurs at the surface and exposes the coating, the FL could provide cathodic protection to the UIDL. Moreover, the  $E^*$  seems to decrease as a function of depth in the FL. However, a trend correlating  $E^*$  as a function of depth cannot be established because it is probably more related to the influence of the precipitates, as shown in Figure 4.4 (a). The higher average  $E^*$  of the UIDL in comparison with the FL may be justified by the amount of silicon and iron present in it. However, the steel substrate shows the highest  $E^*$ . This suggests that the steel substrate could be protected by the coating by means of cathodic protection, but, as already mentioned, the driving force (the potential difference) may not be enough for the coating to corrode preferentially instead of the steel. The average  $\Delta E^*$  between the UIDL and the steel substrate is only 0.06 V, but the minimum corrosion potential difference for cathodic protection has been pointed out as 0.05 V [7].

The predominance of the passive behaviour seen in Figure 6.4 may also be related to the thickening of the oxide layer inside the craters made by means of GDOES. Nevertheless, this passive layer may breakdown from a specific potential for each sublayer ( $E_{BD}$ ). The lower  $E_{BD}$  of the FL is related to the presence of precipitates which lead to the formation of a flawed oxide film [31,66]. As the precipitates act as cathodic sites, the surrounding aluminium matrix will start to corrode, promoting localised corrosion [31,68]. This was experimentally confirmed by means of SKPFM technique and immersion tests (Chapter 5). The corrosion morphology of the specimens after immersion in NaCl solution (3.5% in mass fraction) revealed that the attack in the AR samples was characterised by localised corrosion initiated around the precipitates. Conversely, the UIDL shows the higher  $E_{BD}$ , which is related to the homogeneity in terms of layer composition [31], consisting of iron, silicon and aluminium.

The corrosion mechanism of the Al-Si (10 % Si in mass fraction) coating / steel substrate system, before hot stamping, can be summarised as illustrated in Figure 6.6. (I) The native oxide layer at the surface acts as a protective barrier and shows low  $i_a$ . (II) In the case of damages at the native oxide layer the FL is exposed; its corrosion occurs localised around the precipitates. (III) If damage reaches the UIDL, the FL will be corroded preferentially behaving as a sacrificial anode to the UIDL as it presents the lowest average

$E^*$ . Moreover, the FL does have an  $i_a$  as low as the top oxide layer, which means that, despite it corrodes at low potential, its corrosion rate is also low. As long as the steel substrate is not exposed, the UIDL will protect the steel substrate by means of a barrier mechanism and not by cathodic protection because of the small potential difference among them. (IV) In case of steel exposure by severe damages in the coating, the steel substrate would corrode similar the UIDL (in terms of corrosion potential) with a high corrosion rate due to its highest  $i_a$  indicating the high corrosion susceptibility of the steel substrate in this media ( $0.1 \text{ mol. L}^{-1} \text{ NaCl}$ ). As the UIDL shows an  $i_a$  higher than the FL and the surface, it can be suggested that the corrosion rate of the sublayers seems to be closely related to the amount of iron in them.

**Figure 6.6 - Schematic diagram of the proposed corrosion mechanism for 22MnB5 steel coated with hot-dip Al-Si (Si 10 % in mass fraction) showing: (I) initial condition of the system, absent of defects at the surface, in which the native oxide layer acts as a protective barrier; (II) damage at the surface and the beginning of the corrosion process of the coating matrix (free layer) localised around the precipitates; (III) damage reaches the interdiffusion layer and the coating matrix plays a role of sacrificial anode, corroding preferentially; (IV) the steel substrate is exposed and it corrodes similarly to the interdiffusion layer; moreover, the corrosion process of the coating matrix enhances**



Source: Author

### 6.4.3 Influence of hot stamping on the electrochemical depth profile

Comparing the results from Figure 6.4 and Figure 6.5, the evaluation of the influence of the hot-stamping process on the corrosion mechanism is possible. The first highlight is regarding the overall shift of  $E^*$  and  $E_{BD}$  towards nobler values. These results are in agreement with the SKPFM results (Figure 5.3 and Figure 5.5) presented in Chapter 5. An increase in the Volta potential of the coating layer was seen after hot stamping, as well as a minimal potential difference among the sublayers and a decrease in driving force for cathodic protection. However, in the SKPFM results both the Fe/Si-rich sublayer and the IDL presented Volta potential smaller than the steel substrate whereas in the electrochemical micro-cell measurements they presented a different trend. In the electrochemical micro-cell results both Fe/Si-rich sublayer and the IDL are nobler than the steel substrate. The reason may be attributed to the influence of the Al-rich phase (the most abundant phase in the coating's cross section) on the measured Volta potential of the other sublayers seen in the cross section (much thinner than the Al-rich sublayers). The size effect of intermetallics on the measured Volta potential has been shown in previous studies [111,112]. On the other hand, the electrochemical micro-cell measurements were performed from the top surface, where a specific area of the sample containing mainly the phases corresponding to the analysed sublayer was isolated and evaluated. The two local electrochemical techniques present different principles but they bring complementary information about the electrochemical behaviour of the system. Furthermore, the present investigation has indicated a similar trend among the coating's sublayers.

During hot stamping, iron diffuses from the steel substrate towards the coating. Thus, the whole coating layer becomes enriched in iron, and the coating presents a multi-layered structure. Even the surface becomes enriched in iron as shown the surface EDS analyses (Figure 4.3) in agreement with previous studies [7,11]. The presence of iron and silicon in the top surface can be the reason for the increase of the surface's  $E^*$ . Moreover, the oxide layer formed after hot stamping (thermal oxides) may be thicker than the native aluminium oxide layer, enhancing the passive behaviour and being the probable reason for a higher  $E_{BD}$ . As the average  $E^*$  of the surface (oxide layer) is higher than that of the Al-rich phases, the possible protection mechanism is only by barrier protection. Among all the sublayers in the coating, the Al-rich phases presented similar average  $E^*$  as the steel substrate (around -0.40 V vs Ag|AgCl|KCl sat.). This could be due to the high amount of iron found in these layers after hot stamping. These layers could provide some cathodic

protection to the Fe/Si-rich layer, but there is just a small driving force for that (only 0.16 V). The Fe/Si-rich layer presents the noblest average  $E^*$  (-0.23 V vs Ag|AgCl|KCl sat.), though, it is only 0.09 V higher than the IDL.

The reason for the shift towards nobler potential values could be related to the silicon influence. According to the depth profile presented in Figure 6.3, the silicon content is relatively higher in the Fe/Si-rich layer than in the IDL. The presence of silicon might be also the reason for the highest  $E_{BD}$  of the Fe/Si-rich layer. As the precipitates are no longer seen in the PHS condition, the overall  $E_{BD}$  shifted towards more positive values for those curves presenting a passive behaviour. Previous studies have found that the addition of silicon in steel leads to the decrease of iron oxidation rate at high temperatures [116]. This mechanism is related to the formation of a silicon oxide at the surface which inhibits the diffusion of iron throughout the surface, consequently avoiding its oxidation [116]. This effect could be related to the passivation of the sublayers presenting a high silicon content in PHS (Fe/Si-rich layers). However, further and dedicated research is necessary in order to fully understand the effect of Si in the passivity of these Fe-Si-(Al) intermetallic phases.

The hot stamping changes the electrochemical behaviour of the coating layer but does not change the electrochemical behaviour of the steel substrate even considering the microstructure transformation from pearlite-ferrite to martensite. Although one of the curves regarding the steel substrate for PHS sample shows a small passivity range, this behaviour is not a trend. However, it is an important observation since this is mostly related to the thickening of the oxide layer on the bottom of the crater. During the SKPFM measurements it was noticed that the Volta potential of the steel substrate is slightly shifted to nobler values after hot stamping (see Figure 5.7). It was attributed to the martensite transformation as it results in residual stress on the material and, therefore, changes on the Volta potential as it is very sensitive to any change in the sample surface [90]. As already reported, the effect of phase transformation on the steel substrate should be more pronounced in terms of Volta-potential difference than any other potential measured by means of conventional electrochemical techniques.

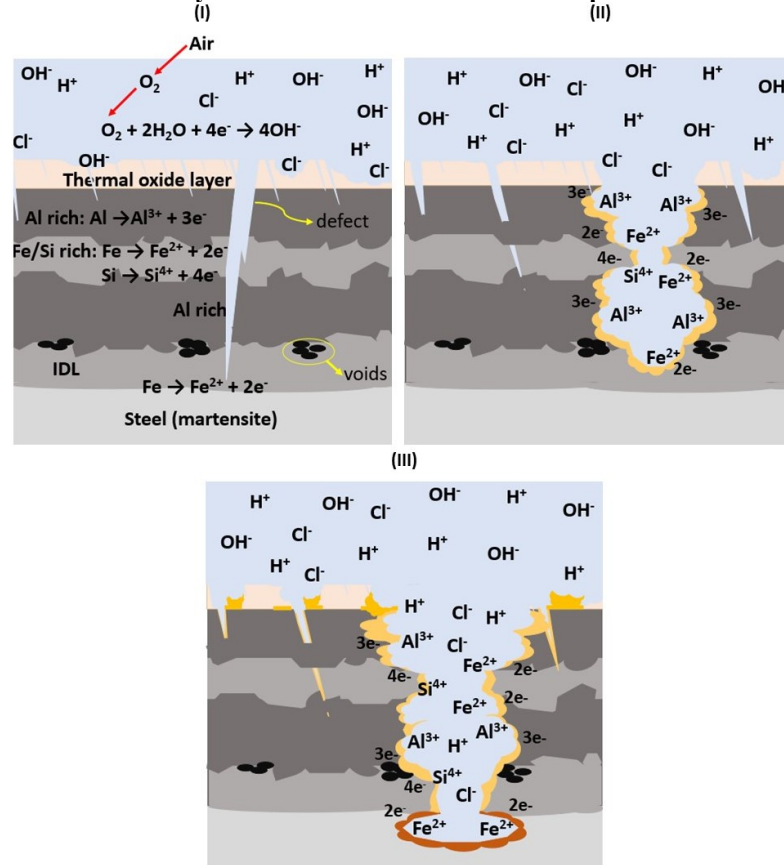
As already mentioned, during the micro-cell measurements, the Al-rich layers and the surface presented both passive and active behaviour. The probable reason for the active behaviour of the Al-rich phases could be the iron enrichment which is around 45 % (in mass fraction), as seen in Figure 4.5 (b) spots 1 and 3. The iron enrichment can also be the reason why the Al-rich layers presented the highest  $i_a$ , similar to the steel substrate. Conversely, for the curves showing passive behaviour during the measurements, it could be

because of the thickening of oxides on the bottom of the craters in the Al-rich sublayers, due to the different intervals between making the crater by GDOES and carrying out the electrochemical measurements. Another hypothesis for the active behaviour of the Al-rich phases as well as the surface could be the presence of micro cracks. On the contrary, during the micro-cell measurements, the acquired curves for the IDL and the Fe/Si-rich layer showed only passive behaviour. Despite the open discussion about the most appropriate stoichiometry for each sublayer in PHS coated with Al-Si, there is a consensus that the Al-rich layers are harder and brittle whereas the Fe/Si-rich layers and the IDL are more ductile [24,60,117]. This may contribute to the density of cracks as well as their formation and propagation. Fan et al. [24] have shown that the cracks initiate from the surface and they are limited at the IDL. The authors have pointed out two reasons for the formation and propagation of cracks: the thermal expansion and the difference on mechanical properties between the sublayers. Furthermore, the predominant passive behaviour and the enhancement of the  $E_{BD}$  of the Fe/Si-rich layer and the IDL could be attributed to the presence of silicon, as already discussed.

Concerning the  $i_a$  either for AR and PHS samples, they show low order of magnitude from  $10^{-8} \text{ A}\cdot\text{cm}^{-2}$  to  $10^{-6} \text{ A}\cdot\text{cm}^{-2}$ . These are expected current density ranges for curves presenting a passive behaviour. However, for those curves where the active behaviour is predominant, a higher order of magnitude would be expected, such as  $10^{-5} \text{ A}\cdot\text{cm}^{-2}$ . The latter corresponds to the limiting current density of the oxygen which determines the Fe and also Al corrosion rate in aerated solution [118]. Thus, the relatively low order of magnitude of  $i_a$  for those curves presenting active behaviour ( $10^{-6} \text{ A}\cdot\text{cm}^{-2}$ ) could be another indication of the influence of the oxide layer on the bottom of the craters.

From the results presented, the following protection mechanism for coated PHS, considering the  $0.1 \text{ mol}\cdot\text{L}^{-1}$  NaCl as an electrolyte is proposed in Figure 6.7. (I) Damages (cracks) are already seen from the surface throughout the whole coating layer. The surface consists of a thermal oxide layer thicker than the native oxide layer from the AR condition. (II) The presence of damages enhances the corrosion process: the oxide layer at the surface acts as a protective barrier to the Al-rich layer; the surface will corrode at relatively high potentials, exhibiting low  $i_a$ . The Al-rich layer, independent of the depth, could play the role of sacrificial anode for the Fe/Si-rich and / or the IDL, corroding preferentially and exhibiting high corrosion rates. Finally, the steel substrate will be protected by only barrier mechanism. (III) In case of severe damage and the exposure of the steel substrate, the latter will corrode as much as the Al-rich layers due to their similar  $E^*$  and  $i_a$ .

**Figure 6.7 - Schematic diagram showing the proposed corrosion mechanism for press-hardened 22MnB5 steel coated with hot-dip Al-Si from: (I) initial condition of the system which already shows several damages at the surface and in the coating layer; (II) as the oxide layer plays a role of protective barrier, the coating sublayers start to corrode, but the corrosion of the Al-rich sublayers is more pronounced as they could behave as sacrificial anode to the Fe/Si-rich layer and the IDL; (III) the coating layer provides a barrier protection to the steel substrate; when it is exposed it corrodes as much as the Al-rich sublayers due to their similar corrosion potential and corrosion rate**



Source: Author

#### 6.4.4 Influence of the electrolyte concentration on the electrochemical behaviour of the system before and after hot stamping

In this thesis, the electrochemical behaviour of the systems (either before or after hot stamping) has been characterised in different media. In Chapter 5, the global electrochemical measurements were carried out in a high chloride content electrolyte (5 % NaCl in mass fraction, which is approximately  $0.7 \text{ mol}\cdot\text{L}^{-1}\cdot\text{NaCl}$ ). Conversely, in the same chapter the electrochemical behaviour was evaluated in the absence of an electrolyte by SKPFM. On the other hand, in this Chapter 6 a less concentrated electrolyte was used in the local potentiodynamic measurements ( $0.1 \text{ mol}\cdot\text{L}^{-1}\cdot\text{NaCl}$ ). Usually, local electrochemical measurements require less concentrated electrolyte to improve the resolution [119,120].

In Chapter 5, the differences between global electrochemical measurements and SKPFM were discussed. Nevertheless, at this point is worth to compare the effect of the electrolyte concentration on the electrochemical behaviour of the systems. The results presented in Figure 5.1 (b) can only be compared with the results of the surface and the steel substrate in Figure 6.4, and the result of the surface in Figure 6.5. The first highlight is related to the electrochemical behaviour. In high chloride medium, all conditions presented an active behaviour. On the other hand, in a less concentrated electrolyte the samples' surface showed a predominant passive behaviour, while the steel substrate kept its predominant active behaviour independent of the chloride content. As already discussed, in high chloride media (marine environments) the passive behaviour at the top surface is lost by the action of the chloride ions, as they cause the breakdown of the passive layer [25]. Therefore, the systems become active. This may also justify the reason why the corrosion potentials are higher and the current densities in the anodic branch are lower in a less concentrate electrolyte. Conversely, for the steel substrate the only effect of different chloride content was in terms of corrosion potential. The higher the chloride concentration in the electrolyte the lower the corrosion potential of the steel. The reason can probably be correlated with the different methodologies employed, and the critical aspects of the electrochemical micro cell shall be considered [81]. In addition to the possible thickening of oxides on the bottom of the craters made by GDOES, as already discussed, according to Andreatta et al. [81] "local measurements carried out with the electrochemical micro-cell often exhibit different behaviour than conventional large-scale measurements carried out on the same material (...) this should be considered as an intrinsic characteristic of the method".

## 6.5 Conclusion

The effect of the hot-stamping process on the electrochemical behaviour was systematically evaluated using a depth profiling approach combining GDOES and an electrochemical micro cell. The main findings are summarised as follows:

- i. The iron enrichment was the reason for the overall increase of corrosion potential of the coating layer.
- ii. The increased potential of the surface was attributed to the formation of an oxide layer (thermal oxides), thicker than the native aluminium oxide layer, probably containing also silicon and iron oxides.

- iii. Silicon precipitates are no longer seen after hot stamping. The presence of silicon in solid solution was attributed as the reason for the predominant passive behaviour of the Fe/Si-rich layer and the IDL. Moreover, the high silicon content in the Fe/Si-rich layer has been indicated as the reason for its highest corrosion and breakdown potential.
- iv. The predominant active behaviour of the Al-rich layers was mainly related to the iron enrichment. The presence of micro cracks may also affect the electrochemical behaviour of both the Al-rich phases and the surface.
- v. The hot-stamping process did not change the electrochemical behaviour of the steel substrate. However, it altered the electrochemical behaviour of the coating layer, which becomes nobler. Thus, after hot stamping the steel can be protected only by barrier protection.

## **CHAPTER 7 - Salt spray test and analysis of corrosion products by means of Raman spectroscopy for 22MnB5 steel coated with hot-dip Al-Si: the effect of hot stamping <sup>5</sup>**

### **7.1 Introduction**

The electrochemical measurements, both global and local, indicate that the thermo-mechanical process causes an ennoblement of the system (coating/steel). However, it is not a straight relation with the corrosion resistance of the material; the latter is mostly influenced by the kinetics parameters (rates). Furthermore, the presence of micro cracks and voids, formed during the thermo-mechanical process, can also play an important role on the corrosion resistance of the system (coating/steel). Additionally, the way that the corrosion starts and propagates shall be analysed in order to control both. De Faria et al. [121] have highlighted the importance of the knowledge about the rust formation mechanism in corrosion control. The accelerated tests can provide insights about the nature of the corrosion products formed under severe environments, for instance, in high chloride media as Dosdat et al. and Allély et al. have shown [7,11]. Among the different accelerated tests, the continuous salt spray test (SST), according to the ASTM B 117, is still used as a quality control [77].

As the Al-Si coating has already been established as a widely applied metallic coating for hot-stamped components, this chapter aims at evaluating the effect of the thermo-mechanical process on the corrosion damage of the system exposing it to the continuous salt spray test. This test was chosen in order to enhance the formation of corrosion products for a better analysis of their composition. The nature of the corrosion products formed under SST conditions in the samples either before or after hot stamping were analysed by means of Raman spectroscopy, in order to elucidate the possible corrosion mechanism.

---

<sup>5</sup> This chapter was peer reviewed in a submission to **Surface & Coatings Technology** and it will be resubmitted further either to the same journal or to another one.

## 7.2 Experimental procedure

### 7.2.1 Continuous salt spray test

AR and PHS samples were submitted to a continuous salt spray test (SST), according to the ASTM B 117 standard, for three weeks. The test conditions consist of a continuous 5.0 % NaCl spray solution (% in mass fraction) at 35 °C and pH from 6.5 to 7.2 [122].

### 7.2.2 Raman spectroscopy

The corrosion products present at the sample surfaces after the SST were characterised by Raman spectroscopy. There was an interval of 24 h to 48 h between taking out the sample from the SST chamber and analysing it by Raman spectroscopy. Several regions at the surface were analysed using a green laser ( $\lambda = 532$  nm). The laser intensity was about 1 mW, though, for some measurements, only 0.1 mW was used in order to avoid thermal decomposition of the compounds [121]. After Raman analysis, the samples' cross sections were characterised following the same procedure presented in Chapter 4, section 4.2.

## 7.3 Results

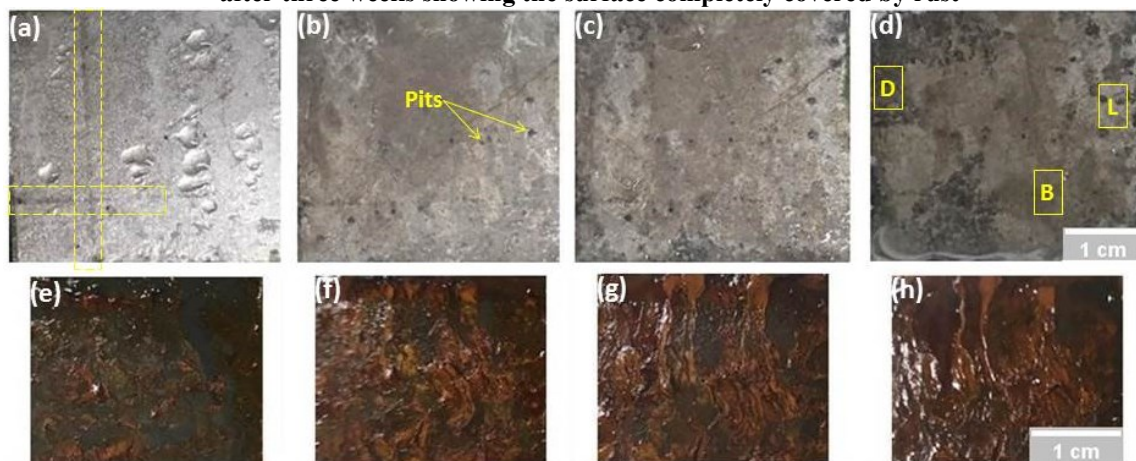
### 7.3.1 Macroscopic characterisation of corroded samples' surface after SST

Figure 7.1 shows corroded samples' surfaces for both conditions, AR and PHS, after the SST. For the AR surface, after one day of test, it is seen that the corrosive attack started in scratched areas highlighted in Figure 7.1 (a). These scratches were probably originated from transportation and storage of the blanks. They play a role of preferential sites for corrosion attack, as the superficial energy at these sites is different from the overall sample surface. After one week, a larger area was attacked; the surface showed different shades of grey and white lines (Figure 7.1 (b)). The white lines are probably due to saline deposits from the salt spray, and the different shades of grey may be related to the formation of aluminium-based corrosion products. It is important to notice that, after one week, it is already possible to identify the presence of pits at the surface. From the first until the third week, the corrosive attack intensifies; the number of pits increased and, at the end, the surface has dark (D) and light (L) grey areas and a large brownish (B) area, as highlighted in Figure 7.1 (d), further analysed by means of Raman spectroscopy. The brownish area indicates the presence of

iron-based compounds [123–125] which could be either from the interdiffusion layer of the coating or from the steel substrate.

Concerning the PHS samples (Figure 7.1 (e-h)), the main highlight is the presence of an irregular rust layer at the surface after one day under SST conditions. By increasing the time of exposure to SST conditions, the whole samples' surface was covered by a reddish-brownish rust layer. The presence of rust at the surface often indicates corrosion of the steel substrate. However, in the case of PHS, it is important to point out that the top layer is enriched in iron, due to the diffusion which takes place during hot stamping, as discussed in Chapter 4. Therefore, the reddish-brownish colour may be related to either the iron enriched phases or the corrosion of the substrate. To evaluate the severity of the attack and whether it had reached the steel substrate, cross-section analyses were carried out.

**Figure 7.1 - Surface of samples under SST conditions: (a) AR after one day, highlighting the initial scratches; (b) AR after one week, showing pits; (c) AR after two weeks; (d) AR after three weeks, pointing out dark (D), light (L) grey and brown (B) areas; (e) PHS after one day showing the growth of reddish-brownish rust at the sample surface; (f) PHS after one week; (g) PHS after two weeks; (h) PHS after three weeks showing the surface completely covered by rust**



Source: Author

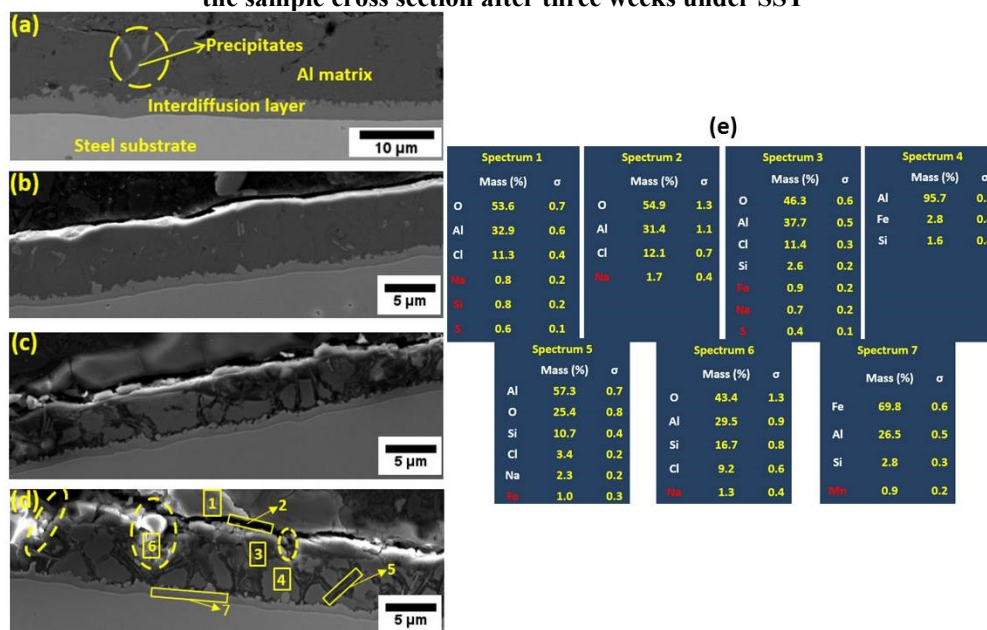
### 7.3.2 Cross-section characterisation

The cross sections of AR samples submitted to the SST are shown in Figure 7.2. The initial condition shown in Figure 7.2 (a) is very similar to that present in Figure 4.4; it consists of an Al matrix with cathodic precipitates in it and an interdiffusion layer. Moreover, Figure 7.2 (b-d) presents the progress of the coating corrosion as a function of exposure time (in weeks) under SST conditions.

From Figure 7.2, after one week (Figure 7.2 (b)) in the SST, the formation of a brighter layer at the top surface is seen, probably related to the oxide layer. This layer

provides a barrier protection to the whole system (coating/steel) as indicated by the electrochemical micro-cell results (Figure 6.4). The whole coating layer and the steel substrate are well preserved. However, from the second week (Figure 7.2 (c)), the aluminium coating matrix is attacked; from this is suggested that the breakdown of the oxide layer has occurred due to the high chloride content, and that the barrier protection is no longer provided, resulting in the corrosion of the underlying aluminium coating matrix. It is seen that the attack occurs preferentially in a localised way, as indicated in the immersion test (Figure 5.2). It is important to notice that the interdiffusion layer remains well preserved even after the third week under SST conditions, as shown in Figure 7.2 (d). In Figure 7.2 (d), regions with a probable pitting corrosion are highlighted by dashed circles. The visual inspection of the samples' surface (Figure 7.1 (b-d)) showed that those pits were present since the first week under SST conditions. Moreover, Figure 7.2 (e) shows the EDS results corresponding to Figure 7.2 (d). Spots 1 and 2 show that aluminium oxide is presented at the top surface of the sample, while spot 3 shows the corrosion of the aluminium matrix which started around the precipitates, as shown in spot 5.

**Figure 7.2 - SEM secondary electron images for the cross sections of AR samples as: (a) initial condition; (b) one week after SST; (c) two weeks after SST; (d) three weeks after SST showing the probable areas of pitting corrosion by means of dashed circles; (e) semi-quantitative EDS analyses of the sample cross section after three weeks under SST**



Source: Author

Figure 7.3 shows the results of the effect of the hot-stamping process on the Al-Si coating structure, as well as the effect of the SST on the PHS samples in terms of corrosion

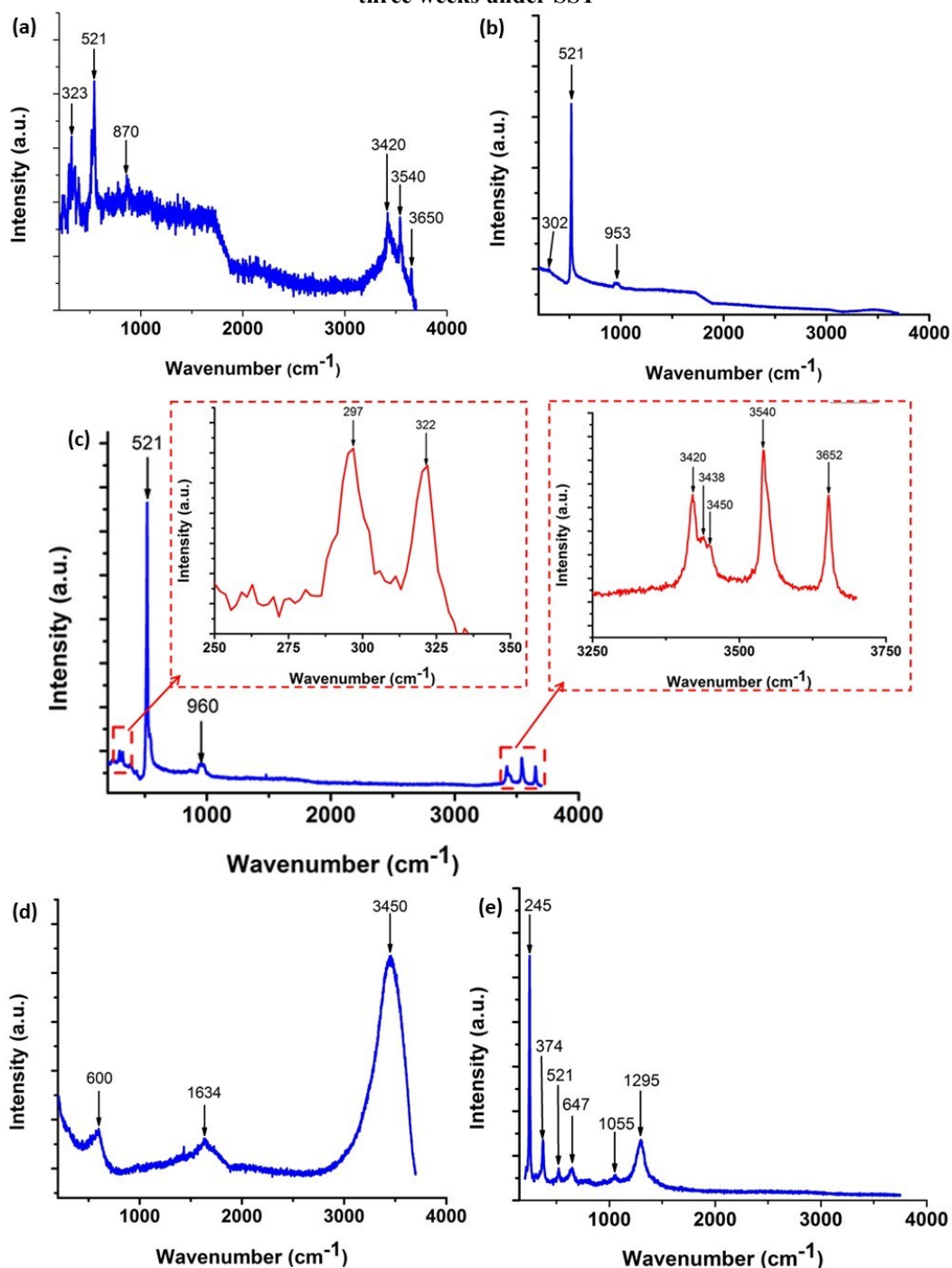


SST (Figure 7.3 (d)) shows the attack of the coating and steel substrate, and the formation of oxides in the attacked region, characterised by the bright areas with nodular morphology. This is better seen in Figure 7.3 (e), which is a magnified image of the region highlighted by a rectangle in Figure 7.3 (d). Figure 7.3 (f) shows the EDS results of different regions from Figure 7.3 (e). Spot 1 corresponds to a mixture of oxides inside the cavity which are enriched in aluminium, iron and silicon. Spot 2 also shows the formation of a mixture of oxides composed of iron and aluminium. This suggests that the corrosion started in the Al-rich phase reaching the Fe/Si-rich phase. Spot 3 presents the attack of the steel substrate and, probably, the beginning of oxide formation, mostly indicated by the bright contrast. Finally, spot 4 shows the predominance of iron oxide towards the top surface. These results indicate that the corrosion process, regarding PHS samples, is mainly influenced by the initial defects and whether they reach the steel substrate, because the coating layer acts mostly as a protective barrier to the substrate.

### 7.3.3 Raman spectroscopy

For both conditions, AR and PHS, the oxide layer formed at the top surface during SST plays a role of extra protective barrier. The nature of these oxides was characterised by Raman spectroscopy. In Figure 7.4 is shown the Raman spectra acquired on different positions in the AR samples after the SST. Spectra (a-d) were seen on all the samples analysed. The peaks show predominance at both low and high wavenumbers; high wavenumbers are characterised by the stretching bands of OH [126]. In Figure 7.4 (a) a mixture of compounds is presented; the highest and sharpest peak could be attributed to silicon presenting its most intense peak at  $521\text{ cm}^{-1}$  [127] and, at high wavenumbers, bayerite ( $\alpha\text{-Al(OH)}_3$ ) is clearly present due to its characteristic peaks around  $3420\text{ cm}^{-1}$ ,  $3540\text{ cm}^{-1}$  and  $3650\text{ cm}^{-1}$  [126,128,129]. The results presented in Figure 7.4 (c) confirms the presence of bayerite by means of a magnification at the low and high wavenumbers. According to the literature, the most intense peaks at low wavenumbers are at  $297\text{ cm}^{-1}$  and  $322\text{ cm}^{-1}$  and, at high wavenumbers, are at  $3420\text{ cm}^{-1}$ ,  $3438\text{ cm}^{-1}$ ,  $3450\text{ cm}^{-1}$  (shoulder),  $3542\text{ cm}^{-1}$  and  $3652\text{ cm}^{-1}$  [128]. In addition to this, the results displayed Figure 7.4 (b) confirm the presence of silicon, since this spectrum was obtained in an area where precipitates were present with the most intense peak at  $521\text{ cm}^{-1}$  [127]. The spectrum shown in Figure 7.4 (d) is probably related with a mixture aluminium hydroxide presenting an amorphous structure [126].

Figure 7.4 - Raman spectra of the corrosion products formed at the surface of AR sample after SST; (a) mixture of silicon and bayerite; (b) silicon; (c) mixture of silicon and bayerite showing its most characteristic peaks magnified; (d) amorphous hydroxides mixture; (e) lepidocrocite found only after three weeks under SST

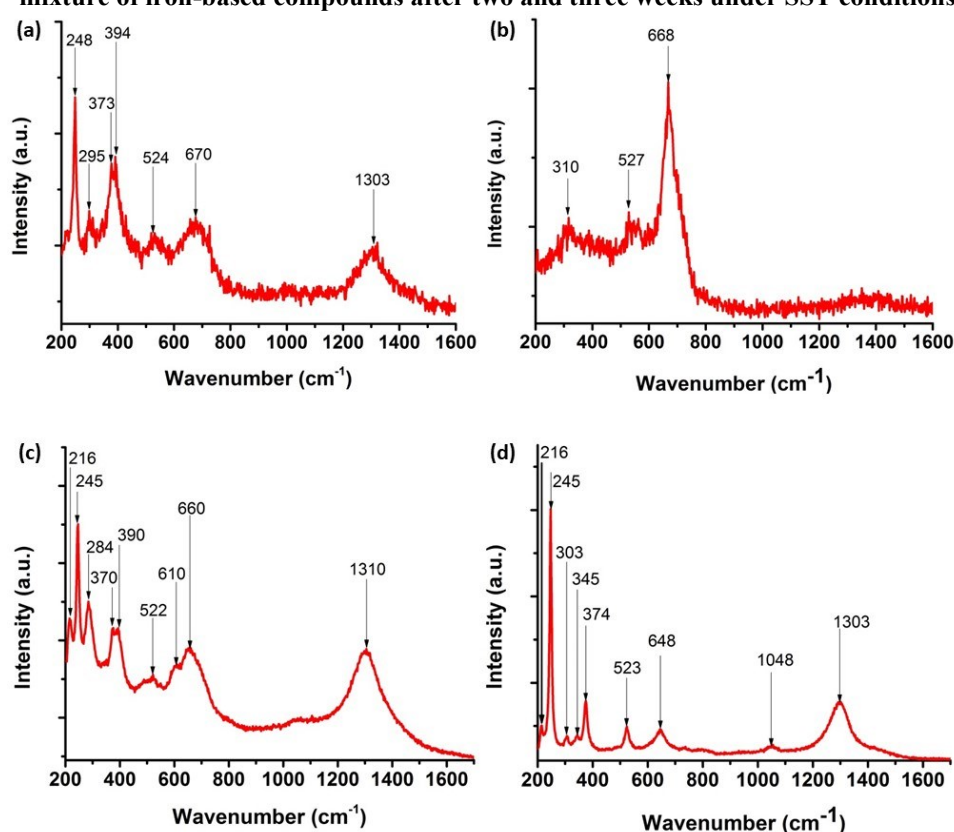


Source: Author

After 3 weeks under SST conditions, a different Raman spectrum was obtained, as shown in Figure 7.4 (e). It shows predominant peaks at low wavenumbers, a characteristic observed for iron-based compounds analysed by Raman spectroscopy [121,123,130]; the surface image obtained by means of confocal microscope (not presented) showed the

presence of brownish spots at the sample surface, indicating the possible exposition of the steel substrate due to the localised attack from the surface. The spectrum corresponding to Figure 7.4 (e) can be considered as lepidocrocite ( $\gamma$ -FeOOH) due to the presence of its characteristic peaks at  $245\text{ cm}^{-1}$  (most intense),  $373\text{ cm}^{-1}$ ,  $522\text{ cm}^{-1}$  and  $650\text{ cm}^{-1}$  [121]. In this case, the peak at  $521\text{ cm}^{-1}$  could be an overlapping of lepidocrocite and silicon, as silicon oxide was identified in all other spectra for AR samples. The presence of iron-based compounds is expected mostly for the PHS sample condition as of the first week under SST due to the high iron content in the coating layer. Figure 7.5 shows the results of Raman measurements for PHS.

**Figure 7.5 - Raman spectra of the corrosion products formed at the surface of PHS sample after SST; (a) mixture of iron-based compounds after one week under SST; (b) presence of magnetite after one week under SST; (c) mixture of iron-based compounds after two weeks under SST conditions; (d) mixture of iron-based compounds after two and three weeks under SST conditions**



Source: Author

From Figure 7.5, the spectrum (a) represents the mixture of iron-based compounds and the spectrum (b) shows the spectrum of magnetite and its most intense peak around  $670\text{ cm}^{-1}$  [130,131]. Both spectra were found only in the sample analysed after one week under SST conditions. Additionally, they present lower and noisier signal in

comparison with other spectra. This can be correlated to the presence of amorphous phases which lead to broader peaks as well. After two weeks, the corresponding spectra are (c) and (d) in Figure 7.5. Only the spectrum (d) shown in Figure 7.5 was identified in the sample after three weeks under SST conditions. All the spectra, except for spectrum (b), show a mixture of iron-based oxides and hydroxide including: hematite ( $\alpha$ -Fe<sub>2</sub>O<sub>3</sub>), magnetite (Fe<sub>3</sub>O<sub>4</sub>), goethite ( $\alpha$ -FeOOH), lepidocrocite ( $\gamma$ -FeOOH) and akaganeite ( $\beta$ -FeOOH). Figure 7.5 (b).

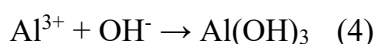
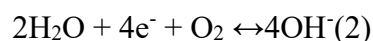
The shapes of the peaks as well as their intensities are related to the order of crystallinity [121]. Magnetite, goethite and lepidocrocite are related to aqueous corrosion [123], whereas akaganeite has been identified as a corrosion product in chloride media [125,132]. The presence of hematite is most related to the laser intensity effect, as it has been pointed out as the thermal product of magnetite decomposition [121,125]. When a lower laser intensity was used, hematite was not found.

Allély et al. [7] have studied the corrosion products formed on PHS coated with Al-Si after accelerated corrosion tests. They have suggested the presence of cristobalite (SiO<sub>2</sub>) and alumina (Al<sub>2</sub>O<sub>3</sub>) formed after cyclic test, identified by X-ray diffraction; moreover, a mixture of aluminium, iron and silicon oxides formed after continuous salt spray test. This statement reinforces the possibility that those peaks around 520 cm<sup>-1</sup> ( $\pm 3$ ) can also be related to the presence of silicon, similar those found in the AR condition. Moreover, aluminium-based compounds were not identified by means of Raman spectroscopy at the PHS surface. However, according to the EDS analyses (Figure 7.3 (f) - spectrum 1), the aluminium-based compounds are formed in the cross-section cavity.

## 7.4 Discussion

Aluminium and aluminium-based coatings show a passive behaviour in different environments with a low concentration of chloride ions [25]. However, in atmospheres with high concentrations of chloride ions these coatings become active due to the breakdown of the passive layer [25]. The presence of pits at the AR sample surface after SST is in agreement with the extensive literature which has investigated corrosion of aluminium-based alloys [66,67,113,114]. The precipitates present in the Al-Si coating matrix behave as cathodes versus the aluminium matrix as shown by the SKPFM results (Figure 5.3). As indicated previously by the immersion test (Figure 5.2 (b)), the corrosion process of the

aluminium matrix starts locally around these precipitates, as shown in Figure 7.2 (d-e). Simultaneously, several reactions may take place during the SST such as the oxidation of the aluminium matrix (1), oxygen reduction (2), acidification inside the pits (3) and the formation of aluminium hydroxide (4) [133]:



According to the Raman spectra, the aluminium hydroxide was characterised as bayerite ( $\alpha\text{-Al}(\text{OH})_3$ ), rarely found in nature [128,134]. Bayerite is one of the polymorphs of  $\text{Al}(\text{OH})_3$ , the other compounds are gibbsite ( $\gamma\text{-Al}(\text{OH})_3$ ) and nordstrandite ( $\text{Al}(\text{OH})_3$ ) [129,134]. Boehmite ( $\gamma\text{-AlOOH}$ ) and diaspore ( $\alpha\text{-AlOOH}$ ) are oxyhydroxides found in laterites and bauxite reserves. Gibbsite is often found in combination with the two oxyhydroxides [128]. Among the different polymorphs, bayerite is easily synthesised in solutions with pH above 5.8 [134]. Schoen et al. [134] also showed that nordstrandite is the product of bayerite transformation at intermediate to high pH values, and gibbsite may be formed at the same time as bayerite at intermediate pH, but prolonged aging promotes the growth of bayerite. Additionally, iron-based corrosion product was found after three weeks under SST which, according to Raman analysis, was identified as lepidocrocite. The presence of iron-based corrosion products can be related to the attack of the steel substrate. Due to the acidification inside the pits, it may increase their depth reaching the steel substrate. This could, however, not be confirmed as the cross-section images (see Figure 7.2) did not show pits reaching either the interdiffusion layer or the steel substrate.

The local electrochemical measurements (SKPFM and micro cell) shows that the aluminium coating matrix (free layer) is the less noble phase of the system (coating/steel). This corroborates to the preferential attack of the aluminium matrix and the high corrosion resistance of the interdiffusion layer. However, occasional local pits penetrating through the interface may still happen in the present severe exposure test. Therefore, a longer exposure time is suggested.

The corrosion process of the AR sample under SST conditions can be summarised as follows: the AR sample consists of a passive oxide layer which is broken down due to the high concentration of chloride ions. Moreover, due to the presence of

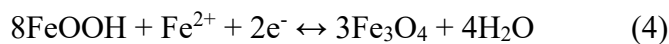
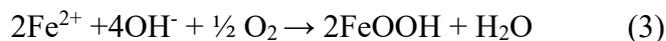
cathodic precipitates at the surface, they act as oxygen reduction sites promoting the corrosion of the aluminium matrix at their surroundings. Due to the simultaneous reactions taking place, bayerite is formed as a corrosion product and HCl promotes the acidification inside the pits; it is very probably that the depth of the pits may increase, reaching the steel substrate. As soon as the steel substrate is reached, it will corrode.

The hot-stamping process has an influence on the Al-Si coating morphology as well as on its corrosion mechanism. It is mostly related to the high iron content present in the coating layer, even in the top surface as suggested by the EDS results from the surface characterisation (see Figure 4.3). This supports the observed presence of brownish-reddish rust at the PHS sample surface in the early stages, as seen in Figure 7.1 (e). Dosdat et al. [11] have shown that the red rust on the PHS's surface in a short time is not related to the exposure of the steel substrate. It is a consequence of the high amount of iron present in the coating after hot stamping. However, as the SEM results highlighted, the PHS samples presented a poor corrosion resistance, under SST conditions, showing the concomitant attack of the coating layer and the steel substrate. The results displayed in Figure 7.3 suggests that in the early stages under SST conditions might enhance the growth of the initial oxide layer, resulting in a thick oxide layer, as seen in Figure 7.3 (b). However, the presence of defects, inherent to the thermo-mechanical process, combined with the severe conditions of the SST support the explanation of poor corrosion resistance of the PHS sample. That is why, the correlation with previous studies and other techniques when accelerated tests are evaluated is of paramount importance. In this scope we will try to position the various insights from the different corrosion test versus each other to come to a more general understanding.

The electrochemical measurements, presented in the previous chapters, have shown that the hot-stamping process shifts the corrosion potential, as well as the Volta potential, to nobler values. This decreases the potential difference between the coating layer and the steel substrate which diminishes the driving force for cathodic protection. Moreover, a small potential difference among the sublayers, which comprises the coating layer after hot stamping, was noticed. The local electrochemical measurements indicate that the Al-rich sublayers are more susceptible to the corrosive attack than the Fe/Si-rich sublayers. The former are less noble and they show high current densities in the anodic branch. Moreover, if the steel substrate is exposed, it corrodes as much as the Al-rich sublayers.

The ennoblement of PHS has also been attributed to the thermal oxide layer presented at the top surface. The EDS results suggest the presence of a mixture of oxides in agreement with the findings of Allély et al [7]. Under continuous SST conditions, the

corrosion products have been characterised as a mixture of aluminium, iron and silicon oxides which present lower crystallinity [7]. In the present investigation, the corrosion products at the samples surface were identified by Raman spectroscopy. The predominance of iron-based compounds was confirmed. The formation of iron-based corrosion products can be easily correlated with the salt drop experiment carried out by Evans cited by Fujita et al. [80]. By adding droplets of 3.5 % NaCl solution (% in mass fraction) above the iron surface, Evans observed the following reactions: (1) iron oxidation, (2) oxygen reduction, (3 and 4) formation of brownish-reddish corrosion product consisting of FeOOH and Fe<sub>3</sub>O<sub>4</sub> [29].



The iron oxyhydroxide (FeOOH) presents different structural arrangements:  $\alpha$ -FeOOH (goethite),  $\gamma$ -FeOOH (lepidocrocite) and  $\beta$ -FeOOH (akaganeite) [124]. Akaganeite has also been reported as  $\beta$ -FeOOHCl by Scheinost [124] because it is mostly found in environments with high concentration of chloride ions [125,132]. All these compounds were identified in the PHS samples by means of Raman spectroscopy analyses, as shown in Figure 7.5. Moreover, Fe<sub>3</sub>O<sub>4</sub> (magnetite) and Fe<sub>2</sub>O<sub>3</sub> (hematite) were also characterised. However, it is important to point out that the presence of hematite was probably related to the decomposition of magnetite due to the laser effect [121]. Furthermore, silicon oxide may be formed, as silicon was characterised by Raman, and present as corrosion product in the PHS sample, in accordance with Allély et al. [7] and Windmann et al. [8,19].

The corrosion process of the PHS under SST conditions can be summarised as follows: the coating layer protects the steel substrate by means of a barrier mechanism; if the steel substrate is exposed, it starts corroding. At the sample surface, there will be the predominance of FeOOH (presenting different polymorphologies) which formed due to the two electrochemical reactions (the iron oxidation and oxygen reduction), whereas Fe<sub>3</sub>O<sub>4</sub> is formed from the electrochemical reaction of FeOOH. Moreover, depending on the laser intensity, Fe<sub>3</sub>O<sub>4</sub> is decomposed into Fe<sub>2</sub>O<sub>3</sub>. Further, a mixture of oxides (aluminium, silicon and iron) may be formed inside the cracks; therefore, they could decrease the damage propagation in the coating since they play a role as protective barrier by filling the cavities

originated during corrosive attack. On the other hand, the acidification may also occur inside the cavities, therefore, enhancing the damage propagation.

Even though the electrochemical results have shown an ennoblement of the system after hot stamping, the SST results clearly indicate that the corrosion resistance of the system under continuous salt spray conditions does not improve. However, the results presented in this chapter are in good agreement with the great increase in corrosion current density and the change in the Al-rich sublayer from passive to active behaviour (as evaluated using micro cell in Chapter 6). This increase in corrosion current was due to the enrichment of iron in the coating. The PHS samples presented high susceptibility to the corrosive attack under SST conditions, possibly also due to the intrinsic defects originated from the thermo-mechanical process. These observations show that although the SST contributes to the evaluation of the corrosion resistance of PHS, despite of presenting poor correlation to weathering corrosion tests, it provides valuable insights that promote the knowledge on the material's corrosion behaviour in severe exposure conditions. Additionally, the SST conditions chosen to promote the formation of sufficient corrosion products at the sample surfaces so their nature can be analysed by Raman spectroscopy.

## 7.5 Conclusion

The effect of hot-stamping on the corrosion properties of steel coated with hot-dip Al-Si (10 % Si in mass fraction) was evaluated by means of the accelerated salt spray test (ASTM B 117) simulating a severe environment for corrosion and the corrosion products were identified by Raman spectroscopy. The results showed that the thermo-mechanical process has a substantial influence on the corrosion mechanism of the coating and on the nature of the corrosion products. The main findings can be drawn:

- i. The corrosion mechanism changed from localised to general as the precipitates found in the AR sample are no longer seen in the PHS condition.
- ii. Brownish-reddish rust is seen in the earliest corrosion stages of the tested PHS samples indicating the presence of iron at the surface. This is due to the diffusion process which takes place during hot-stamping process.
- iii. The PHS coating layer does not provide cathodic protection to the steel substrate and the intrinsic defects of the coating expose the steel substrate, enhancing corrosion at the exposed substrate.

- iv. Prior to hot stamping, either silicon oxides or bayerite ( $\alpha$ -Al(OH)<sub>3</sub>) were found as corrosion product of the AR, but in PHS samples after SST, mainly iron-based compounds were identified, including magnetite (Fe<sub>3</sub>O<sub>4</sub>), goethite ( $\alpha$ -FeOOH), lepidocrocite ( $\gamma$ -FeOOH), akaganeite ( $\beta$ -FeOOH) and silicon oxides.

## **CHAPTER 8 - Influence of different austenitisation temperatures during hot-stamping process on the local electrochemical behaviour of 22MnB5 steel coated with hot-dip Al-Si <sup>6</sup>**

### **8.1 Introduction**

It is known that the coating morphology is highly influenced by the process parameters during hot stamping, e.g., austenitisation temperature, soaking time and even the heating rate [8,19,24]. Windmann et al. [8,19] have shown that increasing the soaking temperature increases the growth of ductile intermetallic phases in the coating layer, as the iron diffusion is promoted. Nonetheless, little is known about the influence that these process parameters could have on the electrochemical behaviour of the system (coating/steel). Therefore, this work aims at correlating the effect of austenitisation temperatures during hot stamping on the morphology of the Al-Si coating with the local electrochemical properties of this system. Microstructural analysis of samples prepared at different austenitisation temperatures, maintaining the soaking time constant, was carried out using field emission-scanning electron microscopy (FE-SEM) and energy dispersive X-ray spectroscopy (EDS). Additionally, surface potential maps of the coatings' cross sections were studied by means of scanning Kelvin probe force microscopy (SKPFM). This approach allowed a better understanding the galvanic interactions within the coating layer and between the coating and the metal substrate as function of the austenitisation temperature.

### **8.2 Experimental procedure**

In this chapter, AR samples and hot-stamped samples obtained on laboratory scale, as described in section 3.2 of Chapter 3 (materials and samples' preparation), were evaluated. The experimental conditions describing the preparation of each sample are listed in Table 8.1. The experimental approach followed in this chapter is the same as that presented in

---

<sup>6</sup> This chapter has been submitted as a scientific paper to **Corrosion Science**.  
COUTO, C.P.; REVILLA, R.I.; POLITANO, R.; COSTA, I.; PANOSSIAN, Z.; DE GRAEVE, I.; ROSSI, J.L.; TERRY, H. Influence of different austenitisation temperatures during hot-stamping process on the local electrochemical behaviour of 22MnB5 steel coated with hot-dip Al-Si.

Chapter 4 (cross section characterisation - section 4.2) and in Chapter 5 (global and local electrochemical measurements - sections 5.2.1 and 5.2.2, respectively).

**Table 8.1 - Steel samples' identification and their corresponding experimental conditions**

Sample ID	Condition
AR	22MnB5 steel coated with hot-dip Al-Si (10% Si in mass fraction)
PHS850	AR condition heated at 850 °C for 8 min and hot stamped on laboratory scale
PHS900	AR condition heated at 900 °C for 8 min and hot stamped on laboratory scale
PHS950	AR condition heated at 950 °C for 8 min and hot stamped on laboratory scale

Source: Author

### 8.3 Results

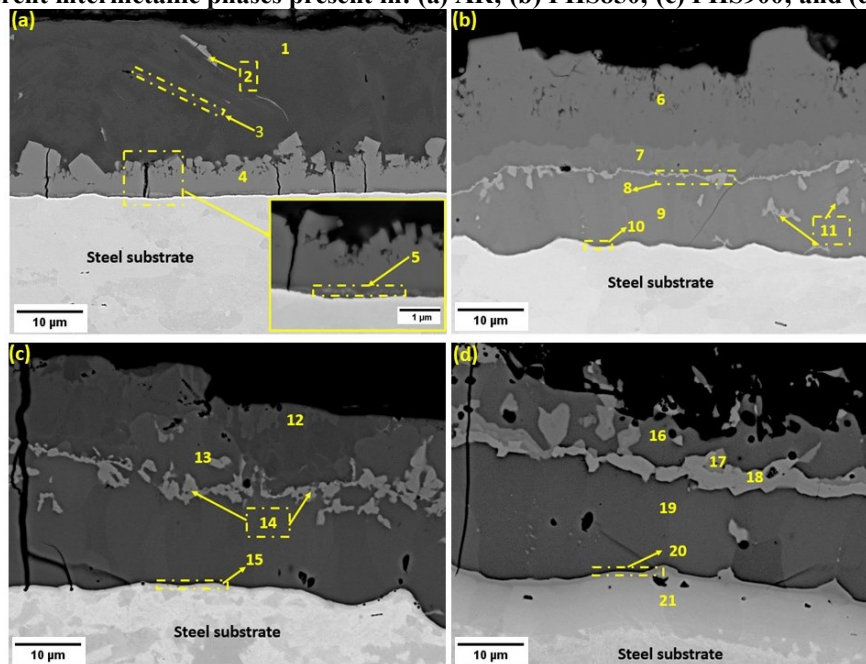
#### 8.3.1 Cross-section coating characterisation as function of different austenitisation temperatures

The effect of the different austenitisation temperatures on the Al-Si coating morphology is shown in Figure 8.1, while the EDS data are presented in Figure 8.2 (a) as well as the individual cross sectional mappings of the elements shown in Figure 8.2 (b-e). The cross-section morphology of AR, before hot stamping, is shown in Figure 8.1 (a). This is similar to that shown in Figure 4.4 which consists of an aluminium matrix (1) and some precipitates (2 and 3). The precipitates are characterised as either Al-Fe-Si (2) or Si (3). In addition to this, there is also an interdiffusion layer present (4), consisting of two sublayers (UIDL and LIDL), which shows a similar composition as the ternary precipitates (2). The EDS mapping for oxygen (Figure 8.2 (b)) shows its enrichment at the top surface.

The effect of austenitisation at 850 °C for 8 min on the Al-Si coating layer is seen in Figure 8.1 (b) and Figure 8.2 (c) for the PHS850 sample. The backscattered electron image displays different contrasts for the present phases, indicating different compositions. The top coating (spot 6) consists of a ternary Al-Fe-Si phase being enriched in aluminium, while its underlayer (spot 7) is basically composed of Al-Fe phase, since the silicon content is very little, as shown in both point ID and EDS mappings analyses (Figure 8.2 (a) and Figure 8.2 (c)). Conversely, the highest silicon content is seen in the thin and bright layer (spot 8) which is a ternary Al-Fe-Si phase (about 14 % Si in mass fraction). This same phase is also seen as an island morphology (spot 11) close to the steel substrate. The silicon content significantly decreases towards the steel substrate, while the iron content increases. There is

a thin layer (spot 10) at the interface between the coating layer and the steel substrate which has a high iron content. This can be considered as the interdiffusion layer for this sample condition. In general, the iron content gradually decreases from the steel substrate towards the coating top surface. The EDS maps (Figure 8.2 (c)) show the presence of an oxide layer at the coating top surface. This layer seems to be thicker than the one seen on the surface of the AR condition and might be related to the formation of thermal oxides due to the austenitisation of the samples during the hot-stamping process.

**Figure 8.1 - Scanning backscattered electron images showing the cross-section morphologies of 22MnB5 steel coated with hot-dip Al-Si (10 % Si in mass fraction) in different conditions highlighting the different intermetallic phases present in: (a) AR; (b) PHS850; (c) PHS900; and (d) PHS950**

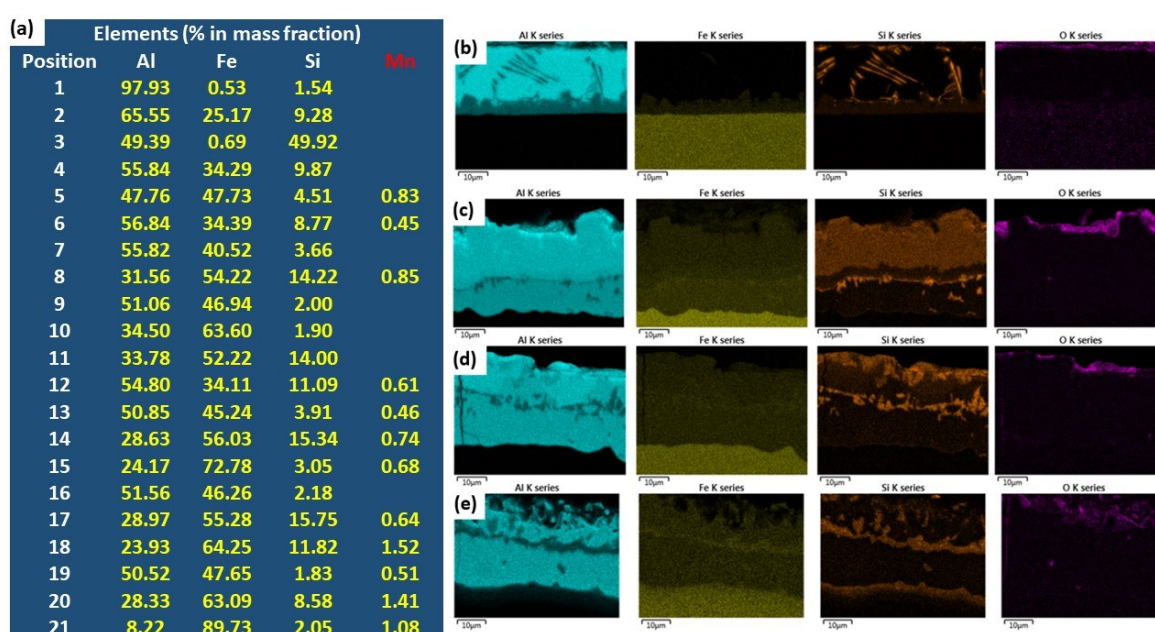


Source: Author

Increasing the austenitisation temperature to 900 °C, but keeping the soaking time for 8 min, the coating presents three regions with different contrasts (Figure 8.1 (c)), mostly related to the silicon content as seen in Figure 8.2 (d). The coating matrix presents two different phases (spots 12 and 13) which mainly differ in terms of silicon content; the dark contrast of the phase represented by spot 12 shows higher silicon content than the phase pointed out in spot 13. Comparing the silicon EDS maps in Figure 8.2 (c) and in Figure 8.2 (d), it is seen that the thickness of the top layer enriched in silicon (6) seems to decrease (compared to the sample heated at 850 °C), being more concentrated at the outer surface (spot 12). Moreover, the silicon content in this phase (spot 12) increased from 8.8 % to 11.0 % (both % in mass fraction). Nevertheless, the highest silicon content (up to 15 % in mass fraction) is found in the brightest sublayer (spot 14), similar to the one presented in

Figure 8.1 (b) (spot 8). The effect of the higher austenitisation temperature is seen mainly in the thickness and in the morphology of the Fe/Si-rich sublayer (spot 14). The latter became thicker and the fraction rate of the islands decreased. Moreover, a deep crack is seen reaching the interface between the coating layer and the steel substrate. It is not possible to determine a clear interdiffusion layer. However, the interface between the coating and the steel (spot 15) presents a high iron content, aluminium and silicon in solid solution. Therefore, this region can be associated with the interdiffusion layer. Finally, an oxide layer is also observed at the coating top surface of the PHS900 sample as seen in the EDS map for oxygen in Figure 8.2 (d).

**Figure 8.2 - EDS analyses: (a) punctual identification for the positions highlighted in Figure 8.1; and EDS elemental mappings for Al, Fe, Si and O of (b) AR; (c) PHS850; (d) PHS900; (e) PHS950**



Source: Author

The coating morphology for the samples heated at 950 °C for 8 min (laboratory scale), is the most similar to the morphologies presented in previous investigations in which the samples were produced on an industrial large scale (see Figure 4.5 (a) and Figure 7.2 (a)). It consists of five sublayers which are either enriched in aluminium (sublayers 16 and 19) or in iron/silicon (sublayers 17, 18 and 20). It is important to highlight that the Fe/Si-rich sublayers have two different contrasts: the phase in spot 17 shows a darker contrast than the phase represented by spot 18, due to the higher silicon content in its composition. Moreover, this sample condition shows a clear interface between the coating layer and the steel substrate considered as the interdiffusion layer (21). According to the EDS semi-

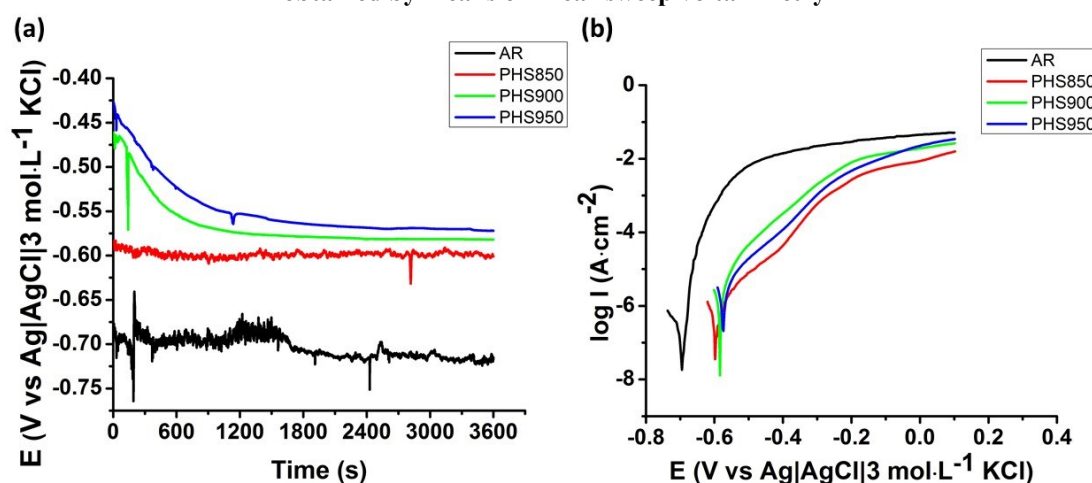
quantitative analysis (Figure 8.2(a)), this layer has a higher amount of iron. However, the elemental EDS map for silicon in Figure 8.2 (e), shows that the silicon content is high at the interface between the coating layer and the steel substrate; and its content gradually decreases towards the steel substrate. Furthermore, the number of voids also increases in the coating layer. It is important to highlight that the cracks present are limited to the interdiffusion layer; and they do not reach the steel substrate. The probably reason has been attributed to the thermal expansion coefficient of the interdiffusion layer which is similar to the one of the steel [60]. Similar to the other samples' conditions, an oxide layer can be clearly seen at the surface as shown in Figure 8.2 (e) (oxygen mapping). Additionally, manganese is often identified in the EDS point ID for most of the points analysed and presented (Figure 8.2 (a)), as a consequence of its diffusion from the steel substrate into the coating layer.

### 8.3.2 Electrochemical measurements of the coated systems as function of austenitisation temperature

The *OCP* evolution during 1 hour of immersion in 5.0 % NaCl solution (% in mass fraction) is presented in Figure 8.3. The *OCP* value for both PHS900 and PHS950, from the beginning to the end of the measurements, decreased about 100 mV. This was first related (see Chapter 5) to the dissolution of the oxide layer in contact with the electrolyte [29]. On the other hand, the PHS850 and the AR conditions show a small variation in *OCP* during the measurements, but both samples do have a noisy *OCP* signal. This can be attributed to the formation of metastable pits at the sample surface, which is characteristic of Al-Si alloys [98]. This may indicate the predominance of aluminium content over iron at the surface of the PHS850 sample. After 1 h of immersion the *OCP* of all the samples were stable. The average *OCP* values for each sample condition, as well as their standard deviations, are listed in Table 8.2. The *OCP* of the samples is shown to increase by increasing the austenitisation temperature. The AR sample displays the lowest average *OCP* (-0.715 V vs Ag|AgCl|KCl sat.) whereas the PHS950 sample shows the highest average *OCP* (-0.576 V vs Ag|AgCl|KCl sat.). Furthermore, the average *OCP* values of the PHS900 and the PHS950 are very similar, and the average *OCP* difference between these samples (PHS900 and PHS950) and the PHS850 is only about 20 mV. Although only a little difference is observed between the *OCP* values of the PHS samples, there is a trend in which the potential shifts towards nobler values by increasing the austenitisation temperature. The ennoblement of the coating layer for PHS

samples was attributed previously to the iron and silicon enrichment. Nevertheless, the formed thermal oxide layer during heat treatments may also have an influence on the shifting of the *OCP* for the PHS samples. According to the oxygen mappings shown in Figure 8.2 (b-e), the oxide layer at the top coating surface of the PHS samples appears to be thicker than one at the top coating of the AR sample. Therefore, it may influence on *OCP* shifting it to nobler values.

**Figure 8.3 - Electrochemical measurements for AR, PHS850, PHS900 and PHS950 in NaCl 5 % solution (in mass fraction): (a) open circuit potential evolution for 1 h; (b) anodic polarisation curves obtained by means of linear sweep voltammetry**



Source: Author

Figure 8.3 (b) shows the characteristic anodic polarisation curves obtained just after the *OCP* measurement for each sample condition. An active behaviour is identified in all anodic polarisation curves, due to the high chloride content in the electrolyte (5.0 % NaCl in mass fraction) which inhibits the re-passivation of the oxide layer [25]. On the other hand, the local electrochemical micro-cell measurements carried out in a less concentrate electrolyte ( $0.1 \text{ mol}\cdot\text{L}^{-1}$  NaCl) has shown that the surface (oxide layer) of both sample condition AR and PHS presented a passive behaviour. Table 8.2 also displays the average values of  $E^*$  and their standard deviations.

According to Table 8.2, the values of  $E^*$  show the same trend as that of the *OCP*: the AR sample presented the lowest average  $E^*$ , while the sample heated at the highest austenitisation temperature (PHS950) shows the highest value of  $E^*$ . The average  $E^*$  difference among the austenitised samples is very small; the highest difference is 17 mV between the PHS850 and PHS950 samples. This difference increases to 107 mV when the AR and PHS950 samples are compared.

**Table 8.2 - Average OCP,  $E^*$  and their corresponding standard deviation values for AR, PHS850, PHS900 and PHS950 samples measured in 5% NaCl solution (in mass fraction)**

Sample condition	<i>OCP at <math>t = 3600</math> s</i>		<i><math>E^*</math></i>	
	<i>(V vs Ag AgCl KCl sat.)</i>		<i>(V vs Ag AgCl KCl sat.)</i>	
	Average	Standard deviation	Average	Standard deviation
AR	-0.715	0.008	-0.701	0.004
PHS850	-0.598	0.023	-0.593	0.020
PHS900	-0.583	0.008	-0.584	0.008
PHS950	-0.576	0.007	-0.578	0.007

Source: Author

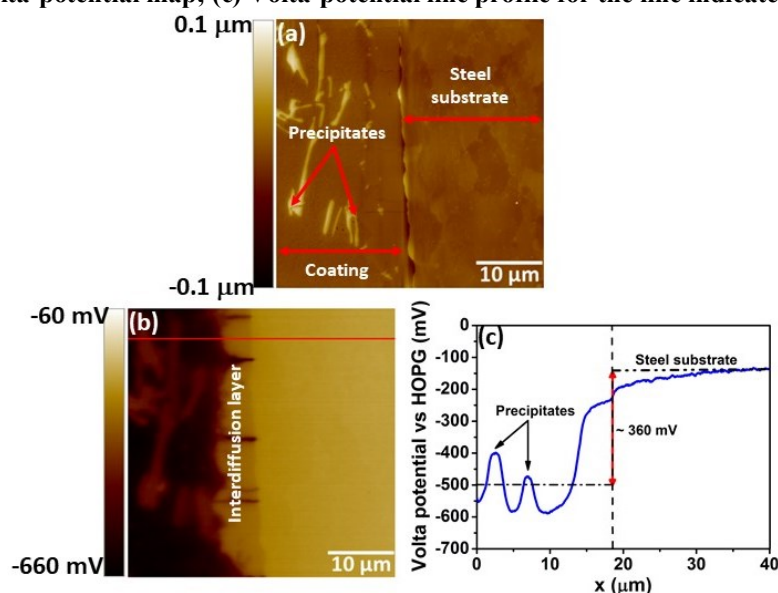
An interesting difference between the anodic polarisation curves of the samples analysed is related to the current increment: for the AR sample the current increases quickly while for the PHS samples there is a relatively slower increase (see Figure 8.3 (b)). This behaviour was first seen during the electrochemical measurements of PHS samples produced on industrial scale (Figure 5.1). This has been correlated to the presence sublayers in the coating. As the PHS samples have the sublayers enriched in iron and silicon, this may have an influence on the current increment, because these sublayers have been pointed out as nobler than the Al-rich sublayers.

### 8.3.3 Scanning Kelvin probe force microscopy analyses

Figure 8.4 shows the topography (a) and Volta-potential map (b), as well as a specific Volta-potential line profile (c) for the AR sample. These results are very similar to those presented in Chapter 5 (see Figure 5.5) which indicates a good reproducibility of the measurements. From the topographical map (Figure 8.4 (a)), it is possible to distinguish the coating layer from the steel substrate and individual precipitates in it. For the steel substrate, even some grain boundaries of the pearlite-ferrite microstructure are observed. The precipitates in the coating layer reveal a slightly higher topographical contrast.

From the Volta-potential map (Figure 8.4 (b)), the interdiffusion layer can be identified at the interface of the coating layer/steel substrate. This region is not clear in the topography map (Figure 8.4 (a)). The Z-scale shows that the Volta potential varies approximately from -660 mV to -60 mV (vs HOPG). The darkest contrast is attributed to the free aluminium layer (see Figure 8.1 (a) and Figure 8.2 (b) - Al mapping), indicating that it is the less noble phase of the system. The precipitates and the interdiffusion layer behave cathodically versus the aluminium matrix. On the other hand, the steel substrate shows the brightest contrast, related to the noblest Volta potential.

**Figure 8.4 - Cross-section image of AR sample measured by means of SKPFM: (a) topographic map; (b) Volta-potential map; (c) Volta-potential line profile for the line indicated in (b)**



Source: Author

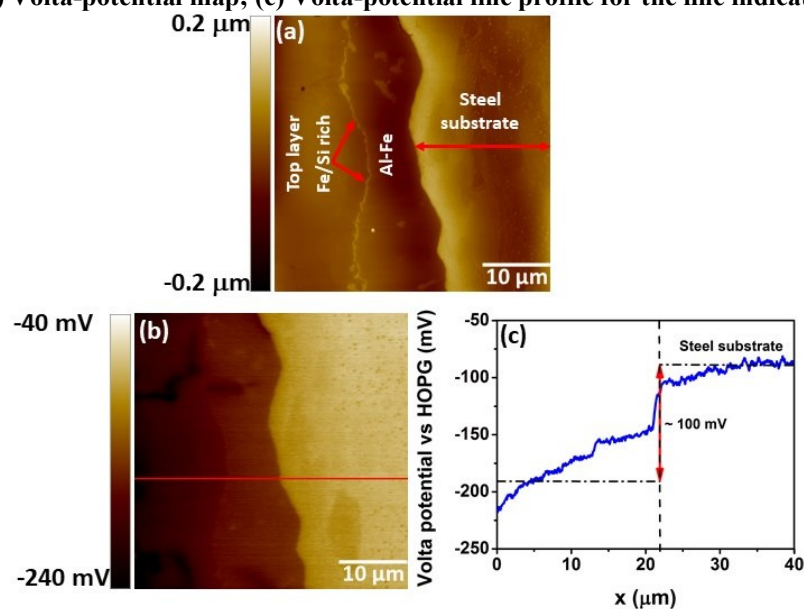
The Volta-potential line profile (Figure 8.4 (c)), corresponding to the highlighted red line in Figure 8.4 (b), indicates that the average Volta-potential difference between the steel substrate and the coating layer is approximately 360 mV. Moreover, the Volta potential of the precipitates in the coating layer is from 30 mV to 100 mV higher than the aluminium matrix. The average Volta potential of the interdiffusion layer is around -230 mV (vs HOPG) which is 115 mV lower than the average Volta potential of the steel substrate.

Figure 8.5 shows the topography (a) and Volta-potential map (b) of the cross section of the PHS850 sample. From Figure 8.5 (a), the thin sublayer and the intermetallics presented as an island morphology show higher topography than the overall coating layer which consists of different compositions along its thickness (see Figure 8.1 (b) and Figure 8.2 (a) - spots 6 and 7).

The Volta-potential map in Figure 8.5 (b) shows the trend of the Volta potential increasing towards the steel substrate. Three different contrasts are seen in the coating layer. Correlating with Figure 8.1 (b), the darkest contrast is regarding the top layer which consists of an Al-Fe-Si phase enriched in aluminium (up to 55 % in mass fraction). The thin Fe/Si-rich sublayer, highlighted in Figure 8.5 (a), shows the brightest contrast of the coating layer. The contrast difference between the Fe/Si-rich sublayer, the intermetallics as islands and the Al-Fe sublayer is not very pronounced, indicating a small Volta-potential difference among them. Nonetheless, the cathodic behaviour of the steel is kept, indicated by its brightest contrast. The SKPFM results (both topography and Volta potential) show an interdiffusion

layer in the sample which is nobler than the coating layer, but less noble than the bulk steel substrate. This interdiffusion layer was not easily distinguished in the backscattered electron image (Figure 8.1 (b)), but it was assumed as point 10 in that same image.

**Figure 8.5 - Cross-section image of PHS850 sample measured by means of SKPFM: (a) topographic map; (b) Volta-potential map; (c) Volta-potential line profile for the line indicated in (b).**

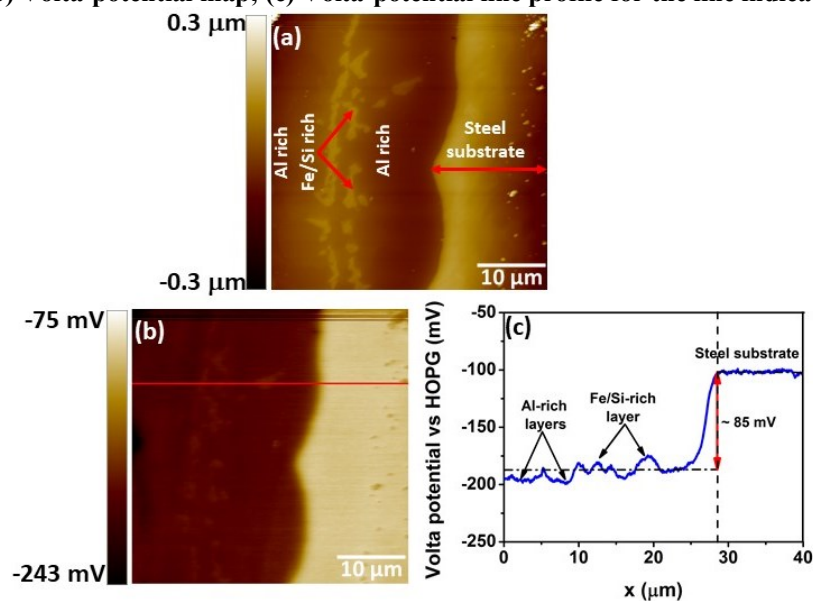


Source: Author

Figure 8.5 (c) shows the Volta-potential line profile corresponding to the highlighted line in Figure 8.5 (b). A gradient in the potential values is seen decreasing from the steel substrate to the outer surface of the coating. This can be probably related to the diffusion of iron into the coating and aluminium towards the steel substrate. Moreover, the line profile shows a great decrease in the driving force for cathodic protection (compared to the AR sample) between the coating and the steel matrix since the average Volta-potential difference between the coating layer and the steel substrate is around 100 mV. The heat treatment changed the average Volta potential of both the coating layer and the steel substrate, as they became nobler than the AR condition. The Volta-potential values of the different sublayers of the coating are distributed in a range of approximately 60 mV. Moreover, a slight peak is seen around the position  $x = 15 \mu\text{m}$ , with a potential value of approximately -155 mV (vs HOPG) which may be attributed to the Fe/Si rich sublayer. The interdiffusion layer shows an average Volta potential of around -115 mV (vs HOPG), only 30 mV lower than the average Volta potential of the steel substrate.

Increasing the austenitisation temperature to 900 °C for 8 min, the Volta-potential of the coating/steel system significantly changes, as seen in Figure 8.6.

Figure 8.6 - Cross-section image of PHS900 sample measured by means of SKPFM: (a) topographic map; (b) Volta-potential map; (c) Volta-potential line profile for the line indicated in (b)

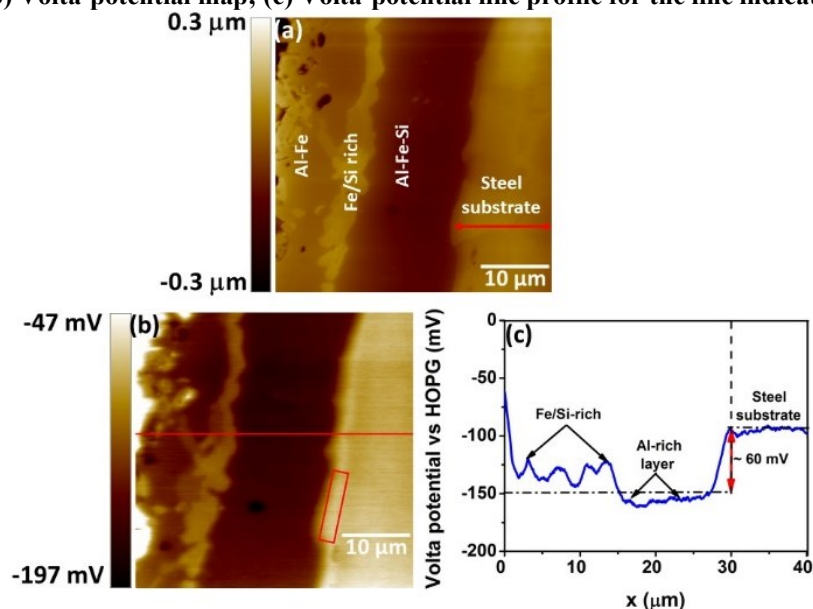


Source: Author

From the Volta-potential map, Figure 8.6 (b), it is seen that the Fe/Si-rich sublayers in the coating are slightly brighter than the overall coating. Additionally, a brighter and thin interdiffusion layer is seen at the interface between the coating and the steel. The steel substrate remains as the noblest phase in the system, indicating that it could be protected by cathodic protection provided by the coating layer. However, according to the Volta-potential line profile in Figure 8.6 (c), for the highlighted line in Figure 8.6 (b), Volta-potential difference between the coating layer and the steel substrate decreases to 85 mV in comparison with the previous PHS850 sample. The Volta-potential values of the different sublayers of the coating are distributed in a range of approximately 20 mV. Additionally, the Volta potential of the interdiffusion layer is around -180 mV (vs HOPG). However, this is difficult to determine as the interdiffusion layer is seen as a very thin interface. Nonetheless, these results show that increasing the austenitisation temperature, the coating layer becomes nobler and the Volta potential of the steel substrate also increases.

Figure 8.7 shows the topographical map (a), the Volta-potential map (b) and a Volta-potential line profile of the PHS950 sample. The different sublayers of the coating can be clearly distinguished in the topography map of the cross section (Figure 8.7 (a)).

Figure 8.7 - Cross-section image of PHS950 sample measured by means of SKPFM: (a) topographic map; (b) Volta-potential map; (c) Volta-potential line profile for the line indicated in (b)



Source: Author

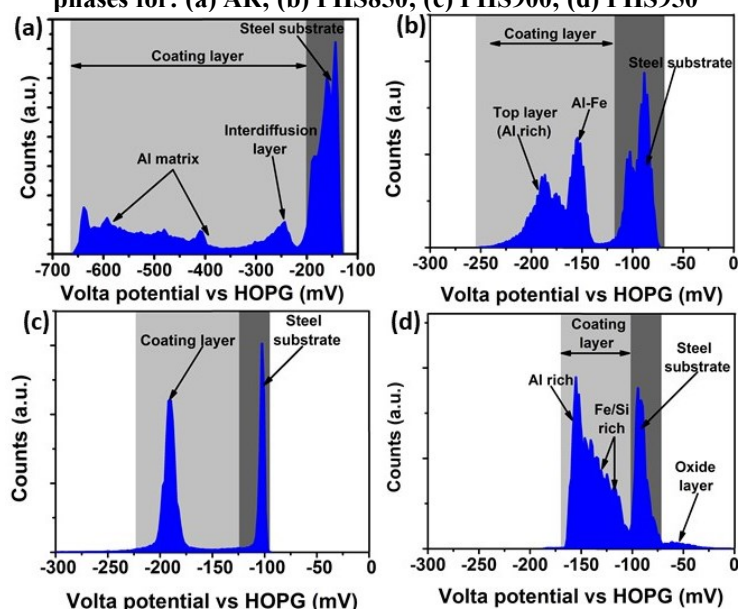
The Volta-potential map, Figure 8.7 (b), shows the brightest contrast (white) at the top surface which can probably be attributed to the thermal oxide layer, highlighted in Figure 8.7 (e) - oxygen mapping. The coating layer shows different contrasts: the Al-rich sublayer shows the lowest Volta potential, indicated by the darkest contrast, while the Fe/Si-rich sublayer shows brighter contrast than the Al-rich sublayer. Moreover, as also seen in Figure 8.2 (d), the Fe/Si-rich sublayer shows two different contrasts, indicating that one phase is nobler than another. The interdiffusion layer can be considered as the region highlighted by a rectangle, in which the Volta potential is the highest, except for the oxide layer at the top coating surface. According to the EDS mapping (Figure 8.2 (e)), even though the interdiffusion layer has a high amount of iron in it, its top is enriched in silicon which justifies the highest potential. Additionally, the silicon content decreases from the coating towards the steel substrate, while the iron content is maintained. For this reason, the interdiffusion layer and the steel substrate show similar Volta-potential values.

The Volta-potential line profile in Figure 8.7 (c) shows that the top layer (oxide layer) has the highest Volta potential around -60 mV (vs HOPG). The Volta-potential values, of the different sublayers of the coating, varies in the range from approximately -125 mV (Fe/Si-rich sublayers) to -160 mV (Al-rich sublayers) vs HOPG. Moreover, the average Volta-potential difference between the coating layer and the steel substrate is around 60 mV. This indicates the ennoblement of both the coating layer and the steel substrate. Additionally, Figure 8.7 (c) shows that the Volta potential of the steel substrate and the interdiffusion layer

is very similar, around -90 mV (vs HOPG). These SKPFM results are very similar to those presented for that industrial-PHS sample in Chapter 5 and Figure 5.5.

Figure 8.8 shows the histograms constructed from the Volta-potential values obtained in the scanned areas. For the AR sample, Figure 8.8 (a), three different areas can be clearly distinguished: the Al matrix, the interdiffusion layer and the steel substrate. As expected, this result is very similar to that presented in Chapter 5. Figure 5.4 From the histogram, it is possible to estimate the average Volta-potential value of each region. It is important to highlight that these average values can be, sometimes, slightly different from those presented in the Volta-potential line profiles for each sample, because those were related to the specific line randomly chosen in the Volta-potential map. From the histograms, the average values are related to the whole scanned area. Thus, the average Volta-potential value of the Al coating matrix, the interdiffusion layer and the steel substrate are - 480 mV, -250 mV and -140 mV (vs HOPG), respectively.

**Figure 8.8 - Histograms based on the Volta-potential map highlighting the contribution of different phases for: (a) AR; (b) PHS850; (c) PHS900; (d) PHS950**



Source: Author

Figure 8.8 (b) shows the histogram of the Volta-potential values for the PHS850 sample. The coating layer is presented by two main peaks due to the different composition across the coating. The first peak around -180 mV (vs HOPG) can be attributed to the top layer enriched in aluminium and the second peak, around -160 mV (vs HOPG), may be related to the Al-Fe phase in which the amount of iron is around 40 % (in mass fraction). The contribution of the Fe/Si- rich sublayer and the intermetallics cannot be precisely

highlighted in the histogram as they are very thin, and the relative number of counts is very limited. Finally, the contribution from the steel substrate can be seen with an average Volta-potential of around -85 mV (vs HOPG).

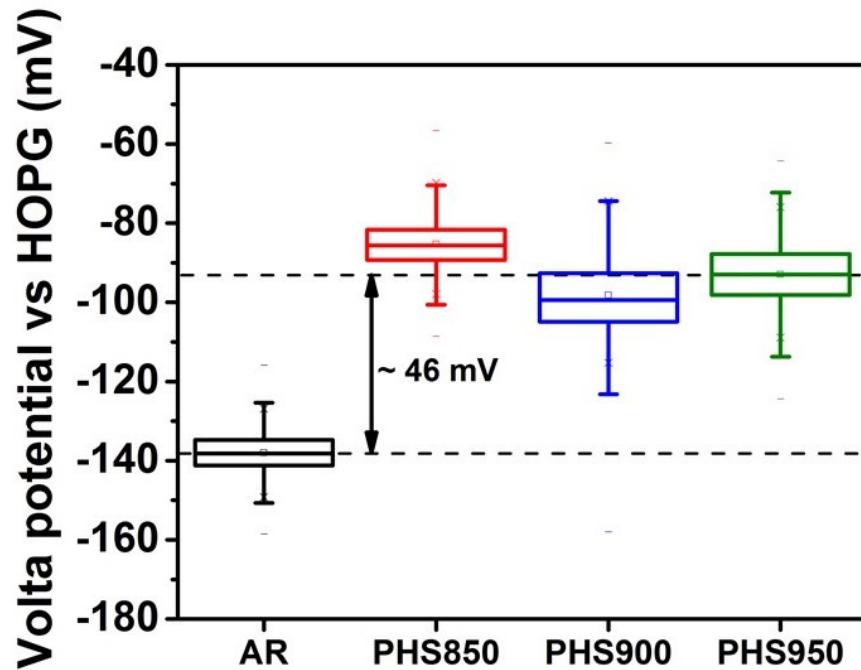
The corresponding histogram for the PHS900 sample is shown in Figure 8.8 (c). It presents two sharp peaks: the first at lower Volta potential regarding the coating layer and the second, at higher potentials, representing the steel substrate. It can be explained by correlation with Figure 8.6 (b) which shows that the Volta potential is approximately the same throughout the whole coating layer, except for the Fe/Si-rich sublayers and the interdiffusion layer. Nevertheless, as the two latter show very thin thickness, they do not show a representative contribution in the histogram. This reinforces the hypothesis risen in the discussion of Chapter 6 (see section 6.4.3) in which the Volta potential of the sublayers in the coating could be influenced by the Volta potential of the predominant phase in the coating (Al-rich sublayers).

Figure 8.8 (d) displays the histogram of the PHS950 sample. The broader area corresponds to the coating layer, as it is composed of different sublayers. The Al-rich sublayers can be characterised as the sharp peak seen at low potentials (around -150 mV vs HOPG), whereas the Fe/Si-rich sublayers show an average potential around -125 mV (vs HOPG). From Figure 8.8 (by looking at the separation between the peaks) it is clear that the Volta-potential difference between the coating layer and the steel substrate decreases as the austenitisation temperature increases. Moreover, the shift towards nobler values is seen both for the coating layer and for the steel substrate. Finally, the noblest Volta potential (-60 mV vs HOPG) is attributed to the thermal oxide layer shown in Figure 8.2 (e) and Figure 8.7 (b).

As shown by means of the Volta-potential maps and the histograms, there was an ennoblement of the steel substrate after the thermo-mechanical process, as previous seen in Figure 5.7. Figure 8.9 shows the average Volta-potential value of the bulk steel substrate for each sample condition. The Volta potential of the bulk steel substrate of each sample was measured at least three times. Thus, the box plots shown in Figure 8.9 represent the merging of all the measurements. This indicates a good reproducibility for each sample condition, even considering the slight scattering shown. This indicates a good reproducibility for each sample condition, even considering the slight scatter. The Volta-potential values of the steel in the various PHS conditions are all in the same range. Interestingly, the average Volta-potential of the steel substrate in the PHS samples is around 46 mV higher than the steel substrate in the AR condition. This is in good agreement with the value shown in Chapter 5 (approximately 53 mV) where only industrial samples were analysed. The steel

ennoblement can be related to the microstructural transformations from pearlite-ferrite into martensite, as the Volta potential is influenced by residual stress [90].

Figure 8.9 - Average Volta potential of the steel substrate as function of different austenitisation temperatures



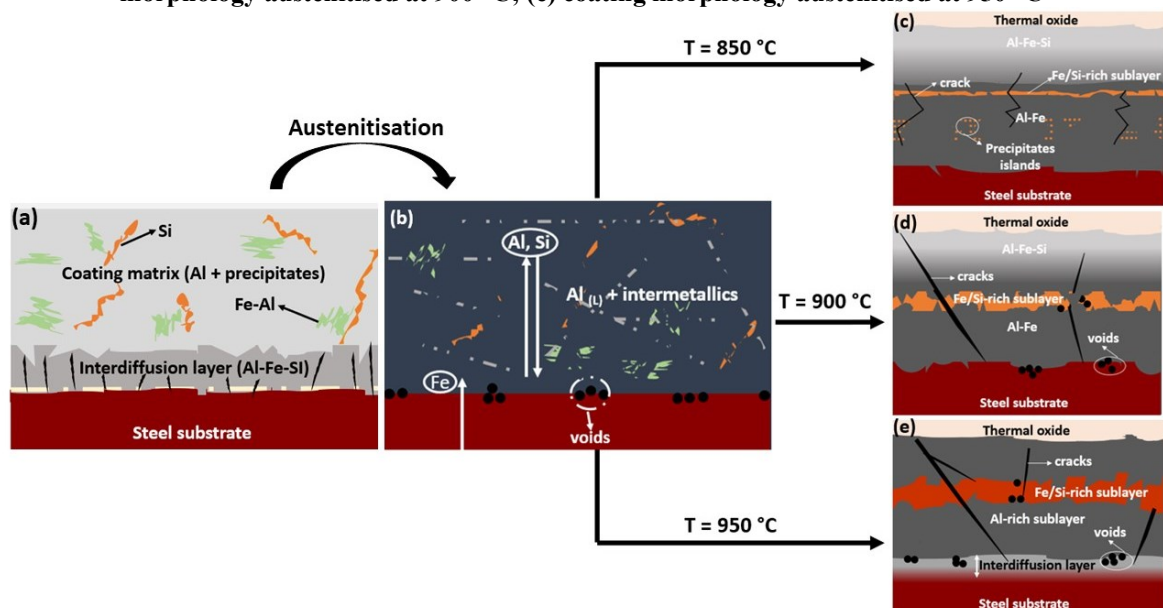
Source: Author

#### 8.4 Discussion

In general, these results show that small variations in the austenitisation temperature during hot stamping can promote substantial changes in the morphology of the Al-Si coating. Based on the discussion presented in Chapter 4, a schematic overview summarising the evolution of the Al-Si coating layer as function of different austenitisation temperatures in the hot stamping is presented in Figure 8.10. This figure represents the AR sample being submitted to austenitisation temperatures (Figure 8.10 (a)). The austenitisation step in hot-stamping processes takes place at temperatures higher than the melting temperature of the eutectic Al-Si alloy (577 °C) [24]. Thus, the first phenomenon which takes place during hot stamping is the melting of the aluminium coating matrix, but some intermetallic phases can remain in the solid state [24], as represented in Figure 8.10 (b). The austenitisation temperatures promote the diffusion of the elements, mainly iron, silicon and aluminium. The former precipitates become enriched mostly in iron and they are rearranged forming sublayers (Figure 8.10 (c-e)). The high austenitisation temperatures enhance the growth of the

sublayers enriched in iron and in silicon, as represented by Figure 8.10 (c-e), in which the sample heated at 950 °C shows the thicker Fe/Si-rich sublayer and a clear interdiffusion layer. Additionally, the density of defects, inherent to the hot-stamping process, is also dependent on the austenitisation temperature. Micro cracks and voids were observed in the sample conditions annealed at 900 °C and 950 °C. This indicates that the higher the austenitisation temperature, the higher diffusion among the elements and more pronounced the thermal expansion.

**Figure 8.10 - Schematic overview representing the changes in the Al-Si coating morphology as function of temperature: (a) AR condition; (b) AR condition at austenitisation temperatures showing the melted coating layer and the solid intermetallics; (c) coating morphology austenitised at 850 °C; (d) coating morphology austenitised at 900 °C; (e) coating morphology austenitised at 950 °C**



Source: Author

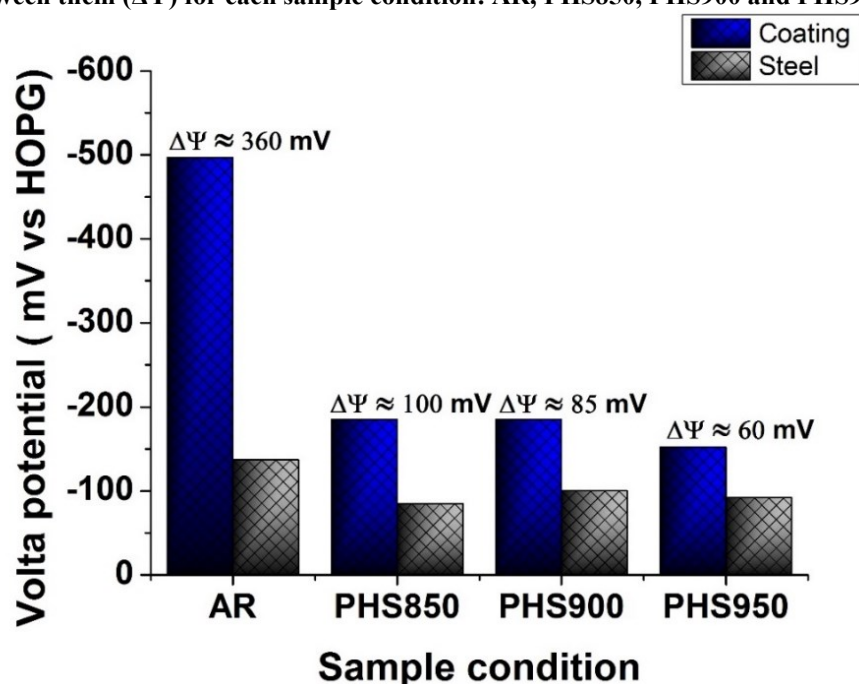
Fan et al. [24] and Windmann et al. [8,19] have shown that the formation of intermetallics takes place in the first 2 min of the austenitisation. Furthermore, successive metallurgical transformations occur enhanced by iron enrichment. Nevertheless, they are influenced by the other hot-stamping parameters, such as soaking time and the cooling rate. The latter may have an influence suppressing the formation of a stable phase. Additionally, it is important to point out that the intermetallics might originate from metastable phases. For this reason, it is rather complicate to determine the most accurate phase and/or stoichiometry by means of a semi-quantitative analysis because some of the intermetallics, mainly the ternaries of the  $\tau$ -phases (from  $\tau_1$  to  $\tau_9$ ), present very similar composition [57].

As expected, these changes on coating morphology and composition greatly altered the electrochemical behaviour of the system (steel/coating) both on global and on local scale.

As already noticed in Chapter 5, a similar trend was seen between corrosion potential and Volta potential. From the *OCP* and *LSV* measurements, the effect of hot stamping was evaluated on the global electrochemical behaviour of the system (coating/steel). Moreover, as a complementary approach, the local electrochemical techniques revealed the high complexity of the electrochemical behaviour on local scale, greatly influenced by the complex physical metallurgy of the coating. However, based on the available data from this thesis, a further step can be considered for better characterisation of all the possible steps involved in the corrosion mechanism of the system (either before or after hot stamping). This is possible by means of non-steady state techniques, such as electrochemical impedance spectroscopy. Furthermore, local electrochemical impedance spectroscopy can be considered on the scope of local corrosion behaviour. However, for a better understanding of the non-stationarities inherent, present in a localised corrosion system, odd-random phase multisine EIS is recommended.

In Figure 8.11 is summarised the average Volta potential of the coating layer, the steel substrate and the difference between them. This difference clearly decreases as the austenitisation temperature increases, which is an important overall observation.

**Figure 8.11 - Average Volta potential of the coating layer, the steel substrate, and the difference between them ( $\Delta\Psi$ ) for each sample condition: AR, PHS850, PHS900 and PHS950**



Source: Author

As seen in Figure 8.11, the higher the austenitisation temperature, the lower the Volta-potential difference between the coating layer and the steel substrate. Among the

austenitised samples, the PHS850 shows the highest Volta-potential difference between the coating layer and the steel substrate (100 mV). Moreover, as observed in Figure 8.5 (c), the Volta potential increases gradually towards the steel substrate for this sample condition. This could contribute to the reduction of galvanic-coupling effects between the steel substrate and the coating layer. The overall coating ennoblement is mainly related to iron enrichment. However, silicon plays a substantial role, as it forms solid solution with iron, shifting the Volta potential of the Fe/Si-rich sublayers towards nobler values. On the other hand, the steel substrate becomes nobler due to the microstructural transformations.

In this chapter, the effect of one hot-stamping parameter (austenitisation temperature) was evaluated in terms of coating layer morphology/structure and linked with the electrochemical behaviour. At this point, it is worth to speculate the influence of lower silicon contents in the coating layer on the electrochemical behaviour of the system. This would probably alter most of the structure-composition of the coating layer, mainly the Fe/Si-rich sublayers. Therefore, it could also influence the local electrochemical behaviour of the referred sublayers, decreasing its corrosion and breakdown potentials, as silicon has been pointed out as the reason for the noblest corrosion and breakdown potential of the Fe/Si-rich sublayers. Moreover, on the global electrochemical behaviour a reduction of silicon content could, for instance, result on higher current densities in the anodic branch. The Fe/Si-rich sublayers have been pointed out in this thesis as the reason for the slowest increment of the current in PHS samples.

The results presented in this chapter highlight the high dependence of the morphology and local electrochemical behaviour of the coating/steel system on the austenitisation temperature. In general, the driving force for cathodic protection is influenced by changes in austenitisation temperature, which is shown by variations in the Volta-potential difference between the steel substrate and the coating layer.

## 8.5 Conclusion

The effect of different austenitisation temperatures on the electrochemical behaviour of Al-Si coatings (10 % Si in mass fraction) was evaluated for press-hardened steels on laboratory scale. The main findings can be summarised as follows:

- i. This work demonstrates that small changes in austenitisation temperature (50 °C) during the hot-stamping process can result in great variations in the Al-

Si coating morphology and consequently alter the (local) electrochemical behaviour of the system (coating/steel).

- ii. The hot-dip Al-Si coating becomes a multi-layered system as the austenitisation temperature increases. The increase in austenitisation temperature accelerates the diffusion of iron into the coating and promotes the formation of either binary or ternary intermetallic phases. The presence of cracks and voids is also related to higher austenitisation temperatures.
- iii. Corrosion potential in NaCl solution (5% in mass fraction) shifts to nobler values by increasing the austenitisation temperature. This is attributed to the iron enrichment in the coating and the formation of thermal oxides. However, a small difference was seen between the heat treated (and hot stamped) samples.
- iv. The Volta-potential difference between the coating layer and the steel substrate, and therefore the driving force for cathodic protection, decreases as the austenitisation temperature during the hot-stamping process increases. Both coating layer and steel substrate become nobler after the thermo-mechanical process: the first one due to the iron enrichment into the coating layer, and the second due to the phase transformation of the steel substrate from pearlite-ferrite to martensite.

## **CHAPTER 9 - Use of Synchrotron based X-ray diffraction for monitoring *in situ* surface modifications of the Al-Si coated 22MnB5 steel for hot stamping as function of exposure in chloride containing solutions**

### **9.1 Introduction**

Currently, there is a drive to study surface modification due to corrosion *in situ* as function of time when a metal is exposed to a hostile environment. Several methods are applied such as *in situ* infrared (IR), Raman, near ambient XPS and ambient SEM. Fleischmann et al. [135] have reported already in 1980 on the possibility of *in situ* observation of electrochemical interfacial reactions between electrode and electrolyte making use of synchrotron X-ray diffraction. Robinson et al. [136] pointed out the advantages of X-ray techniques for electrodes studies, mainly *in situ*, using synchrotron radiation as a method to evaluate the surface conditions in the presence of an electrolyte. The main advantage of this method is the high degree of penetration of the radiation throughout the electrolyte/surface [136].

Concerning the framework of this thesis, in Chapter 4 and Chapter 8 it was shown that the Al-Si coating, either before or after hot stamping, presents a complex morphology-composition highly dependent on the process parameters (hot-dip and hot stamping). This makes the characterisation of these system by means of the compositional micro-analyses (EDS) rather difficult. Lemmes [49] has suggested the use of high resolution diffraction methods to characterise the intermetallic phases in the Al-Si coatings.

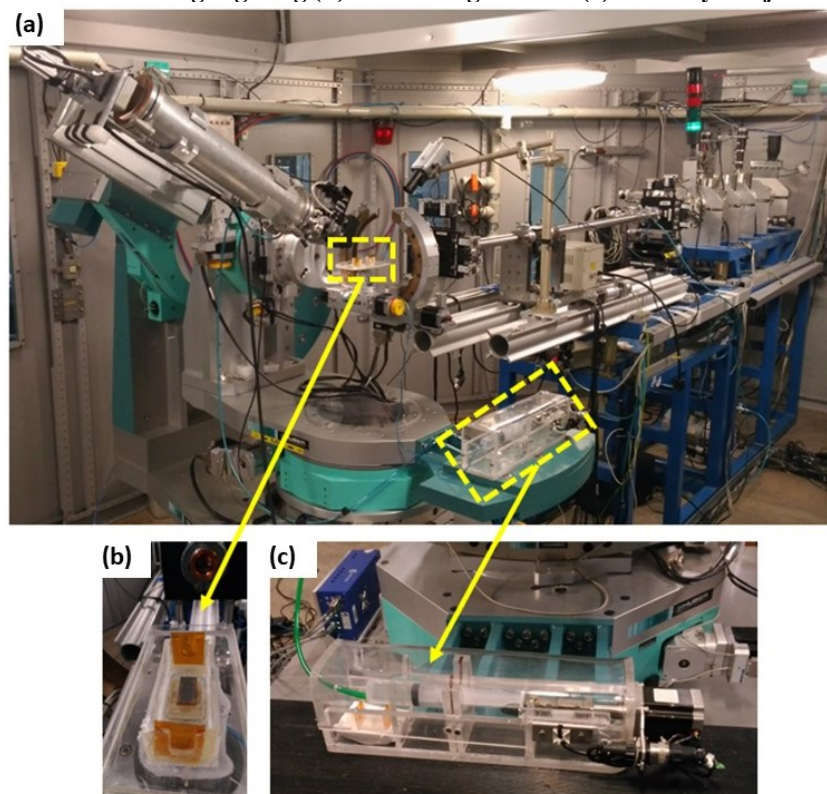
Considering the trend for *in situ* corrosion studies and the high complexity of the Al-Si coatings structure (before and after hot stamping), this chapter shows a feasibility study aiming at the *in-situ* monitoring of crystalline phase transformations present at the surface of AR and PHS samples in a chloride medium (3.5 % NaCl in mass fraction) by means of synchrotron X-ray diffraction. It is expected that the *in-situ* monitoring of the surface condition in contact with an electrolyte can bring insights about the dynamic of phase transformations in the Al-Si coating, which directly influences the corrosion properties. The main advantage of the synchrotron X-ray diffraction is related to the high energy of the X ray. In this work, the samples' coating layers (AR and PHS) are thick, approximately 25  $\mu\text{m}$ ; hence, a high X-ray energy combined with an appropriate geometry allow the characterisation of the whole coating from the surface.

## 9.2 Experimental procedure

### 9.2.1 Synchrotron X-ray diffraction

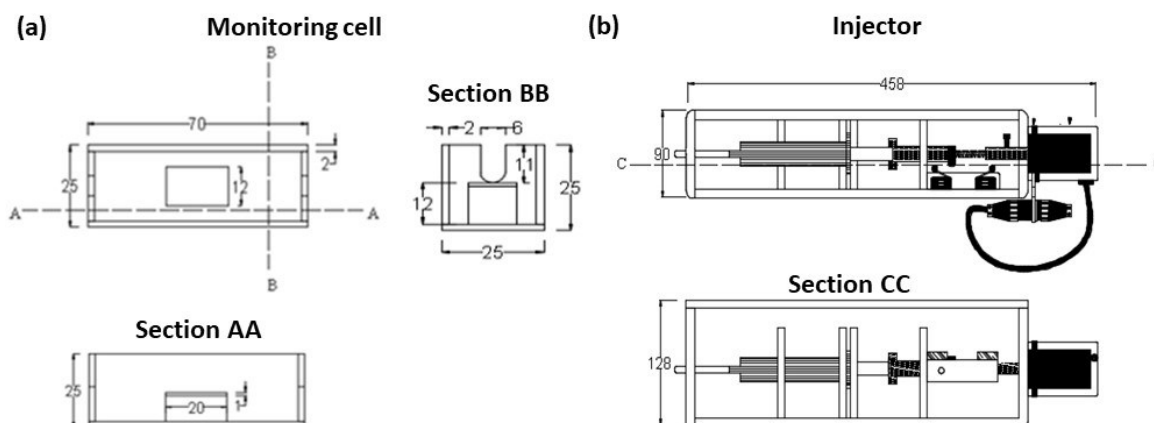
One of the limitations regarding the investigation of corrosion processes by means of synchrotron radiation is related to the adequate instrumentation [136]. Therefore, a specific approach was designed to monitor the changes at the sample's surface, exposed to an electrolyte (3.5% NaCl in mass fraction), by means of synchrotron X-ray diffraction. Figure 9.1 (a) shows the apparatus *in loco* at the National Synchrotron Light Laboratory (LNLS), in Brazil. Figure 9.1 (b) highlights the monitoring cell/sample holder, whereas Figure 9.1 (c) shows the electrolyte injector. They were connected by a hose, and both were integrated to the XRD2 beam line [137]. The detailed specifications of the monitoring cell and the injector are given in Figure 9.2 (a) and Figure 9.2 (b), respectively, in which the dimensions are in mm and the scale 1:1.

**Figure 9.1-** *In loco* apparatus for *in-situ* synchrotron X-ray diffraction integrated to (a) XRD2 beam line at LNLS highlighting (b) monitoring cell and (c) electrolyte injector



Source: Author

**Figure 9.2 - Detailed specifications of (a) monitoring cell and (b) electrolyte injector, showing the dimensions in mm and scale 1:1**



Source: courtesy G. Carezzato

The cell shown in Figure 9.2 (a) consists of a polypropylene box with two kapton-polyimide windows allowing that the X rays go throughout it at different angles. The flat sample is placed in the middle of the box that is on the top of the goniometer head. For safety reasons, the central box is positioned over a tray to avoid the spillage of liquid on precision parts of the equipment. On the bottom of the cell there is a connection to the hose linked to the plunger injector. The plunger is driven by a step motor. This way, it was possible to synchronise the filling up and draining of the electrolyte from the cell with the actual data acquisition of diffraction patterns.

The experiments were divided into cycles. One cycle consisted of the immersion of sample in the 3.5 % NaCl solution (in mass fraction) and then the acquisition of the diffraction pattern. First, the cell (Figure 9.1 (b) and Figure 9.2 (a)) was filled with the electrolyte and the sample was kept immersed in it for an average time of 20 min. Then, the electrolyte was drained from the cell through the plunger and the XRD measurement was carried out. It was necessary to remove the electrolyte because it would influence on the scattering between the beam and the sample. It is important to highlight that the samples' surfaces remained wet and exposed to the atmospheric air during the measurements. The acquisition time of the diffraction pattern took approximately 40 min. This procedure was repeated several times for each sample condition.

The X-ray diffraction experiments were performed in the Bragg-Brentano geometry. The most appropriate incidence angle on the specimen was found to be  $5^\circ$  for a collimated beam of rectangular section of approximately 2.0 mm wide and 0.7 mm height. A Mythen detector and a wavelength corresponding to 7 keV (0.177127 nm) were used.

### 9.2.2 Phase analysis

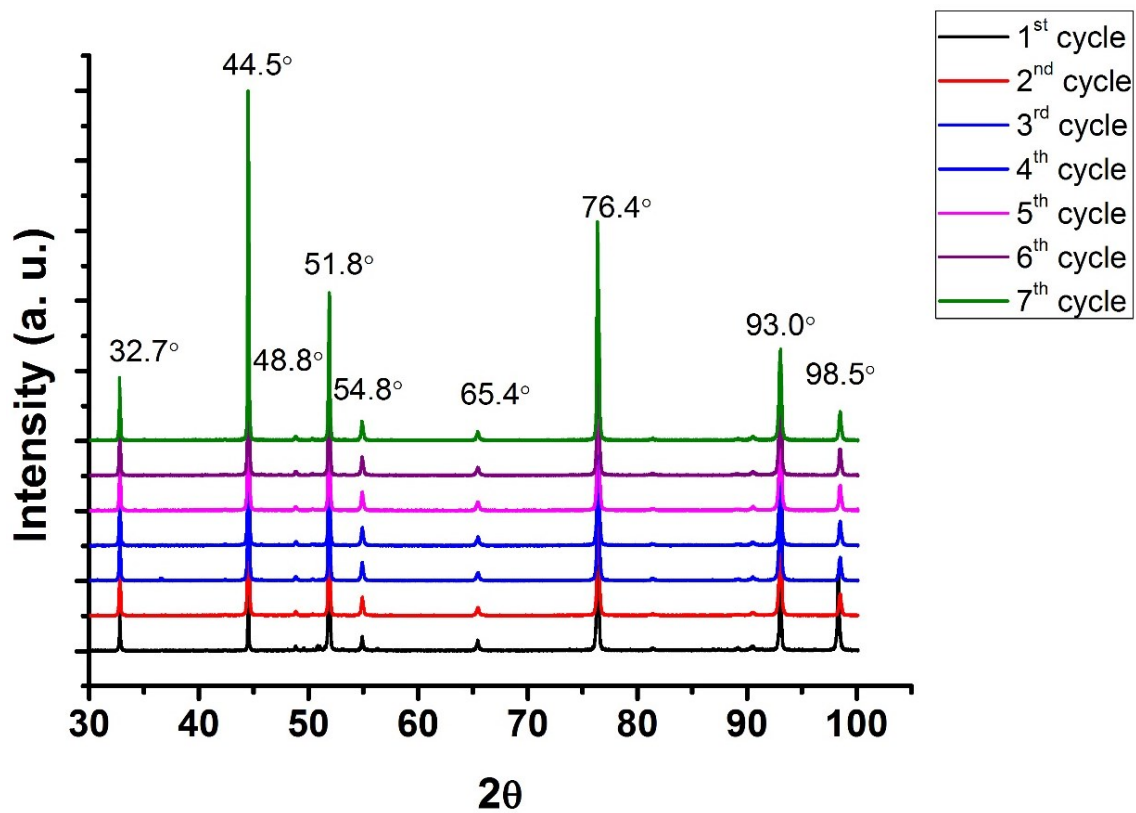
A computer programme in Python language was developed, in which all the possible reflexion positions for all phases found in literature, regarding the Fe-Al-Si system and the possible corrosion products formed, were compared with the diffraction pattern obtained experimentally. As an outcome, a list of possible phases was suggested for each peak presented in the diffraction patterns. This procedure ensured the indexing process.

## 9.3 Results

### 9.3.1 Synchrotron X-ray diffraction

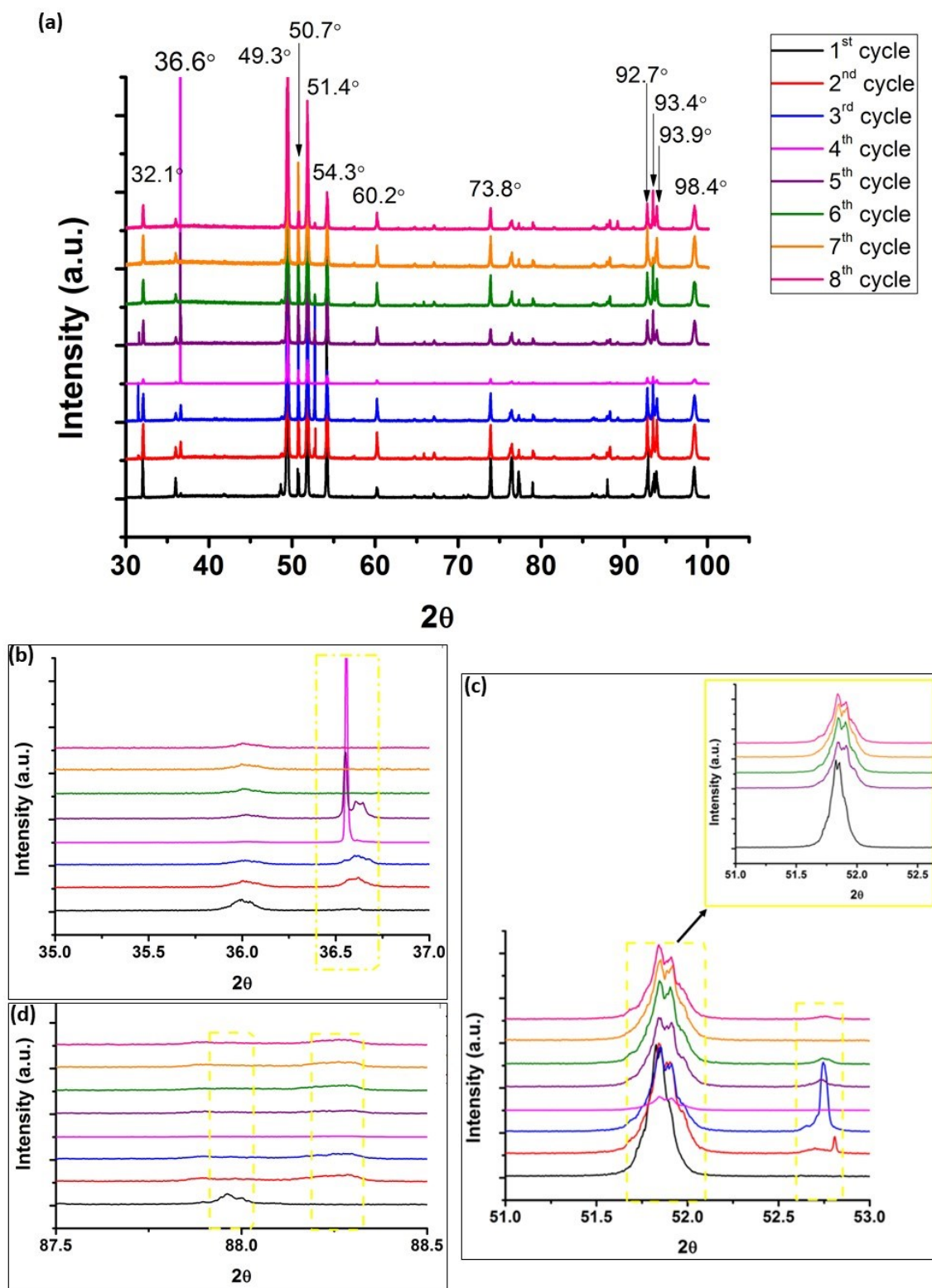
The sequence of diffraction patterns obtained for both AR and PHS samples are shown respectively in Figure 9.3 and Figure 9.4. For the AR condition, changes were not seen related to the position of the main peaks presented in the patterns considering the different cycles. On the other hand, for the PHS condition, small changes were seen in the sequence of the X-ray diffraction patterns as seen in Figure 9.4 (b-c). These changes can be correlated to a crystalline phase, which might be formed by increasing the exposure time of the sample in the electrolyte. This is indicated by the dashed areas in Figure 9.4 (b-c) at positions around  $\theta = 36.5^\circ$ ,  $52.2^\circ$  and  $88.25^\circ$ . On the other hand, at the position  $\theta = 88.0^\circ$  the peak seen in the first cycle did not appear in the other cycles. Nevertheless, major change observed in the sequence of the diffraction patterns is regarding the slight shift of the peaks as shown in the inset image in Figure 9.4 (c). Despite the questions raised about the mean of these slight changes in the samples, indicated by the sequence of the X-ray diffraction patterns, these results showed that the proposed approach worked as principle to monitor the sample surface.

Figure 9.3 - Sequence of diffraction patterns for AR sample condition. Each cycle consists of immersing the sample in NaCl 3.5% (mass fraction) for 20 min and 40 min of exposure to the air for the measurements



Source: Author

Figure 9.4 - Sequence of diffraction patterns for PHS sample condition. Each cycle consists of immersing the sample in NaCl 3.5% (mass fraction) for 20 min and 40 min of exposure to the air for the measurements



Source: Author

### 9.3.2 Indexing patterns

The conventional software for phase identification, such as X-Pert and GSAS II, were extensively tried and showed not to be suitable for the analyses of the obtained synchrotron X-ray diffraction data. This can be ascribed to the absence of standard X-ray diffraction parameters in the conventional software that did match the measured ones, for most of the phases present in the Fe-Al-Si system found in the software libraries. On the other hand, many of these phases already have their crystalline structure, symmetries and lattice parameters reported and available [58]. These parameters enable the direct determination of the possible reflexion positions for each family of crystallographic planes [74].

The main peaks presented in the X-ray patterns for both AR and PHS samples were indexed in Python, where a specific data base, based on the literature [56–58], was built to characterise the possible phases of the Al-Fe-Si system. The results for AR sample are seen in Table 9.1. Some criteria were considered in order to select the most suitable phase for each peak, such as: molten bath composition, process parameters (maximum austenitisation temperature in hot stamping) and lower Miller indices. Additionally, the overlapping of some X-ray diffraction peak of phases can occur.

The metastable phases ( $\mu_x$  - where  $x$  is any index represented by an Arabic number) seen in Table 9.1 could always be present, due to the transformation kinetics, which was very fast, as some previous research had shown [8,24]. However, the metastable phases tend to transform into a more stable phase. The steel substrate of AR condition was composed of ferrite and pearlite, which was hot dipped in an Al-Si molten bath at temperature range from 600 °C - 750 °C. For these reasons, martensite could not be considered as a suitable phase as well as the intermetallic  $\text{FeSi}_2$ , which resulted from an invariant equilibrium between iron and silicon at 937 °C:  $\text{FeSi}_2 \leftrightarrow \text{FeSi}_2 + \text{Si}$  [58]. The  $\theta$  and  $\eta$  phases were not selected as the most suitable phases for the AR sample, though they have been suggested as possible phases. However, these two intermetallic phases are often suggested in the literature as the constituents of the interdiffusion layer [52].

**Table 9.1 - Characterisation of the main peaks present in the sequence of diffraction pattern for the AR sample, indicating the most suitable phases**

Peaks	$d_{hkl}$	Possible phases	Diffraction planes	Most suitable(s)
32.79	-0.1396	$\mu_3$	(014) (411) (430)	Cristobalite
		$\mu_2$	(401)	
		$\mu_5$	(402)	
		Cristobalite	(111) (114)	
		$\tau_2$ (Fe <sub>2</sub> Al <sub>5</sub> Si <sub>2</sub> )	(201)	
44.51	-0.3396	Cristobalite	(201)	Cristobalite
		$\mu_3$	(155)	
		$\mu_2$	(250)	
48.84	-0.1354	$\tau_6$ (Fe <sub>2</sub> Al <sub>9</sub> Si <sub>2</sub> )	(514)	$\tau_6$
		$\mu_3$	(224)	
51.89	0.1220	$\tau_5$ (Fe <sub>2</sub> Al <sub>7,4</sub> Si)	(335)	$\tau_5$
		Fe (martensite)	(241)	
54.9	0.1206	FeSi <sub>2</sub>	(101) (110)	$\tau_6$
		$\tau_6$ (Fe <sub>2</sub> Al <sub>9</sub> Si <sub>2</sub> )	(104)	
		$\tau_5$ (Fe <sub>2</sub> Al <sub>7,4</sub> Si)	(134)	
		goethite	(335)	
65.45	0.0917	FeSi <sub>2</sub>	(410)	Bayerite
		bayerite	(341)	
76.4	0.1844	Hematite	(150)	Cristobalite Fe <sub>3</sub> Al
		Cristobalite	(305)	
		Fe <sub>3</sub> Al	(132)	
		FeSi <sub>2</sub>	(313)	
93.03	0.1548	FeSi <sub>2</sub>	(152)	Hematite
		Hematite	(045)	
		Fe (ferrite)	(140)	
98.5	-0.1042	Hematite	(445)	Hematite Bayerite
		Bayerite	(332)	
		FeSi <sub>2</sub>	(421)	

Source: Author

The result of the indexing patterns for PHS sample is shown in Table 9.2. For PHS condition, the phases formed in the invariant reactions starting from 942.8 °C were considered [58] as the austenitisation temperature during hot stamping can reach 950 °C.

Similar to the AR condition, metastable phases ( $\mu_x$ ) were also indexed in the patterns for PHS. However, they probably will transform into a more stable phase. The results presented in Table 9.2 suggested that a mixture of oxides was also presented at the surface of PHS sample. It consisted mostly of iron and silicon oxides. Aluminium-based oxide was not identified after hot stamping. Moreover, the PHS coating layer was composed of different intermetallic phases including  $\theta$  (Fe<sub>4</sub>Al<sub>13</sub> or FeAl<sub>3</sub>),  $\eta$  (Fe<sub>2</sub>Al<sub>5</sub>) and  $\tau_6$  (Fe<sub>2</sub>Al<sub>9</sub>Si<sub>2</sub>).

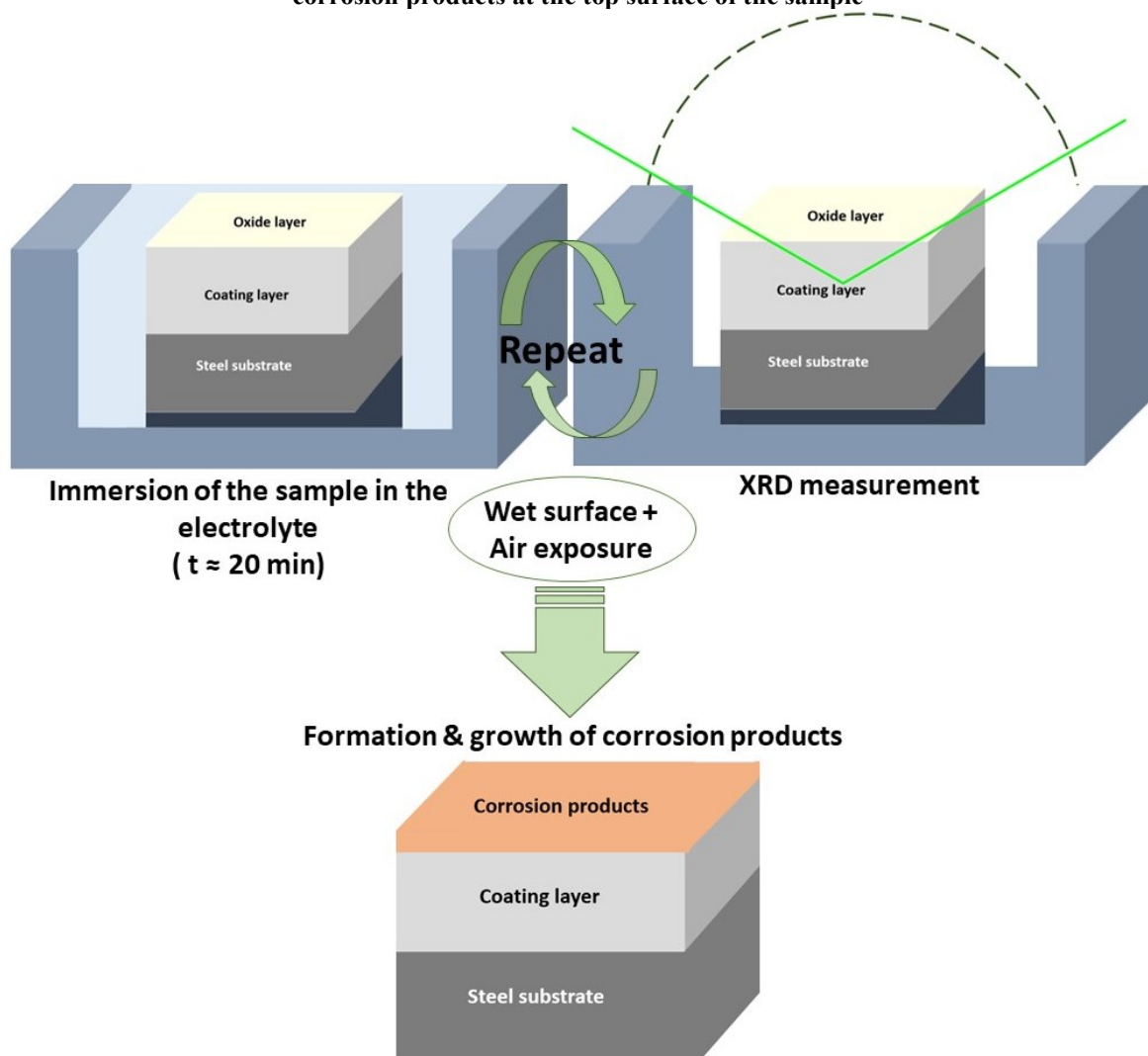
**Table 9.2 - Characterisation of the main peaks present in the sequence of diffraction pattern for the PHS sample, indicating the most suitable phases**

2 $\theta$	d <sub>hkl</sub>	Phases	Diffracted planes	Most suitable
32.05	-0.2841	$\eta$ (Fe <sub>2</sub> Al <sub>5</sub> ) $\tau_6$ (Fe <sub>2</sub> Al <sub>9</sub> Si <sub>2</sub> ) $\mu_5$ $\mu_6$	(020)	$\eta$
36.6	-0.1696	$\tau_2$ (Fe <sub>2</sub> Al <sub>5</sub> Si <sub>2</sub> ) $\theta$ (Fe <sub>4</sub> Al <sub>13</sub> or FeAl <sub>3</sub> )	(024)	$\theta$
50.7	0.4109	$\eta$ (Fe <sub>2</sub> Al <sub>5</sub> ) $\tau_5$ (Fe <sub>2</sub> Al <sub>7.4</sub> Si)	(141)	$\eta$
51.84	0.1250	$\mu_1$	(421)	$\mu_1$
54.17	0.0954	$\tau_6$ (Fe <sub>2</sub> Al <sub>9</sub> Si <sub>2</sub> ) $\mu_3$ $\mu_2$	(424)	$\tau_6$
60.23	-0.0919	Hematite FeSi <sub>2</sub>	(512)	Hematite
73.8	-0.1236	$\eta$ (Fe <sub>2</sub> Al <sub>5</sub> )	(311)	$\eta$
92.7	0.1267	Akaganeite Magnetite FeSi <sub>2</sub>	(330)	Akaganeite
93.52	0.2488	Hematite Goethite	(405) (434)	Hematite
93.88	0.4843	$\tau_6$ (Fe <sub>2</sub> Al <sub>9</sub> Si <sub>2</sub> ) $\eta$ (Fe <sub>2</sub> Al <sub>5</sub> ) FeSi <sub>2</sub>	(132) (312)	$\tau_6$
98.4	-0.1012	Cristobalite FeSi <sub>2</sub>	(445)	Cristobalite

Source: Author

For both sample conditions, the alternating process of immersing the sample in the electrolyte and exposing the wet sample surface to the air, for XRD measurements, may lead to the formation and growth of corrosion products. A generic schematic diagram representing the steps of the experimental procedure and the formation of the corrosion products at the top surface is seen in Figure 9.5.

**Figure 9.5 - Schematic diagram for a generic coated sample representing the steps of immersion and measurements by X-ray diffraction. The alternating procedure promotes the formation and growth of corrosion products at the top surface of the sample**



Source: Author

#### 9.4 Discussion

Based on the proposed approach, it was possible to monitor the samples' surface exposed to an electrolyte. Additionally, the data were analysed by means of a new developed programme in Python. This enabled the correlation of the suggested results with those previously obtained in either this thesis or in the literature. Therefore, the technique worked as principle and the results obtained can either support the previous ones obtained in this thesis or bring different insights about the corrosive process of the AR and PHS systems.

The results about the possible phases constituting either the AR or the PHS samples brought an important contribution in the discussion related to the formation of the

intermetallic phases. The reactions taking place during the hot-dip process do not follow the thermodynamic of equilibrium, considering the short time of the process. Thus, the intermetallic phases formed during hot dipping are greatly influenced by process parameters, such as time and temperature [55]. Thus, they cannot be predicted by the equilibrium diagrams [16]. The same statement can be considered for hot-stamped steel coated with Al-Si. As seen in Chapter 4, the thermo-mechanical process changes the coating morphology, as well as its composition due to the intermetallic phases' transformations. These transformations are enhanced by the diffusion process among the chemical elements present in the system. Moreover, the entropy shall be considered as one of the reasons for the different coating's morphologies for both AR and PHS samples conditions in the literature. Hence, the presence of stable phases (those which can be predicted by means of equilibrium diagram) can be justified if the condition of local equilibrium is assumed [138]. The latter results in micro systems in which the compositions may vary from samples to samples, even from small regions to small regions, due to the segregation formed during the liquid/solid transformations [138].

From Table 9.1, the intermetallic phases indicated as constituents of AR sample are  $\tau_5$ ,  $\tau_6$  and  $\text{Fe}_3\text{Al}$ . The  $\tau_5$  and  $\tau_6$  intermetallics could be formed from the quasiperitectic invariant equilibria reaction at 658.7 °C:  $\text{L} + \tau_2 \leftrightarrow \tau_5 + \tau_6$ . The liquid (L) phase in this reaction consists of Al 85.95 %, Fe 1.40 % and Si 12.64 % (% in atomic fraction) [58]. These intermetallics have also been reported by other authors [16,24,51]. On the other hand, the most probables intermetallic phases in the PHS sample are  $\theta$  ( $\text{Fe}_4\text{Al}_{13}$  or  $\text{FeAl}_3$ ),  $\eta$  ( $\text{Fe}_2\text{Al}_5$ ) and  $\tau_6$  ( $\text{Fe}_2\text{Al}_9\text{Si}_2$ ). In addition to the intermetallic phases, a mixture of oxides were characterised in both sample conditions, AR and PHS. These results are in agreement with the Raman results presented in Chapter 7 (Figure 7.4 and Figure 7.5). Before hot stamping, the corrosion products found were either silicon oxides or bayerite ( $\alpha$ - $\text{Al}(\text{OH})_3$ ). Moreover, lepidocrocite ( $\gamma$ - $\text{FeOOH}$ ) may be formed if the steel substrate is reached. After hot stamping, the nature of the corrosion products changed; mainly iron-based compounds were identified on PHS samples including: hematite ( $\alpha$ - $\text{Fe}_2\text{O}_3$ ), magnetite ( $\text{Fe}_3\text{O}_4$ ), goethite ( $\alpha$ - $\text{FeOOH}$ ), lepidocrocite ( $\gamma$ - $\text{FeOOH}$ ) and akaganeite ( $\beta$ - $\text{FeOOH}$ ). During the Raman measurements, the presence of hematite was associated with the thermal decomposition of magnetite, by means of the laser intensity. However, the results of synchrotron X-ray diffraction shows hematite as corrosion product formed in chloride medium.

As a feasibility study, some improvements shall be done as well as a more dedicated investigation related to the meaning of the small changes presented in the sequence

of X-ray diffraction patterns seen for the PHS sample. It is important to highlight that this approach may face some limitations such as the presence of texture, a common characteristic of sheet metal, and the formation of amorphous phases. The latter have been reported by Allély et al. [7] as a characteristic of the corrosion products in PHS samples under SST conditions.

## 9.5 Conclusion

An approach was developed in order to monitor *in situ* the surface of AR and PHS samples exposed in chloride medium. The main findings of this feasibility study can be summarised as follows:

- i. Synchrotron X-ray diffraction worked as a principle to monitor *in situ* the surface condition of the samples exposed to an electrolyte.
- ii. A computer programme based on Python language was developed and used to index the patterns.
- iii. The indexed results were correlated with previous data related to Al-Fe-Si system.
- iv. The ternary intermetallic phases  $\tau_5$  and  $\tau_6$  were suggested as the most suitable for the AR system whereas  $\theta$ ,  $\eta$  and  $\tau_6$  may compose the PHS coating layer.
- v. In addition to the ternary intermetallic phases, a mixture of oxides was identified in both AR and PHS samples. Cristobalite, bayerite and hematite were found in AR condition whereas for PHS the predominance of Fe-based compounds were seen: hematite, magnetite, goethite, lepidocrocite and akaganeite.

## **Part III**

### Conclusion and outlook

## CHAPTER 10 - Conclusion and outlook

### 10.1 Conclusion

The application of press-hardened steel in vehicle structures has as premise that the total vehicle weight can be reduced as well as safety can be improved. Therefore, it is a strategic material for the automotive industry. This steel is usually protected with coatings to avoid both oxidation and decarburisation. The former decreases painting adhesion and causes premature damage on the stamping tools. The decarburisation affects the final mechanical properties of the components. These two phenomena justify the need for coating's application prior hot stamping in structural vehicle components. Among the coating systems, the hot-dip Al-Si has been widespread used for hot-stamping applications. However, there was a lack of understanding the corrosion resistance of the system after hot stamping. Hence, this research had as its main objective the evaluation of the hot-stamping effect on the electrochemical behaviour of 22MnB5 steel coated with hot-dip Al-Si (Si 10% in mass fraction). The main findings can be related regarding morphology, electrochemical behaviour and corrosion mechanism, as presented in Figure 10.1, as well as summarised as follows:

- I. **Coating morphology and composition:** The initial structure of the Al-Si coating changes into a multi-layered structure either enriched in Al or in Fe/Si. Moreover, the primary precipitates presented in the as-received condition (AR-before hot stamping) are no longer seen in the PHS condition (after hot stamping). The austenitisation step promotes the partial melting of the coating layer and enhances the diffusion among the elements; mostly iron, silicon and aluminium. The primary precipitates, which remain in solid state, become enriched mainly in iron and they are rearranged in sublayers. The higher austenitisation temperature, the thicker thickness of the sublayers enriched in Fe/Si. The hot stamping causes the formation of voids and micro cracks in the coating. The former is due to the fast diffusion, while the latter is related to the thermal expansion. Cracks are also seen at the surface. However, due to their preferential direction, they can be attributed to the mechanical load (forming step). The surface roughness is related to the formation of Al-Fe phases.

Moreover, the diffusion of iron and silicon towards the surface enhances the formation of a mixture of oxides which provide an extra protection barrier.

- II. **Electrochemical behaviour:** The corrosion potential, in chloride media, shifts towards nobler values after hot stamping. The increment of the corrosion potential can be related to the iron enrichment of the coating and the formation of a thermal oxide layer in PHS, which is thicker than the native oxide layer in AR condition. The anodic polarisation curves, recorded after *OCP*, show that the corrosion potential becomes nobler after hot stamping and the current density in the anodic branch increases relatively slower, due to the presence of Fe/Si-rich sublayers. Furthermore, different austenitisation temperatures result in a small variation of the corrosion potential. However, the higher austenitisation temperature, the higher corrosion potential.

The local electrochemical analyses were carried out in the samples' cross-sections. This approach was chosen to simulate the steel substrate exposure and then evaluate the protection mechanism provided by the coating. Scanning Kelvin probe force microscopy (SKPFM) measurements showed that the steel substrate is nobler than the coating layer in both AR and PHS conditions. However, the Volta-potential difference between the coating and the steel greatly decreases after hot stamping. Consequently, the thermo-mechanical process diminishes the driving force for cathodic protection. Moreover, the Volta-potential difference among the sublayers in the PHS varies according to the austenitisation temperature. Therefore, the higher austenitisation temperature, the lower Volta-potential difference among the sublayers. Nevertheless, the Al-rich sublayers shows lower Volta potential versus the Fe/Si-rich sublayers and the interdiffusion layer. This indicates that they could play a role of sacrificial anode to the nobler sublayers and the steel substrate. The coating layer ennoblement after hot stamping is not the only reason why the driving force for cathodic protection is affected; the thermo-mechanical process has also an influence on the Volta potential of the steel substrate. Initially the steel shows a ferrite-pearlite microstructure which changes into martensite after quenching in the stamping tool. This microstructure transformation increases in approximately 50 mV the Volta potential. The ennoblement of martensite

transformation can be mostly attributed to the residual stress, which alters the Volta potential.

The SKPFM results provided insights into the behaviour of the galvanic coupling (steel/coating) in its ambient condition, in the absence of an electrolyte. Thus, local electrochemical micro-cell measurements were carried out, using a depth-profile approach, to evaluate the influence of the electrolyte in this system. The results showed a predominant passive behaviour in the AR sample; only the steel substrate presented an active behaviour in  $0.1 \text{ mol L}^{-1} \text{ NaCl}$ . Before hot stamping, the surface could provide barrier protection to the free aluminium layer, due to the formation of a passive native oxide layer. The presence of cathodic precipitates in the free layer contributes to the high localised corrosion susceptibility and breakdown of the passive layer at low potentials. Moreover, due to its lowest corrosion potential, the free layer could provide cathodic protection to the upper interdiffusion layer, presenting the lowest corrosion rate. Although the UIDL is less noble than the steel substrate, it would protect the steel mainly by means of barrier mechanism due to the small potential difference between the steel substrate and the upper interdiffusion layer.

After hot stamping, the surface, the Fe/Si-rich sublayer, and the IDL presented a passive behaviour. On the other hand, the Al-rich sublayers showed either passive or active behaviour. Even the steel substrate presented a small passive range in some measurements. These observations indicate that care must be taken in order to establish the predominant behaviour of each sublayer. The active behaviour in Al-rich sublayer is justified by both high iron content and the presence of micro cracks whereas the steel substrate has an active behaviour in chloride media. Nonetheless, the passive behaviour could be related to the thickening of the oxide layer at the bottom of the crater where the electrochemical micro cell is placed. The overall corrosion potential of the coating layer increased and the potential difference among the sublayers decreased. The ennoblement of the surface's corrosion potential was attributed to the formation of a thermal oxide layer. The Al-rich could act as sacrificial anode to the Fe/Si-rich sublayer, due to their low corrosion potential and highest corrosion rate. Silicon was attributed as the reason for the highest corrosion and breakdown potential of the Fe/Si-rich layer. The IDL presented corrosion potential similar as the surface, though, less noble than the Fe/Si-rich sublayer.

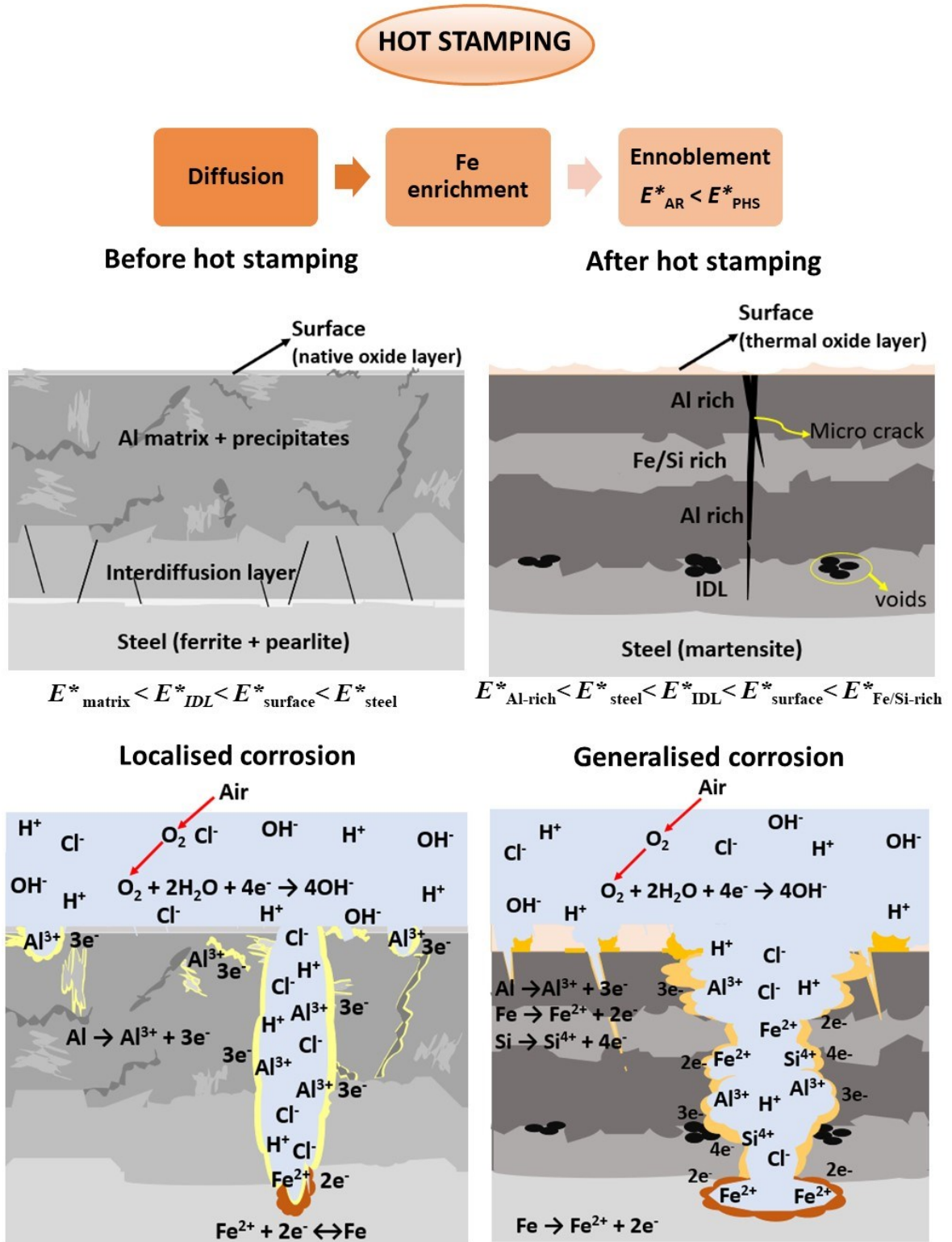
The hot stamping did not change the electrochemical behaviour of the steel substrate. However, as it changed the electrochemical behaviour of the coating layer, the steel substrate was no longer the noblest in the galvanic series. Thus, the steel can be protected only by barrier protection. Moreover, in case of damage and steel substrate exposure it will be corroded at very similar potentials as the Al-rich phases.

- III. **Corrosion mechanism:** The continuous salt spray test (SST) confirmed the trend suggested by the immersion tests in which the AR sample corrodes locally and the PHS presents a general corrosion. The corrosion mechanism of the system (coating/steel) changes from localised into generalised. The presence of red rust at the PHS surface from the early stages under SST conditions is mainly related to the high iron content present in it. However, damages in the coating (cracks and voids) enhance the corrosion in the coating layer. In agreement with the local electrochemical measurements, the preferential attack occurs in the Al-rich sublayers. However, as the driving force for cathodic protection is minimal, the whole coating layer is corroded, exposing the steel substrate. Therefore, the poor corrosion resistance presented under SST condition is mostly related to the defects inherent to the thermo-mechanical process. The nature of the corrosion products also changes due to the hot stamping. The presence of bayerite ( $\alpha$ -Al(OH)<sub>3</sub>) is predominant in the AR condition whereas in PHS magnetite (Fe<sub>3</sub>O<sub>4</sub>), goethite ( $\alpha$ -FeOOH), lepidocrocite ( $\gamma$ -FeOOH), akaganeite ( $\beta$ -FeOOH) and hematite ( $\alpha$ -Fe<sub>2</sub>O<sub>3</sub>) can be found. Silicon oxide (cristobalite) is present in both sample conditions.
- IV. **Synchrotron X-ray diffraction:** The suggested approach based on the use of synchrotron X-ray diffraction to monitor the dynamic changes in the phases present in the Al-Si coating, either before or after hot stamping, indicates that the method works as a principle. Further and dedicated research is necessary to understand the changes in the diffraction patterns. Nevertheless, it was possible to index the data using a developed computer programme in Python language. These results brought important insights about the intermetallic phases. The ternary intermetallic phases  $\tau_5$  and  $\tau_6$  were suggested as the most suitable for the

AR system whereas  $\theta$ ,  $\eta$  and  $\tau_6$  may compose the coating layer of an industrial PHS sample.

Finally, the most important observation taken from this investigation is that the hot stamping process alters the Al-Si coating morphology as well as its corrosion properties. The corrosion mechanism changes from localised into generalised. The coating layer becomes nobler, which greatly decreases the driving force for cathodic protection. Although the Al-rich sublayers could play a role of sacrificial anode, the steel substrate is mostly protected by barrier protection by the sublayers enriched in iron.

Figure 10.1 - Overview of the main findings related to the effect of hot stamping on the Al-Si coating structure-composition and the consequent effect on the corrosion properties



Source: Author

## 10.2 Outlook

This doctorate thesis presents a detailed evaluation of the effect of hot stamping process on the 22MnB5 steel coated with Al-Si linking the changes on coating's morphology with the electrochemical behaviour. However, this research has risen some discussion which could be further investigated, as following suggested:

- i. A carefully study about the growth of the thermal oxide layer by changing process parameters. The oxide layer could be characterised by means of X-ray photoelectron spectroscopy (XPS), grazing incidence X-ray diffraction and transmission electron microscopy (TEM).
- ii. To have a better characterisation of the different possible steps (i.e., passivation, activation, estimation of the polarisation rate of the contributing reactions, mass transfer) that contribute to an electrochemical system, one might consider applying non-stationary methods, such as electrochemical impedance spectroscopy (EIS). Even in these systems, as local corrosion is happening, local electrochemical impedance spectroscopy (LEIS) might be applied. Additionally, odd-random phase multisine EIS, which was developed at VUB, would allow us to better consider the non-stationarities inherent present in a localised corrosion system than using conventional single-sine EIS.

Within this thesis, the application of odd-random phase (ORP) multisine EIS was initially considered. However, it was decided not to start with this method in the progress of the thesis due to the high complexity of the systems, as seen in the local polarisation curves taken by the electrochemical micro-cell as function of depth in the crater of the GDOES. Considering the knowledge gained and the current information available, the use of ORP-EIS is suggested as a next step as it might lead to better separation of the different contributing factors.

- iii. A dedicated investigation about the effect of Si in the passivity of the Fe/Si-rich sublayers and interdiffusion layer.
- iv. Evaluation of the mechanical properties for the samples heated at different austenitisation temperatures. This approach could provide insights about the

best process parameters in order to combine high driving force for cathodic protection and high mechanical strength.

- v. Influence of surface treatments, for instance conversion treatments, on the corrosion resistance of PHS.
- vi. Investigation of the galvanic couple formed between coated PHS with dissimilar materials.
- vii. Influence of joining process on the corrosion resistance of PHS coated with Al-Si. This could include different welding processes and the evaluation of the bonding interactions between coated PHS and adhesives used in automotive industry.
- viii. Improvements on the *in-situ* approach using synchrotron X-ray diffraction to evaluate the effect of hot stamping on the corrosive process of the system, in which electrochemical measurements could be combined.

## References

- [1] C.R. Vaz, T.R. Shoeninger Rauen, Á.G. Rojas Lezana, Sustainability and innovation in the Automotive Sector: a structured content analysis, *Sustainability*. 9 (2017) 880. <https://doi.org/10.3390/su9060880>.
- [2] A.E. Tekkaya, N. Ben Khalifa, G. Grzancic, R. Hölker, Forming of lightweight metal components: need for new technologies, *Procedia Eng.* 81 (2014) 28-37. <https://doi.org/10.1016/j.proeng.2014.09.125>.
- [3] K. Kumar Dama, V. Suresh Babu, R.N. Rao, State of the art on automotive lightweight body-in-white design, *Mater. Today Proc.* 5 (2018) 20966-20971. <https://doi.org/10.1016/j.matpr.2018.06.486>.
- [4] M. Tisza, I. Czinege, Comparative study of the application of steels and aluminium in lightweight production of automotive parts, *Int. J. Light. Mater. Manuf.* 1 (2018) 229-238. <https://doi.org/10.1016/j.ijlmm.2018.09.001>.
- [5] World Health Organization, Road traffic injuries, (2020) 1-6. <https://www.who.int/news-room/fact-sheets/detail/road-traffic-injuries>.
- [6] H. Karbasian, A.E. Tekkaya, A review on hot stamping, *J. Mater. Process. Technol.* 210 (2010) 2103-2118. <https://doi.org/10.1016/j.jmatprotec.2010.07.019>.
- [7] C. Allély, L. Dosdat, O. Clauzeau, K. Ogle, P. Volovitch, Anticorrosion mechanisms of aluminized steel for hot stamping, *Surf. Coatings Technol.* 238 (2014) 188-196. <https://doi.org/10.1016/j.surfcoat.2013.10.072>.
- [8] M. Windmann, A. Röttger, W. Theisen, Phase formation at the interface between a boron alloyed steel substrate and an Al-rich coating, *Surf. Coatings Technol.* 226 (2013) 130-139. <https://doi.org/10.1016/j.surfcoat.2013.03.045>.
- [9] G. Venturato, M. Novella, S. Bruschi, A. Ghiotti, R. Shivpuri, Effects of phase transformation in hot stamping of 22MnB5 high strength steel, *Procedia Eng.* 183 (2017) 316-321. <https://doi.org/10.1016/j.proeng.2017.04.045>.
- [10] M. Merklein, J. Lechler, Investigation of the thermo-mechanical properties of hot stamping steels, *J. Mater. Process. Technol.* 177 (2006) 452-455. <https://doi.org/10.1016/j.jmatprotec.2006.03.233>.
- [11] L. Dosdat, J. Petitjean, T. Vietoris, O. Clauzeau, Corrosion resistance of different metallic coatings on press-hardened steels for automotive, *Steel Res. Int.* 82 (2011) 726-733. <https://doi.org/10.1002/srin.201000291>.
- [12] J. Kondratiuk, P. Kuhn, E. Labrenz, C. Bischoff, Zinc coatings for hot sheet metal forming: Comparison of phase evolution and microstructure during heat treatment, *Surf. Coatings Technol.* 205 (2011) 4141-4153. <https://doi.org/10.1016/j.surfcoat.2011.03.002>.
- [13] R. Neugebauer, F. Schieck, S. Polster, A. Mosel, A. Rautenstrauch, J. Schönherr, N. Pierschel, Press hardening - an innovative and challenging technology, *Arch. Civ. Mech. Eng.* 12 (2012) 113-118. <https://doi.org/10.1016/j.acme.2012.04.013>.
- [14] K. Mori, P.F. Bariani, B.-A. Behrens, A. Brosius, S. Bruschi, T. Maeno, M. Merklein, J. Yanagimoto, Hot stamping of ultra-high strength steel parts, *CIRP Ann.* 66 (2017) 755-777. <https://doi.org/10.1016/j.cirp.2017.05.007>.
- [15] D.W. Fan, H.S. Kim, B.C. De Cooman, A Review of the physical metallurgy related to the hot press forming of advanced high strength steel, *Mater. Technol.* 80 (2009) 218-222. <https://doi.org/10.2374/SRI08SP131>.
- [16] D.W. Fan, B.C. De Cooman, State-of-the-knowledge on coating systems for hot stamped parts, *Steel Res. Int.* 83 (2012) 412-433. <https://doi.org/10.1002/srin.201100292>.

- [17] A. Naganathan, L. Penter, Hot stamping, in: *Sheet Met. Forming-Processes Appl.*, ASM International, Chapter 7 (2010)133-142.
- [18] D.W. Fan, H.S. Kim, S. Biroasca, B.C. De Cooman, Critical review of hot stamping technology for automotive steels, *Mater. Sci. Technol.* (2007) 99-110.
- [19] M. Windmann, A. Röttger, W. Theisen, Formation of intermetallic phases in Al-coated hot-stamped 22MnB5 sheets in terms of coating thickness and Si content, *Surf. Coatings Technol.* 246 (2014) 17-25. <https://doi.org/10.1016/j.surfcoat.2014.02.056>.
- [20] H. Järvinen, M. Isakov, T. Nyssönen, M. Järvenpää, P. Peura, The effect of initial microstructure on the final properties of press hardened 22MnB5 steels, *Mater. Sci. Eng. A.* 676 (2016) 109-120. <https://doi.org/10.1016/j.msea.2016.08.096>.
- [21] L. Cho, H. Kang, C. Lee, B.C. De Cooman, Microstructure of liquid metal embrittlement cracks on Zn-coated 22MnB5 press-hardened steel, *Scr. Mater.* 90 (2014) 25–28. <https://doi.org/10.1016/j.scriptamat.2014.07.008>.
- [22] C. Palm, R. Vollmer, J. Aspacher, M. Gharbi, Increasing performance of Hot Stamping systems, *Procedia Eng.* 207 (2017) 765-770. <https://doi.org/10.1016/J.PROENG.2017.10.826>.
- [23] K. Bachman, Hot-stamped parts in 2019 vehicles, *Stamp. J.* (2018) 1-9. <https://www.thefabricator.com/stampingjournal/article/stamping/hot-stamped-parts-in-2019-vehicles> (accessed March 29, 2021).
- [24] D.W. Fan, H.S. Kim, J.-K. Oh, K.-G. Chin, B.C. De Cooman, Coating degradation in hot press forming, *ISIJ Int.* 50 (2010) 561-568. <https://doi.org/10.2355/isijinternational.50.561>.
- [25] Z. Panossian, L. Mariaca, M. Morcillo, S. Flores, J. Rocha, J.J. Peña, F. Herrera, F. Corvo, M. Sanchez, O.T. Rincon, G. Priddybailo, J. Simancas, Steel cathodic protection afforded by zinc, aluminium and zinc/aluminium alloy coatings in the atmosphere, *Surf. Coatings Technol.* 190 (2005) 244-248. <https://doi.org/10.1016/j.surfcoat.2004.04.023>.
- [26] R. Autengruber, G. Luckeneder, A.W. Hassel, Corrosion of press-hardened galvanized steel, *Corros. Sci.* 63 (2012) 12-19. <https://doi.org/10.1016/j.corsci.2012.04.048>.
- [27] V. Gentil, *Corrosion*, 3rd ed., LTC, Rio de Janeiro, 1996. (In Portuguese).
- [28] M. G. Fontana, *Corrosion engineering* 3rd ed., McGraw-Hill Series in Materials Science and Engineering, 2005.
- [29] S. Wolyneec, *Electrochemical techniques for corrosion*, 1<sup>st</sup> ed., EDUSP, São Paulo, 2003. (In Portuguese).
- [30] J. S.D. Cramer and B. S. Covino, *Corrosion: fundamentals, testing and protection*, 13 A, ASM International, 2003.
- [31] I. De Graeve, I. Schoukens, A. Lanzutti, F. Andreatta, A. Alvarez-Pampliega, J. De Strycker, L. Fedrizzi, H. Terry, Mechanism of corrosion protection of hot-dip aluminium-silicon coatings on steel studied by electrochemical depth profiling, *Corros. Sci.* 76 (2013) 325-336. <https://doi.org/10.1016/j.corsci.2013.07.005>.
- [32] I. Schoukens, I. Vandendael, J. De Strycker, A.A. Saleh, H. Terry, I. De Graeve, Effect of surface composition and microstructure of aluminised steel on the formation of a titanium-based conversion layer, *Surf. Coatings Technol.* 235 (2013) 628-636. <https://doi.org/10.1016/J.SURFCOAT.2013.08.041>.
- [33] B. Lemmens, H. Springer, I. De Graeve, J. De Strycker, D. Raabe, K. Verbeken, Effect of silicon on the microstructure and growth kinetics of intermetallic phases formed during hot-dip aluminizing of ferritic steel, *Surf. Coatings Technol.* 319 (2017) 104-109. <https://doi.org/10.1016/j.surfcoat.2017.03.040>.
- [34] W.K. Liang, W.J. Tao, B. Zhu, Y.S. Zhang, Influence of heating parameters on

- properties of the Al-Si coating applied to hot stamping, *Sci. China Technol. Sci.* 60 (2017) 1088-1102. <https://doi.org/10.1007/s11431-016-0231-y>.
- [35] I. Yakubtsov, R. Sohmshetty, Evolution of Al-Si Coating Microstructure during heat-treatment of Usibor ® 1500, *IOP Conf. Ser. Mater. Sci. Eng.* 418 (2018) 012015. <https://doi.org/10.1088/1757-899X/418/1/012015>.
- [36] W. Yang, E. Hwang, H. Kim, S. Ahn, S. Kim, H. Castaneda, A study of annealing time to surface characteristics and hydrogen embrittlement on AlSi coated 22MnB5 during hot stamping process, *Surf. Coatings Technol.* 378 (2019) 124911. <https://doi.org/10.1016/j.surfcoat.2019.124911>.
- [37] C.D. Horvath, *Advanced steels for lightweight automotive structures*, Woodhead Publishing Limited, 2010. <https://doi.org/10.1533/9781845697822.1.35>.
- [38] P. Schwingenschlögl, M. Merklein, Characterization of tribological conditions within direct hot stamping, *J. Mater. Process. Technol.* 278 (2020). <https://doi.org/10.1016/j.jmatprotec.2019.116535>.
- [39] Y. Nakagawa, K.I. Mori, S. Yashima, T. Kaido, Springback behaviour and quenchability in hot stamping of thick sheets, *Procedia Manuf.* 15 (2018) 1071-1078. <https://doi.org/10.1016/j.promfg.2018.07.385>.
- [40] G. Davies, Design and material utilization, in: *Mater. Automob. Bodies*, Elsevier, 2012: pp. 17-91. <https://doi.org/10.1016/B978-0-08-096979-4.00002-5>.
- [41] H. Li, G. Sun, G. Li, Z. Gong, D. Liu, Q. Li, On twist springback in advanced high-strength steels, *Mater. Des.* 32 (2011) 3272-3279. <https://doi.org/10.1016/j.matdes.2011.02.035>.
- [42] R.H. Wagoner, H. Lim, M.-G. Lee, Advanced issues in springback, *Int. J. Plast.* 45 (2013) 3-20. <https://doi.org/10.1016/j.ijplas.2012.08.006>.
- [43] J. BAO, H. LIU, Z. XING, B. SONG, Y. YANG, -H Liu, -Z Xing, -B Song, -Y Yang, Springback of hot stamping and die quenching with ultra-high-strength boron steel, *Eng. Rev.* 33 (2013) 151-156.
- [44] W.D. Callister, D.G. Rethwisch, *Materials science and engineering: an introduction*, 9th ed., Wiley, 2013.
- [45] J. Tungtrongpaibroj, V. Uthaisangsuk, W. Bleck, Determination of yield behaviour of boron alloy steel at high temperature, *Journal of Metals, Mater. Miner.* 19 (2009) 29-38.
- [46] A.E. Tekkaya, H. Karbasian, W. Homberg, M. Kleiner, Thermo-mechanical coupled simulation of hot stamping components for process design, *Prod. Eng. Res. Dev.* 1 (2007) 85-89. <https://doi.org/10.1007/s11740-007-0025-9>.
- [47] M. Windmann, A. Röttger, I. Hahn, W. Theisen, Mechanical properties of AlXFeY intermetallics in Al-base coatings on steel 22MnB5 and resulting wear mechanisms at press-hardening tool steel surfaces, *Surf. Coatings Technol.* 321 (2017) 321-327. <https://doi.org/10.1016/j.surfcoat.2017.04.075>.
- [48] H. Järvinen, M. Honkanen, M. Patnamsetty, S. Järn, E. Heinonen, H. Jiang, P. Peura, Press hardening of zinc-coated boron steels: role of steel composition in the development of phase structures within coating and interface regions, *Surf. Coatings Technol.* 352 (2018) 378-391. <https://doi.org/10.1016/j.surfcoat.2018.08.040>.
- [49] B. Lemmens, Detailed evaluation and characterization of the intermetallic phases in hot-dip aluminized steel, *Doctoral Thesis*, Ghent University - Faculty of Engineering and Architecture, 2017.
- [50] B. Lemmens, Y. Gonzalez Garcia, B. Corlu, J. De Strycker, I. De Graeve, K. Verbeken, Study of the electrochemical behaviour of aluminized steel, *Surf. Coatings Technol.* 260 (2014) 34-38. <https://doi.org/10.1016/j.surfcoat.2014.06.064>.
- [51] W.J. Cheng, C.J. Wang, Microstructural evolution of intermetallic layer in hot-dipped

- aluminide mild steel with silicon addition, *Surf. Coatings Technol.* 205 (2011) 4726-4731. <https://doi.org/10.1016/j.surfcoat.2011.04.061>.
- [52] W.-J.J. Cheng, C.-J.J. Wang, Growth of intermetallic layer in the aluminide mild steel during hot-dipping, *Surf. Coatings Technol.* 204 (2009) 824-828. <https://doi.org/10.1016/j.surfcoat.2009.09.061>.
- [53] F.C. Yin, M.X. Zhao, Y.X. Liu, W. Han, Z. Li, Effect of Si on growth kinetics of intermetallic compounds during reaction between solid iron and molten aluminum, *Trans. Nonferrous Met. Soc. China (English Ed.)* 23 (2013) 556-561. [https://doi.org/10.1016/S1003-6326\(13\)62499-1](https://doi.org/10.1016/S1003-6326(13)62499-1).
- [54] B. Lemmens, H. Springer, M.J.J. Duarte, I. De Graeve, J. De Strycker, D. Raabe, K. Verbeken, Atom probe tomography of intermetallic phases and interfaces formed in dissimilar joining between Al alloys and steel, *Mater. Charact.* 120 (2016) 268-272. <https://doi.org/10.1016/j.matchar.2016.09.008>.
- [55] I. Schoukens, Electrochemical activity of a new generation of hot dip aluminium coatings on steel, Doctoral Thesis, Vrije Universiteit Brussel - Faculty of Engineering, 2013.
- [56] T. Maitra, S.P. Gupta, Intermetallic compound formation in Fe-Al-Si ternary system: Part II, *Mater. Charact.* 49 (2002) 293-311. [https://doi.org/10.1016/S1044-5803\(03\)00005-6](https://doi.org/10.1016/S1044-5803(03)00005-6).
- [57] S.P. Gupta, Intermetallic compound formation in Fe-Al-Si ternary system: Part I, *Mater. Charact.* 49 (2003) 269-291. [https://doi.org/10.1016/S1044-5803\(03\)00006-8](https://doi.org/10.1016/S1044-5803(03)00006-8).
- [58] G. Ghosh, Al-Fe-Si Ternary Phase Diagram Evaluation, MSI Eureka. (2013). <https://doi.org/10.1007/978-3-540-69761-9>.
- [59] A.Q. Vu, B. Vuillemin, R. Oltra, C. Allély, In situ investigation of sacrificial behaviour of hot dipped AlSi coating in sulphate and chloride solutions, *Corros. Sci.* 70 (2013) 112-118. <https://doi.org/10.1016/j.corsci.2013.01.018>.
- [60] Z.-X. Gui, K. Wang, Y.-S. Zhang, B. Zhu, Cracking and interfacial debonding of the Al-Si coating in hot stamping of pre-coated boron steel, *Appl. Surf. Sci.* 316 (2014) 595-603. <https://doi.org/10.1016/j.apsusc.2014.08.043>.
- [61] Arcelor Mittal, Steels for hot stamping -Usibor® and Ductibor®. [https://automotive.arcelormittal.com/products/flat/PHS/usibor\\_ductibo](https://automotive.arcelormittal.com/products/flat/PHS/usibor_ductibo).
- [62] Arcelor Mittal, Steels coated with Alusi ® aluminum- silicon alloy: specific applications. <https://automotive.arcelormittal.com/products/flat/coatings/alusi>.
- [63] J.I. Goldstein, D.E. Newbury, J.R. Michael, N.W.M. Ritchie, J.H.J. Scott, D.C. Joy, *Scanning Electron Microscopy and X-Ray Microanalysis*, 3rd ed., Springer New York, New York, NY, 2018. <https://doi.org/10.1007/978-1-4939-6676-9>.
- [64] M. Henini, Scanning electron microscopy: An introduction, *III-Vs Rev.* 13 (2000) 40-44. [https://doi.org/10.1016/S0961-1290\(00\)80006-X](https://doi.org/10.1016/S0961-1290(00)80006-X).
- [65] HORIBA, Glow Discharge Optical Emission Spectroscopy GDOES. [https://www.horiba.com/en\\_en/glow-discharge-optical-emission-spectroscopy/](https://www.horiba.com/en_en/glow-discharge-optical-emission-spectroscopy/).
- [66] G. Buytaert, Premendra, J.H.W. de Wit, L. Katgerman, B. Kernig, H.J. Brinkman, H. Terryn, Electrochemical investigation of rolled-in subsurface layers in commercially pure aluminium alloys with the micro-capillary cell technique, *Surf. Coatings Technol.* 201 (2007) 4553-4560. <https://doi.org/10.1016/j.surfcoat.2006.09.096>.
- [67] B.B. Rodriguez, J.M.C. Mol, B. Kernig, J. Hasenclever, H. Terryn, Influence of the surface activation and local pitting susceptibility on the AC-electrograining of aluminium alloys, *Corros. Sci.* 53 (2011) 930-938. <https://doi.org/10.1016/j.corsci.2010.11.020>.
- [68] F.N. Afshar, R. Ambat, C. Kwakernaak, J.H.W. De Wit, J.M.C. Mol, H. Terryn, Electrochemical depth profiling of multilayer metallic structures: an aluminum

- brazing sheet, *Electrochim. Acta.* 77 (2012) 285–293. <https://doi.org/10.1016/j.electacta.2012.06.023>.
- [69] H. Mitsutake, R.J. Poppi, M.C. Breitkreitz, Raman imaging spectroscopy: history, fundamentals and current of the technique, *J. Braz. Chem. Soc.* 30 (2019) 2243-2258. <https://doi.org/10.21577/0103-5053.20190116>.
- [70] P. Rostron, S. Gaber, D. Gaber, Raman Spectroscopy , Review, *Int. J. Eng. Tech. Res.* 6 (2016) 2454-4698.
- [71] P. Larkin, *Infrared and Raman Spectroscopy PRINCIPLES AND SPECTRAL INTERPRETATION*, Elsevier, 2018. <https://doi.org/10.1016/C2015-0-00806-1>.
- [72] Lightsource.org, Light source. <https://lightsources.org/>.
- [73] Center for Research in Energy and Materials, Synchrotron light. <https://www.lnls.cnpem.br/the-lnls/what-is-synchrotron-light/>.
- [74] B.D. Cullity, *Elements of X-ray diffraction*, 2nd ed., ADDISON-WESLEY PUBLISHING COMPANY INC, 1994.
- [75] C.M.A. Brett, A.M.O. Brett, *Electrochemistry principles, methods, and applications*, Oxford University Press, New York, NY, 1993.
- [76] J.O. Bockris, A.K.N. Reddy, *Modern Electrochemistry*, 2<sup>nd</sup> ed., KLUWER ACADEMIC PUBLISHERS, 1999.
- [77] E.P. da S. Pimenta, S. Goulart-Santos, Corrosion resistance of galvanized steels submitted to salt spray test, in: INTERCORR 2016, ABRACO, Búzios/RJ, 2016. (In Portuguese).
- [78] N. Lebozec, N. Blandin, D. Thierry, Accelerated corrosion tests in the automotive industry: A comparison of the performance towards cosmetic corrosion, *Mater. Corros.* 59 (2008) 889-894. <https://doi.org/10.1002/maco.200804168>.
- [79] R.L. Howard, S.B. Lyon, J.D. Scantlebury, Accelerated tests for the prediction of cut-edge corrosion of coil-coated architectural cladding Part I: cyclic cabinet salt spray, *Prog. Org. Coatings.* 37 (1999) 91-98. [https://doi.org/10.1016/S0300-9440\(99\)00060-0](https://doi.org/10.1016/S0300-9440(99)00060-0).
- [80] S. Fujita, H. Kajiyama, C. Kato, Assessment and application technologies for automotive materials (perforation) - techniques for corrosion resistance and perforation feedback for automotive steel materials - , *Jfe Tech. Rep.* 4 (2004) 9-16.
- [81] F. Andreatta, L. Fedrizzi, The use of the electrochemical micro-cell for the investigation of corrosion phenomena, *Electrochim. Acta.* 203 (2016) 337-349. <https://doi.org/10.1016/j.electacta.2016.01.099>.
- [82] H. Böhni, T. Suter, F. Assi, Micro-electrochemical techniques for studies of localized processes on metal surfaces in the nanometer range, *Surf. Coatings Technol.* 130 (2000) 80-86. [https://doi.org/10.1016/S0257-8972\(00\)00681-2](https://doi.org/10.1016/S0257-8972(00)00681-2).
- [83] T. Suter, H. Böhni, A new microelectrochemical method to study pit initiation on stainless steels, *Electrochim. Acta.* 42 (1997) 3275-3280. [https://doi.org/10.1016/S0013-4686\(70\)01783-8](https://doi.org/10.1016/S0013-4686(70)01783-8).
- [84] F. Andreatta, *Local Electrochemical Behaviour of 7Xxx Aluminium Alloys*, Doctoral Thesis, Delft University of Technology, 2004.
- [85] V. Guillaumin, P. Schmutz, G.S. Frankel, Characterization of corrosion interfaces by the scanning Kelvin probe force microscopy technique, *J. Electrochem. Soc.* 148 (2001) B163. <https://doi.org/10.1149/1.1359199>.
- [86] M. Rohwerder, F. Turcu, High-resolution Kelvin probe microscopy in corrosion science: Scanning Kelvin probe force microscopy (SKPFM) versus classical scanning Kelvin probe (SKP), *Electrochim. Acta.* 53 (2007) 290-299. <https://doi.org/10.1016/j.electacta.2007.03.016>.
- [87] C. Örnek, C. Leygraf, J. Pan, On the Volta potential measured by SKPFM -

- fundamental and practical aspects with relevance to corrosion science, *Corros. Eng. Sci. Technol.* 54 (2019) 185-198. <https://doi.org/10.1080/1478422X.2019.1583436>.
- [88] J.H. de Wit, Local potential measurements with the SKPFM on aluminium alloys, *Electrochim. Acta.* 49 (2004) 2841-2850. <https://doi.org/10.1016/j.electacta.2004.01.045>.
- [89] W. Li, M. Cai, Y. Wang, S. Yu, Influences of tensile strain and strain rate on the electron work function of metals and alloys, (2005). <https://doi.org/10.1016/j.scriptamat.2005.10.064>.
- [90] C. Örnek, D.L.L. Engelberg, SKPFM measured Volta potential correlated with strain localisation in microstructure to understand corrosion susceptibility of cold-rolled grade 2205 duplex stainless steel, *Corros. Sci.* 99 (2015) 164-171. <https://doi.org/10.1016/j.corsci.2015.06.035>.
- [91] Y. Jin, M. Liu, C. Zhang, C. Leygraf, L. Wen, J. Pan, First-principle calculation of volta potential of intermetallic particles in aluminum alloys and practical implications, *J. Electrochem. Soc.* 164 (2017) C465-C473. <https://doi.org/10.1149/2.0191709jes>.
- [92] P. Schmutz, G.S. Frankel, Characterization of AA2024-T3 by scanning Kelvin probe force microscopy, *J. Electrochem. Soc.* 145 (1998) 2285. <https://doi.org/10.1149/1.1838633>.
- [93] L. Lacroix, L. Ressler, C. Blanc, G. Mankowski, Statistical study of the corrosion behavior of Al<sub>2</sub>CuMg Intermetallics in AA2024-T351 by SKPFM, *J. Electrochem. Soc.* 155 (2008) C8. <https://doi.org/10.1149/1.2799089>.
- [94] L.E. Fratila-Apachitei, I. Apachitei, J. Duszczyk, Characterization of cast AlSi(Cu) alloys by scanning Kelvin probe force microscopy, *Electrochim. Acta.* 51 (2006) 5892-5896. <https://doi.org/10.1016/j.electacta.2006.03.027>.
- [95] R.I. Revilla, H. Terryn, I. De Graeve, On the use of SKPFM for in situ studies of the repassivation of the native oxide film on aluminium in air, *Electrochem. Commun.* 93 (2018) 162–165. <https://doi.org/10.1016/j.elecom.2018.07.010>.
- [96] A. Davoodi, Z. Esfahani, M. Sarvghad, Microstructure and corrosion characterization of the interfacial region in dissimilar friction stir welded AA5083 to AA7023, *Corros. Sci.* 107 (2016) 133-144. <https://doi.org/10.1016/j.corsci.2016.02.027>.
- [97] F. Norouzi Afshar, J.H.W. De Wit, H. Terryn, J.M.C. Mol, Kelvin probe force microscopy as a means of predicting the electrochemical characteristics of the surface of a modified AA4xxx/AA3xxx (Al alloys) brazing sheet, *Electrochim. Acta.* 88 (2013) 330-339. <https://doi.org/10.1016/j.electacta.2012.10.051>.
- [98] R.I. Revilla, J. Liang, S. Godet, I. De Graeve, Local Corrosion Behavior of Additive Manufactured AlSiMg Alloy Assessed by SEM and SKPFM, *J. Electrochem. Soc.* 164 (2017) C27-C35. <https://doi.org/10.1149/2.0461702jes>.
- [99] A. Alvarez-Pampliega, Y. González-García, K. Van den Bergh, J. De Strycker, H. Terryn, Scanning Kelvin force microscopy study at the cut-edge of aluminum rich metal coated steel, *Mater. Corros.* 66 (2015) 16-22. <https://doi.org/10.1002/maco.201307145>.
- [100] T. Suter, H. Böhni, Microelectrodes for corrosion studies in microsystems, *Electrochim. Acta.* 47 (2001) 191-199. [https://doi.org/10.1016/S0013-4686\(01\)00551-5](https://doi.org/10.1016/S0013-4686(01)00551-5).
- [101] A. Van Alboom, B. Lemmens, B. Breitbach, E. De Grave, S. Cottenier, K. Verbeken, Multi-method identification and characterization of the intermetallic surface layers of hot-dip Al-coated steel: FeAl<sub>3</sub> or Fe<sub>4</sub>Al<sub>13</sub> and Fe<sub>2</sub>Al<sub>5</sub> or Fe<sub>2</sub>Al<sub>5+x</sub>, *Surf. Coatings Technol.* 324 (2017) 419–428. <https://doi.org/10.1016/J.SURFCOAT.2017.05.091>.
- [102] Z.X. Gui, W.K. Liang, Y.S. Zhang, Formability of aluminum-silicon coated boron

- steel in hot stamping process, *Trans. Nonferrous Met. Soc. China (English Ed.)* 24 (2014) 1750-1757. [https://doi.org/10.1016/S1003-6326\(14\)63249-0](https://doi.org/10.1016/S1003-6326(14)63249-0).
- [103] Z. Gui, W. Liang, Y. Zhang, Enhancing ductility of the Al-Si coating on hot stamping steel by controlling the Fe-Al phase transformation during austenitization, *Sci. China Technol. Sci.* 57 (2014) 1785-1793. <https://doi.org/10.1007/s11431-014-5576-3>.
- [104] H. Springer, A. Kostka, E.J.J. Payton, D. Raabe, A. Kaysser-Pyzalla, G. Eggeler, On the formation and growth of intermetallic phases during interdiffusion between low-carbon steel and aluminum alloys, *Acta Mater.* 59 (2011) 1586-1600. <https://doi.org/10.1016/j.actamat.2010.11.023>.
- [105] Z. Esfahani, E. Rahimi, M. Sarvghad, A. Rafsanjani-Abbasi, A. Davoodi, Correlation between the histogram and power spectral density analysis of AFM and SKPFM images in an AA7023/AA5083 FSW joint, *J. Alloys Compd.* 744 (2018) 174-181. <https://doi.org/10.1016/j.jallcom.2018.02.106>.
- [106] M. Sarvghad-Moghaddam, R. Parvizi, A. Davoodi, M. Haddad-Sabzevar, A. Imani, Establishing a correlation between interfacial microstructures and corrosion initiation sites in Al/Cu joints by SEM-EDS and AFM-SKPFM, *Corros. Sci.* 79 (2014) 148-158. <https://doi.org/10.1016/j.corsci.2013.10.039>.
- [107] L.L. Shreir, R.A. Jarman, G.T. Burstein, *Corrosion*, 3rd ed., Elsevier, 1994. <https://doi.org/10.1016/C2009-0-24066-9>.
- [108] K.A. Yasakau, A.N. Salak, M.L. Zheludkevich, M.G.S.S. Ferreira, Volta potential of oxidized aluminum studied by scanning kelvin probe force microscopy, *J. Phys. Chem. C.* 114 (2010) 8474-8484. <https://doi.org/10.1021/jp1011044>.
- [109] P.P. Sarkar, P. Kumar, M.K. Manna, P.C. Chakraborti, Microstructural influence on the electrochemical corrosion behaviour of dual-phase steels in 3.5% NaCl solution, *Mater. Lett.* 59 (2005) 2488-2491. <https://doi.org/10.1016/j.matlet.2005.03.030>.
- [110] K. Fushimi, K. Yanagisawa, T. Nakanishi, Y. Hasegawa, T. Kawano, M. Kimura, Microelectrochemistry of dual-phase steel corroding in 0.1 M sulfuric acid, *Electrochim. Acta.* 114 (2013) 83-87. <https://doi.org/10.1016/j.electacta.2013.09.162>.
- [111] N. Sathirachinda, R. Pettersson, J. Pan, Depletion effects at phase boundaries in 2205 duplex stainless steel characterized with SKPFM and TEM/EDS, *Corros. Sci.* 51 (2009) 1850-1860. <https://doi.org/10.1016/j.corsci.2009.05.012>.
- [112] N. Sathirachinda, R. Pettersson, S. Wessman, J. Pan, Study of nobility of chromium nitrides in isothermally aged duplex stainless steels by using SKPFM and SEM/EDS, *Corros. Sci.* 52 (2010) 179-186. <https://doi.org/10.1016/j.corsci.2009.08.057>.
- [113] F. Andreatta, H. Terry, J.H. de Wit, Corrosion behaviour of different tempers of AA7075 aluminium alloy, *Electrochim. Acta.* 49 (2004) 2851-2862. <https://doi.org/10.1016/j.electacta.2004.01.046>.
- [114] N.L. Sukiman, X. Zhou, N. Birbilis, A.E. Hughes, J.M. C. Mol, S.J. Garcia, X. Zhou, G.E. Thompson, Durability and corrosion of aluminium and its alloys: overview, property space, techniques and developments, in: *Alum. Alloy. - New Trends Fabr. Appl.*, InTech, 2012. <https://doi.org/10.5772/53752>.
- [115] T. Nelis, R. Payling, N.W. Barneet, Qualitative depth profiling, in: T. Nelis, R. Payling, N.W. Barneet (Eds.), *Glow Disch. Opt. Emiss. Spectrosc.*, 2003: pp. 123-135. <https://doi.org/10.1039/9781847550989-00123>.
- [116] A.R. Lashin, O. Schneeweiss, Y. Houbaert, Effect of ambient air pressure on the oxidation kinetics of Fe-6 at.% Si alloy, *Corros. Sci.* 50 (2008) 2580-2587. <https://doi.org/10.1016/j.corsci.2008.06.036>.
- [117] Z. Gui, W. Liang, Y. Liu, Y. Zhang, Thermo-mechanical behavior of the Al-Si alloy coated hot stamping boron steel, *Mater. Des.* 60 (2014) 26-33. <https://doi.org/10.1016/J.MATDES.2014.03.011>.

- [118] Z. Panossian, C.A.L. dos Santos, J.L. Cardoso, L.N. da Silva, R.A. Camargo, Interpretation of polarization curves, in: ABRACO, ABRACO, Fortaleza/CE, 2014. (In Portuguese).
- [119] G. Baril, C. Blanc, M. Keddam, N. Pébère, Local Electrochemical Impedance Spectroscopy Applied to the Corrosion Behavior of an AZ91 Magnesium Alloy, *J. Electrochem. Soc.* 150 (2003) B488. <https://doi.org/10.1149/1.1602080>.
- [120] C.P. de Abreu, C.M. de Assis, P.H. Suegama, I. Costa, M. Keddam, H.G. de Melo, V. Vivier, Influence of probe size for local electrochemical impedance measurements, *Electrochim. Acta.* 233 (2017) 256-261. <https://doi.org/10.1016/j.electacta.2017.03.017>.
- [121] D.L.A. de Faria, S. Venâncio Silva, M.T. de Oliveira, Raman microspectroscopy of some iron oxides and oxyhydroxides, *J. Raman Spectrosc.* 28 (1997) 873-878. [https://doi.org/10.1002/\(SICI\)1097-4555\(199711\)28:11<873::AID-JRS177>3.3.CO;2-2](https://doi.org/10.1002/(SICI)1097-4555(199711)28:11<873::AID-JRS177>3.3.CO;2-2).
- [122] ASTM B117-19, Standard practice for operating salt spray (FOG) apparatus., ASTM International, West Conshohocken, 2019. <https://doi.org/10.1520/B0117-19>.
- [123] R.J. Thibreau, C.W. Brown, R.H. Heidersbach, Raman spectra of possible corrosion products of iron., *Appl. Spectrosc.* 32 (1978) 532-535. <https://doi.org/10.1366/000370278774330739>.
- [124] A.C.C. Scheinost, Metal oxides, in: *Encycl. Soils Environ.*, Elsevier, 2005: pp. 428-438. <https://doi.org/10.1016/B0-12-348530-4/00194-6>.
- [125] S.M. Cambier, D. Verreault, G.S. Frankel, Raman investigation of anodic undermining of coated steel during environmental exposure, *CORROSION.* 70 (2014) 1219-1229. <https://doi.org/10.5006/1358>.
- [126] N. Phambu, Characterization of aluminum hydroxide thin film on metallic aluminum powder, *Mater. Lett.* 57 (2003) 2907-2913. [https://doi.org/10.1016/S0167-577X\(02\)01395-2](https://doi.org/10.1016/S0167-577X(02)01395-2).
- [127] D.M. Popovic, V. Milosavljevic, A. Zekic, N. Romcevic, S. Daniels, Raman scattering analysis of silicon dioxide single crystal treated by direct current plasma discharge, *Appl. Phys. Lett.* 98 (2011) 13–16. <https://doi.org/10.1063/1.3543838>.
- [128] H.D. Ruan, R.L. Frost, J.T. Klopogge, Comparison of raman spectra in characterizing gibbsite, bayerite, diaspore and boehmite, *J. Raman Spectrosc.* 32 (2001) 745-750. <https://doi.org/10.1002/jrs.736>.
- [129] K.A. Rodgers, Routine identification of aluminium hydroxide polymorphs with the laser Raman microprobe, *Clay Miner.* 28 (1993) 85-99. <https://doi.org/10.1180/claymin.1993.028.1.08>.
- [130] L. Bellot-Gurlet, D. Neff, S. Réguer, J. Monnier, M. Saheb, P. Dillmann, Raman studies of corrosion layers formed on archaeological irons in various media, *J. Nano Res.* 8 (2009) 147-156. <https://doi.org/10.4028/www.scientific.net/JNanoR.8.147>.
- [131] S. Mohammed, M. Elnoor, I. Hamad, The structural properties of iron oxides using Raman spectroscopy, *J. Sci. Eng. Res.* 183 *J. Sci. Eng. Res.* 5 (2018) 183-187.
- [132] R.A. Antunes, R.U. Ichikawa, L.G. Martinez, I. Costa, Characterization of corrosion products on carbon steel exposed to natural weathering and to accelerated corrosion tests, *Int. J. Corros.* 2014 (2014) 1-9. <https://doi.org/10.1155/2014/419570>.
- [133] K. Dejun, W. Jinchun, Salt spray corrosion and electrochemical corrosion properties of anodic oxide film on 7475 aluminum alloy, *J. Alloys Compd.* 632 (2015) 286-290. <https://doi.org/10.1016/j.jallcom.2015.01.175>.
- [134] Schoen R, Roberson CE, Structures of aluminum hydroxide and geochemical implications, *Am. Mineral.* 55 (1970) 43-77.
- [135] M. Fleischmann, P.J. Hendra, J. Robinson, X-ray diffraction from adsorbed iodine on

- graphite, *Nature*. 288 (1980) 152-154. <https://doi.org/10.1038/288152a0>.
- [136] J. Robinson, F.C. Walsh, In situ synchrotron radiation X-ray techniques for studies of corrosion and protection, *Corros. Sci.* 35 (1993) 791-800. [https://doi.org/10.1016/0010-938X\(93\)90217-5](https://doi.org/10.1016/0010-938X(93)90217-5).
- [137] National Synchrotron Light Laboratory, XRD2 beamline an experimental station at LNLS. <https://www.lnls.cnpem.br/grupos/xrd2-en/>.
- [138] E. Ben-Jacob, P. Garik, The formation of patterns in non-equilibrium growth, *Nature*. 343 (1990) 523-530. <https://doi.org/10.1038/343523a0>.

## SUMMARY

The press-hardened steel (PHS) is a strategic material for the automotive industry. The application of this type of steel in the vehicle structure allows safety improvement, mass reduction and less fuel consumption. Due to its ultra-high tensile strength the PHS components are produced by means of hot-stamping process in order to avoid the springback effect. Hot stamping is a thermo-mechanical process in which the steel blank is heated at austenitisation temperatures and then, it is transferred to a press-tool where the material is formed and quenched simultaneously. The 22MnB5 steel is the main grade used for hot-stamping application due to its high hardenability which allows a fully martensitic transformation at the end of the process.

The non-controlled furnace atmosphere and the transfer step, during the hot stamping, cause deleterious oxidation and decarburisation of the steel. The former is critical for painting adhesion and may cause damage in the press tool whereas the latter influences on the final mechanical properties. Hence, the steel substrate is often protected with metallic coatings before hot stamping.

The hot-dip aluminium-silicon (Al-Si) has been the most applied metallic coating for hot-stamping applications. This system is well-known for its high corrosion and oxidation resistance at high temperatures. However, the present state of art, regarding the corrosion resistance of PHS coated with Al-Si, still shows some open questions. There are just a few works about the corrosion resistance of coated hot-stamped components, and they have been evaluated mostly by means of accelerated tests and standard electrochemical measurements. These methods only show the global behaviour of the system and they do not give any insights concerning the local electrochemical behaviour of the different sublayers of the coatings.

There is a need for a local investigation of these systems due to the high complexity of these multi-layered coatings, highlighted by the different compositions of the sublayers and the presence of defects (micro cracks and voids). For this reason, a detailed approach based on local electrochemical techniques was suggested. This work aimed at evaluating the effect of hot-stamping process on the electrochemical behaviour of 22MnB5 coated with hot-dip Al-Si (10 % Si in mass fraction). Both global and local electrochemical techniques were used including open circuit potential (*OCP*), linear sweep voltammetry (*LSV*), scanning Kelvin probe force microscopy (*SKPFM*), electrochemical micro cell and continuous accelerated corrosion salt spray test (*SST*). The coatings' morphologies either

before or after hot stamping were characterised by means of scanning electron microscopy (SEM) and the semi-quantitative elemental analyses were undertaken by means of energy dispersive X-ray spectroscopy (EDS). Finally, the corrosion products formed during SST were analysed by means of Raman spectroscopy.

During hot stamping, the austenitisation causes the partial melting of the coating and promotes the diffusion of the elements which compose the system (coating/steel). The whole coating layer becomes enriched in iron (even the top surface) and the coating morphology becomes a multi-layered system which consists of several sublayers enriched either in aluminium or iron/silicon. The latter becomes thicker as the austenitisation temperature increases. Moreover, defects inherent to the thermo-mechanical process, such as voids and micro cracks, are also more pronounced at higher austenitisation temperatures.

The changes on coating structure influence on the electrochemical behaviour of the system. Global electrochemical measurements showed the ennoblement of the system after hot stamping. The SKPFM enables the measurement of the Volta potential of each sublayer in the system without the influence of an electrolyte. The SKPFM results showed that both coating layer and steel substrate becomes nobler after hot stamping. The former is related to the iron enrichment while the latter is a consequence of the microstructural transformation. Additionally, a small Volta-potential difference was seen among the sublayers in the coating and a great decrease on drive force for cathodic protection was seen after hot stamping. The drive force for cathodic protection is influenced by the austenitisation temperature. It was shown that the Volta-potential difference between steel substrate and coating layer decreases as the austenitisation temperature increases.

Local electrochemical micro-cell measurements were carried out, using a depth-profile approach, to evaluate the influence of the electrolyte in each sublayer of the system. The results indicated that before hot stamping all the sublayers of the coating presented a passive behaviour. However, after hot stamping the Al-rich sublayers displayed a predominant active behaviour, being the less noble phase of the system. However, the Fe/Si-rich sublayers and the interdiffusion layer showed only a passive behaviour which can be attributed to the high silicon content. The Fe/Si-rich sublayers were characterised as the noblest phase in the system. Nevertheless, the whole system shifted the corrosion potential to nobler values after hot stamping. The steel substrate was an exception as it showed the same predominant active behaviour, similar corrosion potential and high current density as before hot stamping. In chloride media, if damage exposes the steel substrate it will corrode as much as the Al-rich sublayers. The corrosion mechanism also changed after the thermo-

mechanical process from localised into generalised. This is related to the absence of cathodic precipitates at the coating surface after hot stamping. However, the PHS sample presented a poor corrosion resistance under SST conditions which may be mostly correlated to the presence of defects formed during hot stamping. Nonetheless, in accordance with the electrochemical results, the Al-rich sublayers were attacked preferentially, and the steel exposure resulted in its corrosion as the driving force for cathodic protection is small. Additionally, the nature of corrosion products also changed: prior hot stamping, either silicon oxides or bayerite ( $\alpha$ -Al(OH)<sub>3</sub>) were found as corrosion product; but in PHS samples after SST, mainly iron-based compounds were identified, including magnetite (Fe<sub>3</sub>O<sub>4</sub>), goethite ( $\alpha$ -FeOOH), lepidocrocite ( $\gamma$ -FeOOH), akaganeite ( $\beta$ -FeOOH) and silicon oxides. The presence of hematite ( $\alpha$ -Fe<sub>2</sub>O<sub>3</sub>) was related to the laser intensity.

This doctorate thesis also included a feasibility study which aimed the *in-situ* monitoring of crystalline phase present at the samples' surface, before and after hot stamping, in a chloride medium using synchrotron X-ray diffraction. The suggested approach worked as a principle. Moreover, results brought important insights about the presence of intermetallic phases in the Al-Si coating, either before or after hot stamping, and their dynamic of transformation in which they are highly dependent of the initial conditions of the solid/liquid state at the beginning of both hot dip and hot-stamping processes.

Finally, the most important observation taken from this investigation is that the hot stamping process alters the Al-Si coating morphology and as well as its corrosion properties. The coating layer becomes nobler, but it greatly decreases the driving force for cathodic protection. Although the Al-rich sublayers could play a role of sacrificial anode, the steel substrate is mostly protected by barrier protection by the sublayers enriched in iron.

Keywords: hot stamping, hot-dip aluminium-silicon, electrochemical behaviour

## RESUMO EXPANDIDO

O aço endurecido por prensagem (PHS - do inglês, *press-hardened steel*) é um material estratégico para a indústria automotiva. A aplicação desse tipo de aço na estrutura do veículo permite melhoria da segurança, redução de massa e menor consumo de combustível. Devido a sua ultra-alta resistência à tração os componentes de PHS são produzidos por meio do processo de estampagem a quente para evitar o efeito mola. A estampagem a quente é um processo termo-mecânico no qual o blanque de aço é aquecido a temperaturas de austenitização e então, o blanque é transferido do forno para um ferramenta de prensagem onde o material é conformado e temperado simultaneamente. O aço 22MnB5 é a principal classe usada para aplicações de estampagem a quente devido a sua alta temperabilidade que permite total transformação martensítica ao final do processo.

A atmosfera não controlada do forno e a etapa de transferência para a prensa, durante a estampagem a quente, causam oxidação prejudicial e descarbonetação do aço. O primeiro é crítico para a aderência da pintura e pode causar danos na ferramenta de prensagem, enquanto o último influencia nas propriedades mecânicas finais. Portanto, o substrato de aço é frequentemente protegido com revestimentos metálicos antes da estampagem a quente.

O alumínio-silício por imersão a quente (Al-Si) tem sido o revestimento metálico mais difundido para aplicações de estampagem a quente. Este sistema é conhecido por sua alta resistência à corrosão e oxidação em altas temperaturas. No entanto, o estado da arte atual, com relação à resistência à corrosão do PHS revestido com Al-Si, ainda apresenta algumas questões em aberto. Existem apenas alguns trabalhos sobre a resistência à corrosão de componentes estampados a quente revestidos, e eles foram avaliados principalmente por meio de testes acelerados e medições eletroquímicas padrão. Esses métodos mostram apenas o comportamento global do sistema e não fornecem informações sobre o comportamento eletroquímico local das diferentes subcamadas dos revestimentos.

Existe a necessidade de uma investigação local desses sistemas devido à alta complexidade desses revestimentos, constituído por multicamadas, destacada pelas diferentes composições das subcamadas e pela presença de defeitos (microfissuras e vazios). Por esta razão, uma abordagem detalhada baseada em técnicas eletroquímicas locais foi sugerida. Este trabalho teve como objetivo avaliar o efeito do processo de estampagem a quente no comportamento eletroquímico do aço 22MnB5 revestido com Al-Si (10 % Si em fração de massa) por imersão a quente. Técnicas eletroquímicas globais e localizadas foram

utilizadas incluindo o potencial de circuito aberto (*OCP*- do inglês, *open circuit potential*), voltametria de varredura linear (*LSV*- do inglês, *linear sweep voltammetry*), microscopia de varredura de força por sonda Kelvin (*SKPFM* - do inglês, *scanning Kelvin probe force microscopy*), microcélula eletroquímica e teste contínuo de corrosão acelerada em câmara de névoa salina (*SST*- do inglês, *salt spray test*). As morfologias dos revestimentos, antes ou depois da estampagem a quente, foram caracterizadas por meio de microscopia eletrônica de varredura (*MEV*) e as análises elementares semiquantitativas foram realizadas por meio de espectroscopia de energia dispersiva de raios X (*EDS*- do inglês, *energy dispersive X-rays spectroscopy*). Finalmente, os produtos de corrosão formados durante o *SST* foram analisados por meio de espectroscopia Raman.

Durante a estampagem a quente, a austenitização causa fusão parcial do revestimento e promove a difusão dos elementos que consistem no sistema (revestimento/aço). A camada do revestimento se torna enriquecida em ferro (até mesmo a superfície) e a morfologia do revestimento se torna um sistema de multicamadas que consiste em diferentes subcamadas enriquecidas em alumínio ou ferro/silício. Esta última torna-se mais espessa à medida que a temperatura de austenitização aumenta. Além disso, defeitos inerentes ao processo termo-mecânico, como vazios e microfissuras, também são mais pronunciados em temperaturas de austenitização mais altas.

As mudanças na estrutura do revestimento influenciam o comportamento eletroquímico do sistema. Medidas eletroquímicas globais mostraram o enobrecimento do sistema depois da estampagem a quente. O *SKPFM* permite a medida do potencial Volta de cada subcamada do sistema sem a influência de um eletrólito. Os resultados de *SKPFM* mostraram que a camada de revestimento e o aço tornam-se mais nobres depois da estampagem a quente. O primeiro é relacionado ao enriquecimento em ferro enquanto o último é uma consequência da transformação microestrutural. Além disso, uma pequena diferença de potencial Volta foi vista entre as subcamadas no revestimento e uma grande diminuição na força motriz para proteção catódica foi observada depois da estampagem a quente. A força motriz para proteção catódica é influenciada pela temperatura de austenitização. Foi mostrado que a diferença de potencial Volta entre o aço e a camada de revestimento diminui à medida que a temperatura de austenitização aumenta.

Medições eletroquímicas locais de microcélulas foram realizadas, usando uma abordagem de perfil de profundidade, para avaliar a influência do eletrólito em cada subcamada do sistema. Os resultados indicaram que antes da estampagem a quente todas as subcamadas do revestimento apresentaram comportamento passivo. No entanto, após a

estampagem a quente, as subcamadas ricas em Al apresentaram um comportamento ativo predominante, sendo a fase menos nobre do sistema. Por outro lado, as subcamadas ricas em Fe/Si e a camada de interdifusão apresentaram apenas um comportamento passivo que pode ser atribuído ao alto teor de silício. As subcamadas ricas em Fe/Si foram caracterizadas como a fase mais nobre do sistema. No entanto, o potencial de corrosão de todo o sistema foi alterado para valores mais nobres após a estampagem a quente. O substrato de aço foi uma exceção, pois apresentou o mesmo comportamento ativo predominante, além do potencial de corrosão semelhante e alta densidade de corrente de antes da estampagem a quente. Em meios de cloreto, se o dano expor o substrato de aço, ele corroerá tanto quanto as subcamadas ricas em Al. O mecanismo de corrosão também mudou após o processo termo-mecânico de localizado para generalizado. Isso está relacionado à ausência de precipitados catódicos na superfície do revestimento após a estampagem a quente. No entanto, a amostra de PHS apresentou uma pobre resistência à corrosão em condições de SST, o que pode estar relacionado principalmente à presença de defeitos formados durante a estampagem a quente. No entanto, de acordo com os resultados eletroquímicos, as subcamadas ricas em Al foram atacadas preferencialmente e a exposição do aço resultou em sua corrosão, pois a força motriz para proteção catódica é pequena. Além disso, a natureza dos produtos de corrosão também mudou: antes da estampagem a quente, óxidos de silício ou bayerita ( $\alpha$ -Al(OH)<sub>3</sub>) foram encontrados como produtos de corrosão; mas em amostras de PHS após SST, compostos à base de ferro foram principalmente identificados, incluindo magnetita (Fe<sub>3</sub>O<sub>4</sub>), goethita ( $\alpha$ -FeOOH), lepidocrocita ( $\gamma$ -FeOOH), acaganeita ( $\beta$ -FeOOH) e óxidos de silício. A presença de hematita ( $\alpha$ -Fe<sub>2</sub>O<sub>3</sub>) foi relacionada à intensidade do laser.

Esta tese de doutorado também incluiu um estudo de viabilidade que teve como objetivo o monitoramento *in situ* da fase cristalina presente na superfície das amostras, antes e após a estampagem a quente, em meio de cloreto por difração de raios-X síncrotron. A abordagem sugerida funcionou como princípio de análise. Além disso, os resultados trouxeram contribuições importantes sobre a presença de fases intermetálicas no revestimento de Al-Si, seja antes ou depois da estampagem a quente, e sua dinâmica de transformação na qual são altamente dependentes das condições iniciais do estado sólido/líquido no início de ambos os processos de imersão a quente e de estampagem a quente.

Finalmente, a observação mais importante desta investigação é que o processo de estampagem a quente altera a morfologia do revestimento de Al-Si e também suas propriedades de corrosão. A camada de revestimento se torna mais nobre, mas diminui muito

a força motriz da proteção catódica. Embora as subcamadas ricas em Al possam desempenhar um papel de ânodo de sacrifício, o substrato de aço é principalmente protegido por barreira de proteção pelas subcamadas enriquecidas em ferro.

Palavras-chave: estampagem a quente, alumínio-silício por imersão a quente, comportamento eletroquímico.

## LIST OF PUBLICATIONS

### **Publication under review in peer-reviewed journal**

COUTO, C.P.; REVILLA, R.I.; POLITANO, R.; COSTA, I.; PANOSSIAN, Z.; DE GRAEVE, I.; ROSSI, J.L.; TERRY, H. Influence of different austenitisation temperatures during hot-stamping process on the local electrochemical behaviour of 22MnB5 steel coated with hot-dip Al-Si. **Corrosion Science**.

### **Papers published in peer-reviewed journals**

COUTO, P. C; ANDREATTA, F.; LANZUTTI, A.; COSTA, I; PANOSSIAN, Z.; DE GRAEVE, I.; TERRY, H.; ROSSI, J.L; REVILLA, R.I. Depth profiling approach to evaluate the influence of hot stamping on the local electrochemical behaviour and galvanic series of hot-dip Al-Si coating on 22MnB5 steel. **Corrosion Science**. 2021. <https://doi.org/10.1016/j.corsci.2021.109435>.

COUTO, C.P.; REVILLA, R.I.; COLOSIO, M. A.; COSTA, I.; PANOSSIAN, Z.; DE GRAEVE, I.; TERRY, H.; ROSSI, J.L. Electrochemical behaviour of 22MnB5 steel coated with hot-dip Al-Si before and after hot-stamping process investigated by means of scanning Kelvin probe microscopy. **Corrosion Science**. 174 (2020) 108811. <https://doi.org/10.1016/j.corsci.2020.108811>.

COUTO, C. P.; COSTA, I.; VIVEIROS, B. V. G.; ALENCAR, M. C.; COLOSIO, M.A.; PANOSSIAN, Z.; ROSSI, J.L. The use of Scanning Vibrating Electrode Technique to Evaluate the Effect of Hot Stamping on the Corrosion Resistance of 22MnB5 press-hardened Steel Electroplated with Zn-Ni. **Materials Research**. 2019; 22(suppl. 1): e20190163. <https://doi.org/10.1590/1980-5373-MR-2019-0163>

### **Conference proceedings**

COUTO, C. P.; BARBOSA, L. P.; COLOSIO, M.A.; COSTA, I.; PANOSSIAN, Z.; ROSSI, J.L. Characterization of 22MnB5 steel metallic coated with either hot-dip AlSi or electroplated ZnNi before and after hot stamping. In: SAE Brazil Congress, 03 - 05 September, 2018, São Paulo - Brazil. **SAE Technical Papers**. 2018. doi:10.4271/2018-36-0074.

COUTO, C. P.; POLITANO, R.; GOMES, M. P.; COLOSIO, M.A.; ROSSI, J.L. Diffusion Analyses Using GDOES Technique of the 22MnB5 Press Hardened Steel with Al-Si and Zn-Ni Coatings. In: 22<sup>nd</sup> Brazilian Congress of Engineering and Materials Science, 06-10 November, 2016, Natal - Brazil. **Materials Science Forum**. 2018. doi:10.4028/www.scientific.net/MSF.930.472.

COUTO, C. P.; GOMES, M.P.; COSTA, P.D.O.; COLOSIO, M.A.; POLITANO, R.; ROSSI, J.L. Characterization of PHS coating layer using GDOES technique. In: VII Workshop of Applied Crystallography to Materials Science and Engineering, 05 - 07 September, 2017, Espírito - Santo, Brazil. **Blucher Proceedings**. 2017. doi:.5151/phypro-viii-efa-08.

COUTO, C. P.; COSTA, P. D. O. L.; MARTINEZ, L. G.; TURRILLAS, X.; ROSSI, J. L. The use of X-ray diffraction for phase identification of press hardened steels. In: VI Workshop of Applied Crystallography to Materials Science and Engineering, 13 - 14 May, 2016, Espírito Santo - Brazil. **Blucher Proceedings**. 2016. doi: 10.5151/phypro-vii-efa-038.

### **Extended abstract**

COUTO, C. P.; COSTA, I.; PANOSSIAN, Z.; COLOSIO, M.A.; DE CAMPOS, L. G. F.P.; ROSSI, J.L. Corrosion resistance and adhesion evaluation of press hardened steel 22MnB5 coated with AlSi and ZnNi in cyclic corrosion testing. In: INTERCORR, 14 - 18 May, 2018, São Paulo - Brazil. **ABRACO**. 2018.

### **Oral presentation at conferences**

COUTO, P. C; ANDREATTA, F.; LANZUTTI, A.; COSTA, I; PANOSSIAN, Z.; DE GRAEVE, I.; TERRY, H.; ROSSI, J.L; REVILLA, R.I. Combined GDOES & electrochemical micro-cell measurements to study the influence of hot stamping on the galvanic behaviour of hot-dip Al-Si coatings on 22MnB5 steel. **Eurocorr 2020**, 7 - 11 September, 2020. Virtual edition.

COUTO, C.P.; REVILLA, R.I.; COLOSIO, M. A.; COSTA, I.; PANOSSIAN, Z.; DE GRAEVE, I.; TERRY, H.; ROSSI, J.L. Investigation of electrochemical behaviour of 22MnB5 steel coated with hot-dip Al-Si before and after hot stamping process by means of SKPFM measurements. **Eurocorr 2019**, 9 - 13 September, 2019. Seville - Spain.

COUTO, C. P.; BARBOSA, L. P.; COLOSIO, M.A.; COSTA, I.; PANOSSIAN, Z.; ROSSI, J.L. Characterization of 22MnB5 steel metallic coated with either hot-dip AlSi or electroplated ZnNi before and after hot stamping. **SAE Brazil Congress**. 03 - 05 September, 2018. São Paulo - Brazil.

COUTO, C. P.; COSTA, I.; PANOSSIAN, Z.; COLOSIO, M.A.; DE CAMPOS, L. G. F.P.; ROSSI, J.L. Corrosion resistance and adhesion evaluation of press hardened steel 22MnB5 coated with AlSi and ZnNi in cyclic corrosion testing. **INTERCORR**, 14 - 18 May, 2018, São Paulo - Brazil.

COUTO, C. P.; POLITANO, R.; GOMES, M. P.; COLOSIO, M.A.; ROSSI, J.L. Characterization of PHS coating layer using GDOES technique. **VII Workshop of Applied Crystallography to Materials Science and Engineering**, 05 - 07 September, 2017, Espírito - Santo, Brazil

COUTO, C.P.; COLOSIO, M.A.; ROSSI, J.L. Diffusion study of the chemical elements present in AlSi and ZnNi coatings applied onto 22MnB5 steel for hot stamping. **36<sup>th</sup> SENAFOR**. 05 - 07 October, 2016. Porto Algre - Brazil.

COUTO, C. P.; COSTA, P. D. O. L.; MARTINEZ, L. G.; TURRILLAS, X.; ROSSI, J. L. The use of X-ray diffraction for phase identification of press-hardened steels. **VI Workshop of Applied Crystallography to Materials Science and Engineering**, 13 - 14 May, 2016, Espírito Santo - Brazil.

## **The effect of hot-stamping process on the local electrochemical behaviour of the 22MnB5 steel coated with hot-dip aluminium silicon**

Press-hardened steel (PHS) is a strategic steel for the automotive industry. The application of this type of steel in the vehicle structures allows safety improvement, mass reduction and less fuel consumption. Due to its ultra-high-tensile strength, the PHS components are produced by means of hot stamping. The process consists of heating the steel at temperatures higher than 800 °C and then transferring it to a press tool, for simultaneous forming and quenching. The thermo-mechanical process may cause both steel oxidation and decarburisation; for these reasons, the steel substrate is often protected with metallic coatings prior to hot stamping. Zinc and aluminium-based systems are often used as coatings for automotive applications. However, the hot-dip aluminium-silicon (Al-Si) system is the most widespread and used in hot-stamped components. This coating presents good corrosion and oxidation resistance at high temperatures. Nonetheless, during hot stamping, the initial microstructure and chemical composition of the metallic coating are greatly altered, due to diffusion. Hence, after hot stamping the whole coating layer becomes a complex multi-layered system enriched in iron. Consequently, the coating properties, including the corrosion properties, also change after hot stamping. However, little is known about the effect of the morphological and compositional changes of the Al-Si coating, due to the thermo-mechanical process, on its corrosion behaviour and performance. The different sublayers in the coating form micro-galvanic couplings, which can affect the global electrochemical behaviour of the system. Therefore, a detailed approach based on local electrochemical techniques was suggested to evaluate the role that each sublayer plays on the electrochemical behaviour. The most important contribution from this investigation highlights the substantial influence of slight variation on hot-stamping parameters which greatly alters the structure-composition of the coating layer. Consequently, this results in considerable variations of the local corrosion and electrochemical behaviour of the coating-steel system.

**INSTITUTO DE PESQUISAS ENERGÉTICAS E NUCLEARES**  
**Diretoria de Pesquisa, Desenvolvimento e Ensino**  
**Av. Prof. Lineu Prestes, 2242 – Cidade Universitária CEP: 05508-000**  
**Fone/Fax(0XX11) 3133-8908**  
**SÃO PAULO – São Paulo – Brasil**  
**<http://www.ipen.br>**

**O IPEN é uma Autarquia vinculada à Secretaria de Desenvolvimento,  
associada  
à Universidade de São Paulo e gerida técnica e administrativamente pela  
Comissão Nacional de Energia Nuclear, órgão do  
Ministério da Ciência, Tecnologia, Inovações e Comunicações.**